Publication of the Astronomy Department of the Eötvös University

Volume 12

2nd Workshop of Young Researchers in Astronomy & Astrophysics

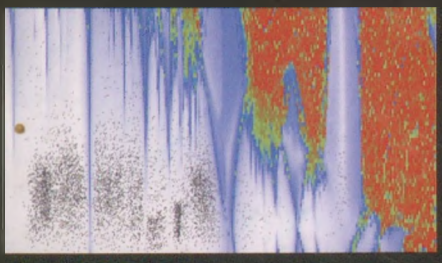

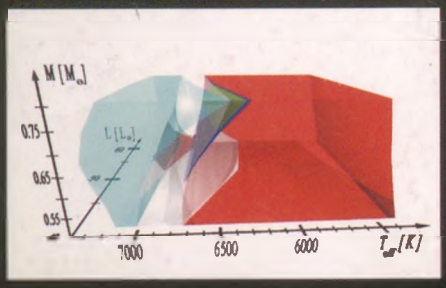

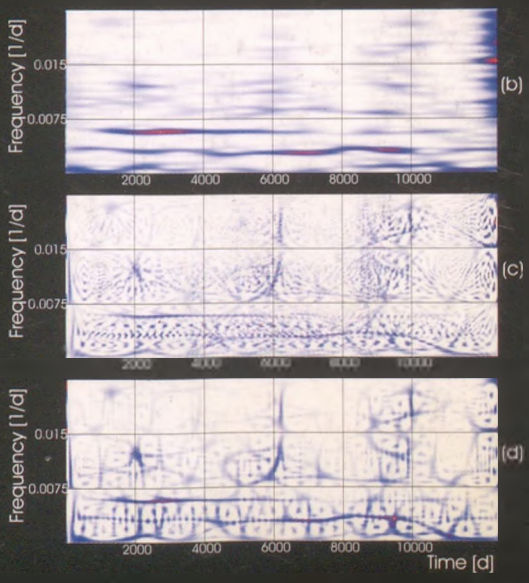

Edited by
E. Forgács-Dajka

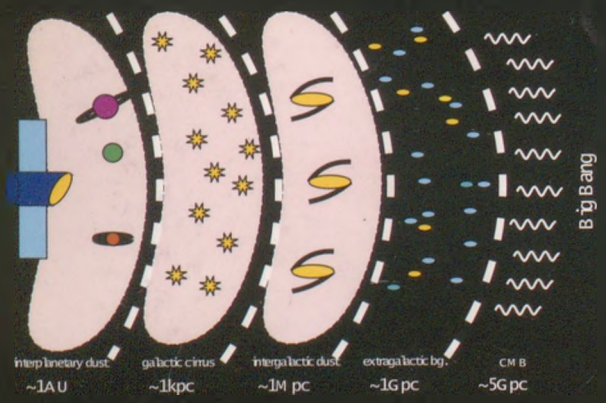

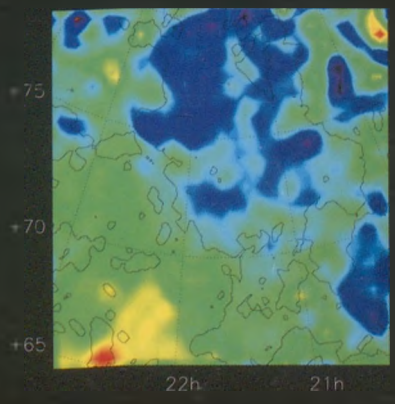

Budapest 2002

Publications of the Astronomy Department of
the Eötvös Loránd University
Vol.12.

2nd Workshop of Young Researchers in Astronomy & Astrophysics

Hungary, January 2002

EDITED BY
E. Forgács-Dajka

Published by the Department of Astronomy of the Eötvös University
Budapest 2002

ISBN 963 463 557
HU ISSN 0238-2423
Responsible publisher: Dr. Bálint Érdi

Contents

Interstellar Matter

Variable Stars

PREFACE

Two years ago, in November 2000, we organized the first meeting of postgraduate students in astronomy and astrophysics.

The success of this meeting motivated us to organize the second meeting in January 2002. According to our original intention it seems we have been able to start a tradition. Being one of the organizers and participants of these meetings, it is a great pleasure, honour, and satisfaction for me to present this proceedings.

We think that this conference was a good occasion for the young researchers in astronomy and astrophysics to present and discuss their researches and results.

The speakers gave their talks covering the following areas of astronomy:

- Application of (Magneto)hydrodinamics to Astrophysical Problems
- Celestial Mechanics
- Extragalactic Astronomy
- Interstellar Matter
- Variable Stars

We also hope that the readers of this volume will find interesting and useful ideas for their future works.

We are grateful to the Department of Astronomy of the Eötvös University, to the Hungarian Astronomical Foundation/IBVS and to the National Federation of PhD Students for their financial support.

Zsolt Sándor
Organizing Committee

List of Participants

Name	Address
Borkovits, T.	Baja Astronomical Observatory of Bács-Kiskun County H-6500, Baja, Szegedi út, P.O.Box 766., Hungary borko@electra.bajaobs.hu
Csizmadia, Sz.	Konkoly Observatory H-1525 Budapest, P.O.Box 67., Hungary csizmadia@konkoly.hu
Csubry, Z.	Konkoly Observatory H-1525 Budapest, P.O.Box 67., Hungary csubry@konkoly.hu
Forgács-Dajka, E.	Eötvös Loránd University Department of Astronomy H-1518 Budapest, P.O.Box 32., Hungary E.Forgacs-Dajka@astro.elte.hu
Frey, S.	FÖMI Satellite Geodetic Observatory, Penc H-1373 Budapest, P.O. Box 546., Hungary frey@sgo.fomi.hu
Győry, Zs.	Eötvös Loránd University Department of Physics of Complex Systems H-1117 Budapest, Pázmány P. s. 1/A, Hungary gyory@complex.elte.hu
Kiss, Cs.	Konkoly Observatory H-1525 Budapest, P.O.Box 67., Hungary pkisscs@konkoly.hu
Kiss, Z.	Eötvös Loránd University Department of Astronomy H-1518 Budapest, P.O.Box 32., Hungary Z.Kiss@astro.elte.hu

Könyves, V.	Eötvös Loránd University Department of Astronomy H-1518 Budapest, P.O.Box 32., Hungary V.Konyves@astro.elte.hu
Kővári, Zs.	Konkoly Observatory H-1525 Budapest, P.O.Box 67., Hungary kovari@konkoly.hu
Marik, D.	Eötvös Loránd University Department of Astronomy H-1518 Budapest, P.O.Box 32., Hungary D.Marik@astro.elte.hu
Moór, A.	Eötvös Loránd University Department of Astronomy H-1518 Budapest, P.O.Box 32., Hungary A.Moor@astro.elte.hu
Mosoni, L.	FÖMI Satellite Geodetic Observatory, Penc H-1373 Budapest, P.O. Box 546., Hungary mosoni@sgo.fomi.hu
Paragi, Zs.	FÖMI Satellite Geodetic Observatory, Penc H-1373 Budapest, P.O. Box 546., Hungary paragi@sgo.fomi.hu
Pál, A.	Eötvös Loránd University Department of Astronomy H-1518 Budapest, P.O.Box 32., Hungary apal@ludens.elte.hu
Pócs, M.	Konkoly Observatory H-1525 Budapest, P.O.Box 67., Hungary pocs@konkoly.hu
Ribárik, G.	Konkoly Observatory H-1525 Budapest, P.O.Box 67., Hungary ribarik@konkoly.hu
Sándor, Zs.	Eötvös Loránd University Department of Astronomy H-1518 Budapest, P.O.Box 32., Hungary Zs.Sandor@astro.elte.hu

Süli, Á. Eötvös Loránd University
Department of Astronomy
H-1518 Budapest, P.O.Box 32., Hungary
saron@astro.elte.hu

Szabó, R. Konkoly Observatory
H-1525 Budapest, P.O.Box 67., Hungary
rszabo@konkoly.hu

Széll, A. Glasgow Caledonian University
Department of Mathematics
Cowcaddens Road Glasgow, G4 0BA, Scotland
a.szell@gcal.ac.uk

Application of (Magneto)hydrodynamics to Astrophysical Problems

Z. Csubry
R. Erdélyi
E. Forgács-Dajka
D. Marik
R. Szabó

A POSSIBLE MODEL FOR THE FAST SOLAR TACHOCLINE

Emese Forgács-Dajka
Eötvös Loránd University, Department of Astronomy
H-1518 Budapest, P.O.Box 32., Hungary
E-mail: E.Forgacs-Dajka@astro.elte.hu

Abstract

One possible scenario for the origin of the solar tachocline, known as the "fast tachocline", assumes that the turbulent diffusivity exceeds $\eta \geq 10^9\,\mathrm{cm}^2/\mathrm{s}$. In this case the dynamics will be governed by the dynamo-generated oscillatory magnetic field on relatively short timescales. Here, we present detailed numerical models for the fast solar tachocline with all components of the magnetic field calculated explicitly, assuming axial symmetry and a constant turbulent diffusivity η and viscosity ν.
KEYWORDS: *Sun: interior – MHD – tachocline*

1. Introduction

The existence and properties of the tachocline have been known from helioseismic studies, recently reviewed by Corbard et al. (2001). The tachocline is known to be extremely thin (Corbard et al., 1999; Charbonneau et al., 1999; Basu & Antia, 2001).

The extreme thinness of the tachocline implies a strongly anisotropic transport of angular momentum. Several different mechanisms have been proposed for this transport, but it is now widely believed that the magnetic field is instrumental in its origin (Gilman & Dikpati, 2000; Gilman, 2000).

Depending on the value of the magnetic diffusivity, this magnetic field may either be a weak permanent, primordial field pervading the solar interior, or the strong oscillatory field generated by the solar dynamo. It follows that for $\eta \leq 10^8\,\mathrm{cm}^2/\mathrm{s}$ the dynamo field cannot penetrate the tachocline, and we can expect the tachocline to be pervaded by the internal primordial field. On the other hand, for $\eta \geq 10^9\,\mathrm{cm}^2/\mathrm{s}$ the tachocline dynamics should be governed by the dynamo field. As the associated diffusive and Lorentz timescales are also very different, these two cases basically correspond to the case of "slow" and "fast" tachocline, discussed in the literature (see esp. Table I in Gilman, 2000; Brun, 2001).

The case of a slow tachocline has been studied extensively in recent years by

a number of authors (MacGregor & Charbonneau, 1999; Rüdiger & Kitchatinov, 1997; Garaud, 2001). The alternative case of a fast tachocline, in contrast, has received much less attention. This is so despite that several authors, (e.g. Gilman, 2000) noted that the tachocline is more likely to be dynamically coupled to the convective zone than to the radiative zone, and that a part of the tachocline is *known* to overlap with the strongly turbulent convective zone, especially at higher latitudes. Faced with this situation, in a recent paper (Forgács-Dajka & Petrovay (2001), hereafter FDP01) we considered the case of a turbulent tachocline with a turbulent diffusivity of about 10^{10} cm^2/s, pervaded by an oscillatory dipole field.
In the present paper we will include a self-consistent calculation of the poloidal field.

2. Equations

The time evolution of the velocity field $\mathbf{v}$ and magnetic field $\mathbf{B}$ are governed by the Navier-Stokes and induction equations. We write these in a frame rotating with the fixed internal rotation rate Ω_0:

$$\partial_t \mathbf{v} + (\mathbf{v}\cdot\nabla)\,\mathbf{v} = \nabla\left(\frac{1}{2}|\vec{\Omega}_0\times\mathbf{r}|^2 - V\right) - 2(\vec{\Omega}_0\times\mathbf{v}) - \frac{1}{\rho}\nabla\left(p+\frac{B^2}{8\pi}\right) + \frac{1}{4\pi\rho}(\mathbf{B}\cdot\nabla)\mathbf{B} + \frac{1}{\rho}\nabla\cdot\hat{\tau}, \tag{1}$$

and

$$\partial_t \mathbf{B} = \nabla\times(\mathbf{v}\times\mathbf{B}) - \nabla\times(\eta\nabla\times\mathbf{B}), \tag{2}$$

where $\mathbf{r}$ is the radius vector, $\hat{\tau}$ is the viscous stress tensor, η is the (turbulent) magnetic diffusivity, V is the gravitational potential and p is pressure. These equations are supplemented by the constraints of mass and magnetic flux conservation.
We assume spherical geometry and axisymmetry in all our calculations. The velocity and magnetic fields can be written as

$$\mathbf{v} = \omega(r,\theta,t) r\sin\theta\,\mathbf{e}_\phi \tag{3}$$

$$\mathbf{B} = B(r,\theta,t)\mathbf{e}_\phi + \nabla\times[A(r,\theta,t)\mathbf{e}_\phi], \tag{4}$$

where $B(r,\theta,t)$ and $A(r,\theta,t)$ represent the poloidal components of the magnetic field and of the vector potential, respectively; $\omega(r,\theta,t)\equiv\Omega-\Omega_0$ is the residual

angular velocity, $\mathbf{e}_\phi$ is the azimuthal unit vector and the meridional circulation is neglected.
The evolution of the poloidal magnetic field is, in contrast, self-consistently calculated by integrating equation (2) as usual:

$$\partial_t A + \frac{1}{r\sin\theta}(\mathbf{v}_m \cdot \nabla)(r\sin\theta A) = \eta\left(\nabla^2 - \frac{1}{r\sin\theta}\right)A. \tag{5}$$

The computational domain for the present calculations consists of just the upper part of the radiative interior, between radii $r_{\rm in}$ and $r_{\rm bcz}$, where $r_{\rm bcz}$ is the radius of the bottom of the convection zone. For the integration of equations we use the following boundary conditions. At the pole and the equator axial and equatorial symmetry is required for ω, and dipole symmetry for the magnetic field:

$$\begin{aligned} \partial_\theta\omega = B = \quad A = 0 \qquad & \text{at } \theta = 0, \\ \partial_\theta\omega = B = \partial_\theta A = 0 \qquad & \text{at } \theta = \pi/2. \end{aligned} \tag{6}$$

The bottom of our box is supposed to be a rigidly rotating perfect conductor — a good approximation for the solar interior. The rigid rotation speed is fixed at the observed rate $\Omega_0/2\pi = 437$ nHz. Thus, the lower boundary conditions are:

$$\omega = B = A = 0 \qquad \text{at } r = r_{\rm in} \tag{7}$$

At the upper boundary of our domain, i.e. at the bottom of the convective zone, we use the following boundary conditions:

$$\begin{aligned} &\omega = \Omega_{\rm bcz} - \Omega_0 \\ &A = A_0 \sin\theta\cos(\omega_{\rm cyc}t) \qquad \text{at } r = r_{\rm bcz}, \\ &B = 0 \end{aligned} \tag{8}$$

The physical assumptions behind these conditions are the following. For ω we suppose that the rotation rate can be described with the same expression as in the upper part of the convection zone. In accordance with the observations of the GONG network, the expression used for $\Omega_{\rm bcz}$ is

$$\frac{\Omega_{\rm bcz}}{2\pi} = 456 - 72\cos^2\theta - 42\cos^4\theta \ \text{nHz}. \tag{9}$$

Our upper boundary condition on the poloidal field is the simplest possible representation of the poloidal component of the solar dynamo field, a dipole oscillating with a period of 22 years. The factor A_0 fixes the poloidal field

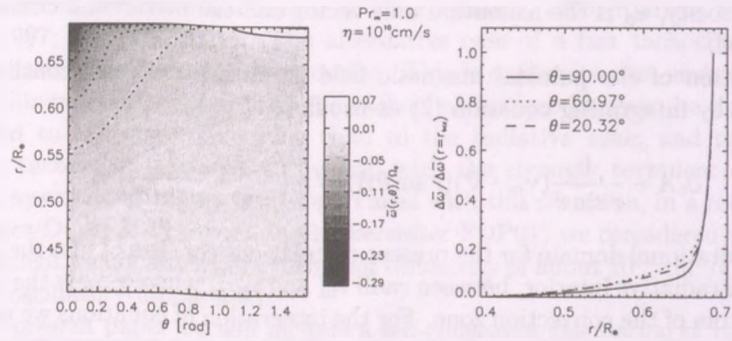

Figure 1: Spreading of the differential rotation into the radiative interior for $\eta = \nu = 10^{10}\mathrm{cm}^2/\mathrm{s}$. *Left-hand panel:* contours of the time-average of the angular rotation rate $\omega(r, \theta, t)$ under one dynamo period. Equidistant contour levels are shown, separated by intervals of $100\,\mathrm{nHz}/\Omega_0$, starting from 0 towards both non-negative (solid) and negative (dashed) values. *Right-hand panel:* normalized differential rotation amplitude $\Delta\overline{\omega}$ at different latitudes as a function of radius. The peak amplitude of the poloidal magnetic field is $B_p \sim 2570$ G.

amplitude. Finally, the upper boundary condition chosen for the toroidal field assumes that the toroidal field is negligible in the convective zone compared to its value in the tachocline. Such a hypothetical situation is in line with current thinking in dynamo theory, and it may be a natural consequence of buoyancy-driven instabilities effectively removing any toroidal flux from the convective zone.

The initial conditions chosen for all calculations are

$$\begin{aligned} &\omega(r,\theta,t=0) = \Omega_{\mathrm{bcz}} - \Omega_0 \quad \text{at } r = r_{\mathrm{bcz}} \\ &\omega(r,\theta,t=0) = 0 \qquad\qquad\quad \text{at } r < r_{\mathrm{bcz}} \\ &B(r,\theta,t=0) \equiv 0 \\ &A(r,\theta,t=0) = A_0 \sin\theta \quad \text{at } r = r_{\mathrm{bcz}} \\ &A(r,\theta,t=0) = 0 \qquad\qquad\quad \text{at } r < r_{\mathrm{bcz}} \end{aligned} \tag{10}$$

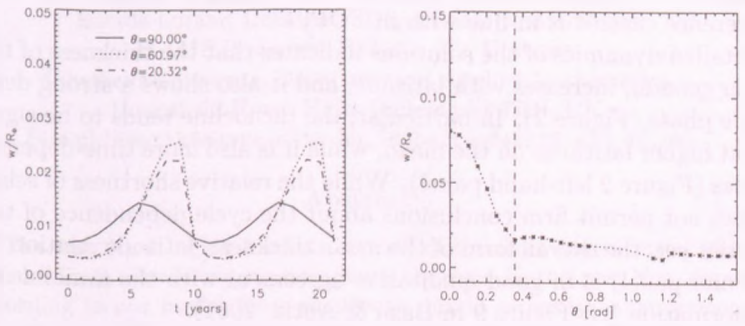

Figure 2: *Left-hand panel:* The thickness of the tachocline at different latitudes as a function of time for the case in Figure 1. *Right-hand panel:* Latitudinal variation of the mean tachocline thickness for the case in Figure 1. A vertical dashed line indicates the poleward limit of reliable helioseismic data.

3. Results and discussion

We present results for a case with $\mathrm{Pr_m} = 1$, $\eta = \nu = 10^{10}\mathrm{cm}^2/\mathrm{s}$, and no meridional circulation. This case corresponds to that computed in FDP01, except that the poloidal field is now not prescribed throughout the volume, but explicitly calculated. The results are shown in Figure 1. In the left-hand panel we plotted the contours of the time-average of the angular rotation rate, which is defined as $\overline{\omega}(r,\theta) = \frac{1}{P_{\mathrm{cyc}}} \int_t^{t+P_{\mathrm{cyc}}} \omega(r,\theta,t)\,\mathrm{d}t$. In the right-hand panel the differential rotation amplitude $\Delta\omega$ is defined as $\Delta\omega = \omega(r,\theta,t) - \int_0^{\pi/2} \omega(r,\theta,t)\sin\theta\,\mathrm{d}\theta$ and $\Delta\overline{\omega} = \overline{\omega}(r,\theta) - \int_0^{\pi/2} \overline{\omega}(r,\theta)\sin\theta\,\mathrm{d}\theta$. The thickness of the tachocline will be defined throughout this paper as the scale height of $\Delta\omega$ (i.e. the depth from the top of our domain where $\Delta\omega$ is reduced by $1/\mathrm{e}$). By "mean thickness", in turn, we will refer to the scale height of $\Delta\overline{\omega}$.

The results shown in Figure 1 are in accordance with those in FDP01. In particular, we confirm that an oscillatory poloidal field with dipolar latitude dependence at the tachocline–convective zone boundary is able to confine the thickness of tachocline.

In order to find the right value of *confining field strength* B_{conf} we experimented with many different field strengths, however, in this paper we only present results computed with $B = B_{\mathrm{conf}}$ (cf. FDP01 for calculations with other field

strengths). The value of the confining field strength is found to be 2570 G for the reference case, it is in line with in FDP01.
The detailed dynamics of the solutions indicates that the thickness of the tachocline, in general, increases with latitude, and it also shows a strong dependence on cycle phase (Figure 2). In particular, the tachocline tends to be significantly wider at higher latitudes on the mean, while it is also more time-dependent near the poles (Figure 2 left-hand panel). While the relative shortness of seismic data sets does not permit firm conclusions about the cycle dependence of tachocline properties yet, the overall form of the mean thickness–latitude relation (Figure 2 right-hand panel) is in good qualitative agreement with the available helioseismic information (cf. Figure 9 in Basu & Antia, 2001).
Computer animations illustrating the time development of some of our solutions can be downloaded from the following web site: `http://astro.elte.hu/kutat/sol/fast1/fast1e.html`

Acknowledgements

I thank Sarbani Basu for useful insights on how to interpret helioseismic constraints on the tachocline. This work was funded by the OTKA under grants no. T032462.

References

Basu, S., & Antia, H. M. 2001, MNRAS , 324, 498

Brun, A. S. 2001, in Helio- and Asteroseismology at the Dawn of the Millennium (ESA Publ. SP-464), 273

Charbonneau, P., Christensen-Dalsgaard, J., Henning, R., et al. 1999, ApJ, 527, 445

Charbonneau, P., & MacGregor, K. B. 1997, ApJ, 486, 502

Corbard, T., Blanc-Féraud, L., Berthomieu, G., & Provost, J. 1999, A&A, 344, 696

Corbard, T., Jiménez-Reyes, S. J., Tomczyk, S., Dikpati, M., & Gilman, P. 2001, in Helio- and Asteroseismology at the Dawn of the Millennium (ESA Publ. SP-464), 265

Forgács-Dajka, E., & Petrovay, K. 2001, Solar Phys. , 203, 195 (FDP01)

Garaud, P. 2001, MNRAS , 329, 1

Gilman, P. A. 2000, Solar Phys. , 192, 27

Gilman, P. A., & Dikpati, M. 2000, ApJ, 528, 552

MacGregor, K. B., & Charbonneau, P. 1999, ApJ, 519, 911

Rüdiger, G., & Kitchatinov, L. L. 1997, Astr. Nachr., 318, 273

Numerical Simulations of Blinker Events

Dániel Marik[1,2] and Róbert Erdélyi[2]
[1]Eötvös Loránd University, Department of Astronomy
H-1518 Budapest, P.O.Box 32., Hungary
[2]Sheffield University, Department of Applied Mathematics
Hounsfield Road, Hicks Building S3 7RH, UK
E-mail:[1]dmarik@astro.elte.hu,[2]Robertus@sheffield.ac.uk

Abstract

The transition region blinkers are one of the most controversial phenomena in the lower solar atmosphere observed in the past five years. According to our model these small-scale bright intensity enhancements may play a significant role not only in the solar transition region but even in the solar wind acceleration and the solar atmospheric plasma heating. They were mainly found, e.g., in He I (584.33 Å), O III (599.52 Å), O IV (554.52 Å), O V (629.73 Å) and Mg IX (368.06 Å), respectively (Harrison, 1997). Their typical parameters are: the mean lifetime is approximately $16s$, the intensity enhancement ratios are around 1.8, and the appearing frequency on the whole solar surface is at $1-20s^{-1}$. Blinker events appear to be increases in density or filling factor rather then to be increases in temperature. Most of the blinkers have repetitive nature and high percentage of these events occur above regions where one magnetic polarity dominates.

We have developed a simple physical model of blinkers based on the process of **magnetic reconnection** (Priest, 1982). In the present paper we show our results of solving the fully nonlinear, time-dependent, dissipative, radiative 2-D MHD equations using a staggered mesh. By setting the initial parameters describing blinkers we found propagating jets with similar properties found by observations.

Keywords: *Sun: transition region – blinker – magnetic reconnection*

1. Introduction

There are numerous observaions about blinkers produced by the Coronal Diagnostic Spectrometer (CDS) of the Solar and Heliospheric Observatory (SOHO). The most frequently investigated lines are He I, formed at $2 \cdot 10^4 K$ (chromospheric line), O III, O IV, and O V formed in the transition region at $10^5 K$, $1.6 \cdot 10^5 K$ and $2.5 \cdot 10^5 K$, respectively and Mg IX, Mg X formed at $10^6 K$ and $1.2 \cdot 10^6 K$.

Blinkers are best detected in the O V line and are found to occur in both the active and quiet region of the Sun. The typical behaviour of the active-region blinkers are very similar to the quiet-region blinkers (Parnell et al., 2001). In order to understand the problem of blinker events we recall some data obtained by (Bewsher et al., 2001) considering only the quiet region blinkers.

The mean lifetime of a blinker event is approximately 16 minutes, the mean rise and fall times are at around 8 minutes and the intensity enhancement ratios are around 1.8. The frequency of blinker events on the whole Solar surface is at around $1 - 20\ s^{-1}$. Futhermore there are evidences that blinker events appear to be increases in density or filling factor rather than to be increases in temperature. Most of the blinkers have a repetitive nature but according to a Fourier and wavelet analysis no evidence of any periodic behaviour in blinkers can be found.

The statistical analysis of blinkers also shows that the distribution of blinkers is not uniform, they are located in regions of strongest emission in the chromospheric and transition region lines. In addition almost the total number of blinkers occur above well defined strong magnetic fragments and approximetely 75% of this events can be found above regions where only one polarity dominates.

Our basic idea to model blinker events is the phenomena of magnetic reconnection. In the present study our aim is to investigate the reconnection jects caused by the process of magnetic reconnection in a 2D physical environment representing the solar transition region. Magnetic flux cancellation is initiated by a localized increase of the magnetic diffusivity in the current concentration.

2. Basic Equations and Initial State

In the present case we are considering the atmospheric solar plasma as an ideal gas in the presence of magnetic field. For simplicity, the effect of gravity is neglected. The governing equations of a 2D dissipative, radiative MHD are can be seen in, e. g., (Roussev et al., 2001a).

We consider the initial magnetic field configuration as follows

$$\mathbf{B} = (0, B_y); \quad B_y = B_0 \tanh\left(C\frac{x}{L_0}\right),$$

where L_0 and B_0 are the typical values of a length scale and magnetic field strength, respectively, and C is a constant. (In our calculation the y axis is perpendicular to the solar surface.) Futhermore the initial equilibrium velocity

is assumed to be zero throughout the computational domain. The total pressure balance can be considered as

$$\frac{B^2}{2} + P = \frac{B_0^2}{2} + P_0 = \text{const.}$$

where P is the kinetic gas pressure. We initially assume a uniform kinetic gas pressure distribution in the y-direction and, as a result, the thermal energy $e = P/(\gamma - 1)$ is also uniform in the y -direction. To represent the transient region we use the following expression for the density stratification in the y -direction:

$$\varrho(y) = \varrho_0 \left\{ 1 + \Delta\varrho \left\{ 1 - \tanh \left[\frac{\varepsilon}{L_0}(y + y_s) \right] \right\} \right\},$$

where ϱ_0 represents a typical value of the mass density in the low density region; $2\Delta\varrho$ means the jump in density across the transition region; ε is a steepness parameter; and y_s is a shifting parameter. In the x direction we use the following form of the mass density distribution:

$$\varrho(x) = \varrho_0 \left(\frac{P}{P_0} \right)^{\theta} = \varrho \left(\frac{e}{e_0} \right)^{\theta},$$

where θ is a free paremter (one over the polytropic index). Finally, we also assume an energy balance in the entire physical domain for the initial state: $S(x, y) - \nabla \mathbf{q}(x, y) - L_r(x, y) = 0$ at $t = 0$, where S, $\mathbf{q}$ and L_r are the volumetric heating rate, the heat flux and the radiative loss, respectively.

In order to characterize the diffusion of the magnetic field we can initiate a localized magnetic diffusion as follows

$$\eta_{loc} = \eta_0 F(t) \exp \left\{ -\frac{\alpha}{L_0^2}[x^2 + (y + y_0)^2] \right\},$$

where F(t) is a function of time, α is a steepness parameter, y_0 is a shifting coefficient and η_0 is defined as $\eta_0 = V_{A0} L_0 / R_m$ (R_m is the magnetic Reynolds number, V_{A0} is the Alfvén speed given by $V_{A0} = B_0/\sqrt{\varrho_0}$).

This model represents the physical situation when two magnetic flux tubes of opposite polarity are pushed together and are in contact due to their foot-point motions.

3. Numerical Method

We have used a 2D compressible MHD code based on staggered meshes (Nordlund et al., 1995). The MHD equations are solved in a 2D domain using non-

uniform staggered grids. The grids are stretched in the x-direction to better resolve the region around the current concentration. In the y-direction, however, there is no stretching applied since we need high resolution all the way through in that direction. The MHD code conserves mass, momentum, energy and magnetic field divergence.

4. Simulation and Results

When the localised magnetic diffusion parameter is switched on the magnetic field on either side of the current concentration starts reconnecting. This process changes the topology of the magnetic field and the magnetic flux is advecting into the so-called X-point along the x-axis, and is beeing expelled from the diffusion region through two reconnection jets along the y-axis of the domain. We can see in Fig. 1. there is a blue shifted jet propagating towards the high temperature region reaching a higher velocity and there is a red shifted jet moving towards the high density region.

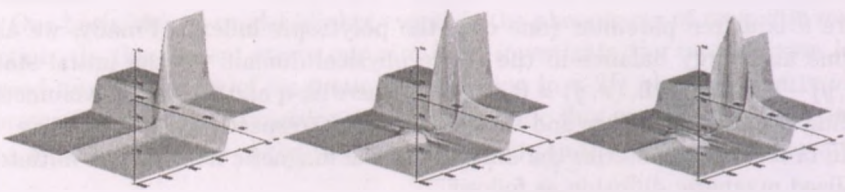

Figure 1: Time evolution of the density distribution representing the evolution of the two jets. The real times of the images are $0s$, $240s$, $275s$ from left to right, respectively. Domain size: $[4.5L_0,4.5L_0]$ in the y-direction and $[1.5L_0,1.5L_0]$ in the x-direction, where $L_0 = 3000$ km.

The same code was applied to simulate explosive events (Roussev el al., 2001c). Explosive events have different properties from blinker events. For example they are smaller and their lifetime is much shorter. The characteristics of maximum jet velocity profile is rather different, because explosive events have maximum jet velocity around the Alfvén speed. We do not have reliable data about blinker jet speeds. According to previous spactral studies it is predictable to be around 20 km/s (?) (Harrison et al., 1999).

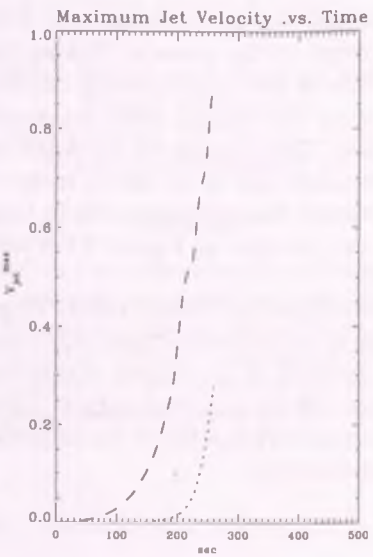

Figure 2: The 'crude' (long dashed) and the integrated (dotted) velocity profiles obtained from the same simulation as we can see in Fig. 1. $V_{jet}^{\max}$ is in Alfvén speed units ($V_{A0} = 1.293 \cdot 10^7$ cm s^{-1}).

In order to obtain solutions similar to blinker events we need to find the appropriate initial parameters. The most important parameters are η_0, t_{ri}, t_{end}, $\Delta\varrho$, y_s, and y_0. We also have to take into account several requirements, for example: the evolving jets must show density enhancement effect rather than temperature enhancement. The maximum velocity of the jets must be less than 20 km/s. We also have to consider the duration and the rising time of the blinkers.

4.1. Velocity profile

In the recent work we are focusing on the velocity profile of the outwards propagating jets. Although there is no accurate data about the maximum jet velocities it is predicted to be around 20 km/s. Before we determine the maximum velocity caracteristics for the jets we have to consider the following problems: (i) a CDS pixel overlaps a $1.7'' \times 4''$ domain which actually corresponds to a whole blinker area on the surface of the Sun. Hence, we observe an averaged image

from the whole blinker surface; (ii) the exposure time is 10 sec.; (iii) images are averaged over the whole depth of the domain. Taking into account these facts we have to take mean values of the velocity along the x-axis at every points of the y-axis. In our calculation the domain along the x-axis was $[0.21L_0,0.21L_0]$ symmetric about the y-axis. This domain on the solar surface corresponds approximately to $1.7''$. The next step is to take a mean value along the y-axis and finally we have to integrate the velocity profile in time for every 10 minutes interval. The difference can be seen in Figure 2 between the 'crude' and the integrated velocity profile.

Unfortunately we cannot simulate blinker effects longer than 8 minutes this time, because a simulation of an 8 minutes event takes approximately two days. Another problem is that 80-90 % of the blinker events belong to unipolar magnetic field dominated areas. Hence this may suggest blinkers are not results of magnetic reconnection unless there is a tilt in the unipolar magnetic field. This latter requires observational proof.

References

Roussev, I., Doyle, J. G., Galsgaard K., Erdélyi R. 2001, A&A, 380, 719
Roussev, I., Galsgaard, K., Erdélyi R., Doyle, J. G. 2001, A&A, 375, 228
Roussev, I., Galsgaard, K., Erdélyi, R., Doyle, J. G. 2001, A&A, 370, 298
Harrison, R. A. et al. 1997, Solar Phys., 175, 467
Harrison, R. A., Lang, J., Brooks, D. H., Innes D. E. 1999, A&A, 351, 1115
Bewsher D., Parnell, C. E., Harrison, R. A, 2002, Sol. Phys. (in press)
Parnell, C. E., Bewsher D., Harrison, R. A. 2002, Sol. Phys. (in press)
Nordlund, Å, Galsgaard, K. 1995, (private communication, www-solar.mcs.st-adn.ac.uk/ klaus/), A 3D MHD code for Paralell Computers
Priest E. R., 1982 Solar Magnetohydrodynamics, Univ. of St Andrews

RR Lyrae variables: pulsation and evolution

Róbert Szabó and Zoltán Csubry
Konkoly Observatory
H-1525 Budapest, P.O.Box 67., Hungary
E-mail: rszabo@konkoly.hu

Abstract

Selected results based on the application of amplitude equation formalism are presented. By means of this simple and very general description of dynamic systems, RR Lyrae pulsation and evolution can be treated collectively, despite the rather different timescales involved. The formalism and the majority of the results are applicable to Cepheids, too.
KEYWORDS: *RR Lyrae, convection, pulsation, hydrodynamics, stellar evolution*

1. Introduction

Evolution and pulsation set two different timescales in most of the pulsating variable stars across the Hertzsprung-Russel Diagram. In the case of RR Lyrae stars the typical period is 0.5 day, hence the dynamical timescale is roughly 10^{-3} yrs. Stellar evolution across the horizontal branch takes approximately 100 million years, so the difference between the evolutionary timescale and the dynamical one is at least 10 orders of magnitude. This renders collective modeling of pulsation and evolution almost impossible.

Fifth-order amplitude equations provide key ingredient to reduce the amount of costly and time-consuming hydrodynamical calculations. The formalism is also capable to describe phenomena that occurs on intermediate timescales (e.g. mode-switching, see Section 4.2).

2. Hydrodynamics

We use a 1-D hydrocode including turbulent convection, tailored to follow radial stellar pulsations. Equations and the method of treating turbulent convection can be found in Kolláth et al. (2002), Kolláth & Buchler (2000) and Buchler & Kolláth (2000). It should be noted that eight dimensionless parameters not defined by the theory are present in the equations, and the calibration does

not seem to be a straightforward task. We have circumvented the problem by setting the parameters to reproduce reasonable amplitudes and periods (Kolláth et al., 2002).

3. Amplitude equations

Amplitude equations may be applied to any dynamical system in which relative growth-rates of the excited modes are small and the pulsations are sufficiently weakly nonlinear so that an expansion in the amplitudes is justified. These conditions are valid for both Cepheid and RR Lyrae stars.

During the following discussion we are considering only fundamental (F) and first overtone (o1) modes. The appropriate amplitude equations for the nonresonant case are (Kolláth et al., 2002):

$$\dot{a}_0 = a_0(\sigma_0 + Q_{00}|a_0|^2 + Q_{01}|a_1|^2 + S_0|a_0|^2|a_1|^2 + R_{00}|a_0|^4 + R_{01}|a_1|^4) \quad (1)$$

$$\dot{a}_1 = a_1(\sigma_1 + Q_{10}|a_0|^2 + Q_{11}|a_1|^2 + S_1|a_0|^2|a_1|^2 + R_{10}|a_0|^4 + R_{11}|a_1|^4) \quad (2)$$

where a_j are complex amplitudes of the two modes, σ_j denote the linear eigenvalues for an assumed $e^{\sigma t}$ dependence, κ is the growth-rate, η is the relative growth-rate, P is the period, Q_{jk}, S_j and R_{jk} are the complex nonlinear coupling constants.

$$\sigma_j = \kappa_j + i\omega_j; \qquad P_j = \frac{2\pi}{\omega_j}; \qquad \eta_j = 2\kappa_j P_j \quad (3)$$

$$Q_{jk} = q_{jk} + i\tilde{q}_{jk}; \qquad S_j = s_j + i\tilde{s}_j; \qquad R_{jk} = r_{jk} + i\tilde{r}_{jk} \quad (4)$$

With the notations of Eqs. (4) and assuming $a_j(t) = A_j(t)e^{i\phi_j(t)}$ one can separate equations for real amplitudes (A_j) and phases (ϕ_j). One also notes that all these equations can be expressed in terms of A_0^2 and A_1^2. The constant amplitude solutions of Eq. (1, 2), the so-called fixed points are therefore obtained from solving the equations

$$\kappa_0 + q_{00}A_0^2 + q_{01}A_1^2 + s_0A_0^2A_1^2 + r_{00}A_0^4 + r_{01}A_1^4 = 0 \quad (5)$$

$$A_1 = 0 \quad (6)$$

$$\kappa_1 + q_{10}A_0^2 + q_{11}A_1^2 + s_1A_0^2A_1^2 + r_{10}A_0^4 + r_{11}A_1^4 = 0 \quad (7)$$

$$A_0 = 0 \quad (8)$$

pairwise between Eq. (5,6) and Eq. (7,8).

4. Pulsation and evolution

Fifth order amplitude equations (Eq. 1,2) are fitted to the instantaneous amplitudes and phases coming from the hydrodynamical results. Although amplitude equation coefficients are related to stellar parameters, it is impractical to derive them directly and therefore we rely on the fitting procedure, that provides them precisely and in a smooth way.

This way, hydrodynamical calculations and the amplitude equations reveal a great variety of modal selection possibilities. These include

- unstable pulsation : 1 stable (zero) fixed point, $A_0 = A_1 = 0$
- single-mode pulsation (F or o1) : 1 stable fixed point, A_0 or $A_1 \neq 0$
- double-mode pulsation : 1 stable fixed point, $A_0 \cdot A_1 \neq 0$
- and even hysteresis (either F or o1; either double-mode or F) : 2 stable fixed points) in which case the actual pulsational mode depends on the direction of evolution.

4.1. Time independent amplitude equations

Using time independent amplitude equations, evolution throughout the HRD can be followed consistently concerning the pulsational states of the star. To do so, several model sequences were computed, in which L and M are held fixed and T_{eff} is varied, thus mimicking approximately the horizontal branch evolution. The modal selection behavior was investigated by the fitted amplitude equations, and an example can be seen in Fig. 2.2..

The following tendencies were found at both $Z = 10^{-3}$ and $Z = 10^{-4}$:

- The location and the shape of the double-mode region (DMR) is independent of metallicity (Szabó et al., 2000). Its width is greater at low luminosities and high masses, while gradually vanishes towards high luminosity and/or low mass.
- Fairly wide either-or region (EOR) is present at every point of the (mass-luminosity-metallicity) parameter space.
- At high luminosity and low masses, there is an additional fundamental mode region next to the EOR, at high temperature. It seems to be a common feature at all metallicities. Its existence means, that the fixed

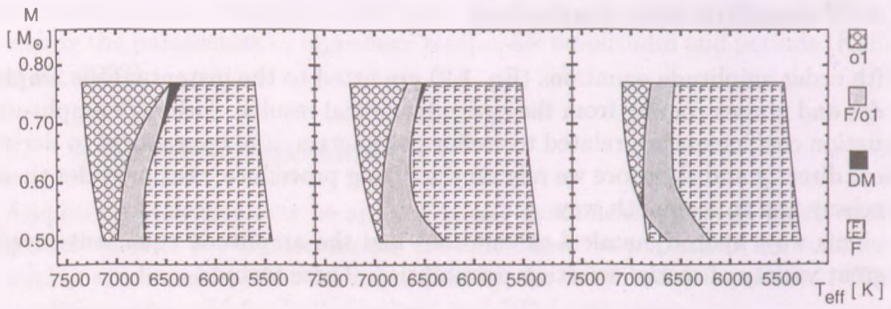

Figure 1: Modal selection of RR Lyrae sequences on the effective temperature - stellar mass plane. Luminosity increases from left to the right $L = 40, 50, 60 L_{\odot}$, $Z = 10^{-4}$. o1: *first overtone*, F/o1: *either overtone or fundamental mode*, DM: pure *double-mode*, or *either double-mode-or-fundamental-mode*, F: *fundamental mode*. We call attention to the extra F region at high luminosity and low mass. All blue and red edges were computed nonlinearly, except for F red edge, which is linear.

point of the fundamental mode loses it's stability later, than that of the overtone during blueward evolution.

It should be noted that different set of dimensionless parameters can slightly shift or distort the apparent regions.

As an application, we mention recent developments on the modeling of RR Lyrae fundamental blue edge (Szabó, 2002). Latest results of modal selection computations for a broad range of metallicities and recent horizontal branch evolutionary calculations (Demarque et al., 2000) in hand, we showed that the slope of the theoretical blue edge can be much less steeper than previously thought (Fig. 3.1.), and thus more consistent with observational constraints (compare with Kolláth et al. (2000)). This result emphasizes the importance of taking both modal selection hysteresis and evolutionary effects into account in the modeling of classical instability strips.

4.2. Time dependent amplitude equations

Application of time-dependent amplitude equations, allowed the consistent description of the mode-switching phenomena for the first time (Buchler & Kolláth,

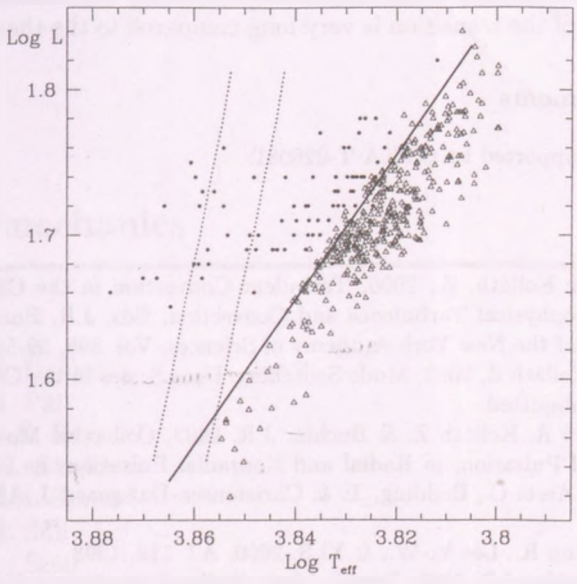

Figure 2: Theoretical fundamental blue edges. Triangles show observed RRab, dots show RRc stars. Dotted lines show the range occupied by previous theoretical blue edges, while thick line delineates blue edge computed by taking account of modal selection as well as stellar evolution.

2002): At a soft switch (entry to the instability strip at the blue or red edge, switch from F to o1 pulsation) the nascent mode starts off with infinitesimal amplitude and growth-rate. Stellar evolution causes a delay during which pulsation amplitude stays negligibly small, but after which it very rapidly achieves its quasi-static value. The delay for RR Lyrae stars is of the order of 1000 years, accounting for the observed absence of low amplitude pulsators at the vicinity of the instability strips. The switching timescale is governed by the evolutionary rate of change of the growth rate. Direct hydrodynamical calculations, designed to mimic stellar evolution by changing the core characteristics (luminosity, i.e. energy-production), showed remarkable agreement with analytic considerations (Csubry et al., 2002).

At hard bifurcations (e.g. from double-mode to F during redward evolution) the stable fixed point disappears, and the star evolves towards another fixed

point. The rate of change of the amplitude is generally not infinitesimally small. The time-scale of the transition is very long compared to the thermal timescale.

Acknowledgements

This work was supported by OTKA T-026031.

References

Buchler, J. R. & Kolláth, Z., 2000, Turbulent Convection in the Classical Variable Stars, in Astrophysical Turbulence and Convection, Eds. J.R. Buchler & H. Kandrup, Annals of the New York Academy of Sciences, Vol. 898, 39-58.

Buchler J.R & Kolláth Z, 2002, Mode Switching Time-Scales in the Classical Variable Stars, ApJ, submitted

Csubry Z., Szabó R, Kolláth Z. & Buchler J.R. 2002, Collective Modeling of Stellar Evolution and Pulsation, in Radial and Nonradial Pulsations as Probes of Stellar Physics, Eds. Aerts C., Bedding, T. & Christensen-Dalsgaard J. ASP Conf. Series, in press

Demarque P., Zinn R., Lee Y.-W., & Yi S. 2000, AJ, 119, 1398

Kolláth Z. & Buchler J.R. 2000, Double Mode Stellar Pulsations in Nonlinear Studies of Stellar Pulsations, Eds. M. Takeuti & D.D. Sasselov, Astrophysics and Space Science Library Series, Kluwer 257, 29

Kolláth Z., Buchler J.R. & Feuchtinger M. 2000, ApJ 540, 468

Kolláth Z., Buchler J.R., Szabó R. & Csubry Z. 2002, Nonlinear Beat Cepheid and RR Lyrae Models, A&A, 385, 932

Szabó R., Csubry Z., Kolláth Z. & Buchler J.R. 2000, Nonlinear Survey of RRd Models, in The Impact of Large-Scale Surveys on Pulsating Star Research, Eds. L. Szabados & D. Kurtz, ASP Conference Series, 203, 374-375.

Szabó R. 2002, A&A, in prep.

Celestial mechanics

R. Dvorak
A. Pál
A.E. Roy
Zs. Sándor
B.A. Steves
Á. Süli
A. Széll

On the Stability of Habitable Zones in Exoplanetary Systems

András Pál[1] and Zsolt Sándor[2]
Eötvös Loránd University, Department of Astronomy
H-1518 Budapest, P.O.Box 32., Hungary
E-mail:[1]apal@ludens.elte.hu,[2]szsolt@astro.elte.hu

Abstract

The dynamical stability of five exoplanetary systems is investigated by the method of the relative Lyapunov indicators. Studying the stability of the *habitable zones*, it has been found that in some systems there are regular regions, which might guarantee the long-term stability of fictive terrestrial planets.
Keywords: *Exoplanetary Systems, Habitable Zone, Chaos, Relative Lyapunov Indicators*

1. Introduction

The continuing discovery of new exoplanetary systems is a very rapidly growing and exciting field of astronomy. Since the main detection method is based on the Doppler-shift of the spectral lines of the central star, the so far discovered exoplanets are massive objects (their masses fall into the magnitude of Jupiter's mass), and they revolve relatively near to the central star. With the present accuracy of the observing techniques the detection of Earth-sized planets seems to be far away. On the other hand, the existence and dynamical stability of such objects in the *habitable zones* of exoplanetary systems has a great importance with respect to the problem of extraterrestrial life.

The habitable zone of an exoplanetary system is defined (Kasting et al., 1993) as the region, where water can exist in fluid phase on the surface of a planet. For stars close to the Sun's spectral type and mass, the habitable zone is approximately between 0.7 AU and 1.5 AU. For stars with smaller mass and later spectral type than the Sun, the boundaries of the habitable zone are shifted inward.

In this paper we investigate the dynamical stability of the habitable zones of a few representatives of the known exoplanetary systems. A commonly accepted way to perform stability investigations of a dynamical system is to separate the regular and chaotic regions of the phase space, which can be done by using chaos

detection techniques. In our study we have used a recently developed fast chaos detection method (Sándor et al., 2000).

It is well known that in our planetary system the dynamics of small bodies is governed by different resonances. The basic features of the motion of a small body are determined by the different mean-motion resonances between the small body and another massive object. The resonances can be classified as internal and external resonances, depending on the position of the investigated small object.

The discovered exoplanetary systems can also be divided in two classes depending on the position of the giant planet and the habitable zone. If the semimajor axis of the giant planet is small ($a < 0.5$ AU), the dynamics of the habitable zone is determined by external resonances (e.g. 70 Vir). If its semimajor axis is larger ($a > 1.5$ AU), the stability of the habitable zone is governed by internal resonances (e.g. ε Eri). If the giant planet is in the habitable zone, the existence of a terrestrial like object is very unlikely in this region (except maybe the presence of habitable satellites of the giant planet).

2. The applied method

In our approach we neglected the masses of the terrestrial bodies. Thus depending on the number of the giant planets in the system, we used the models of the planar restricted three or four-body problem. The system of the equations of motion can be written in vectorial form:

$$\dot{\mathbf{x}} = \mathbf{g}(\mathbf{x}), \tag{1}$$

where the vector-valued function $\mathbf{x}(t) : \mathbb{R} \to \mathbb{R}^n$ describes the evolution of the system and the dot represents the differentiation with respect to the time t. In order to study the long-term behaviour of the system (1) one can use numerical integration for a very long timespan, or calculate quantities related to the stability. A traditional tool of characterizing the chaotic behaviour is the calculation of the maximum Lyapunov characteristic exponent (LCE). The LCE can be determined by integrating the original equations of motion together with their linearized equations:

$$\begin{pmatrix} \mathbf{x}_{n+1} \\ \xi_{n+1} \end{pmatrix} = \mathcal{I}\left[\begin{pmatrix} \mathbf{g} \\ \mathcal{D}\mathbf{g} \end{pmatrix}, \Delta t\right] \begin{pmatrix} \mathbf{x}_n \\ \xi_n \end{pmatrix}, \tag{2}$$

where $\mathcal{I}[\cdot, \Delta t]$ represents symbolically a numerical integrator with stepsize Δt, and $\mathcal{D}\mathbf{g} \in \mathbb{R}^{n \times n}$ is the Jacobian matrix of (1) evaluated at $\mathbf{x}_n$. Renormalizing

the vector $\xi_i \in \mathbb{R}^n$ after each step of the numerical integration, the quantity $s_i = (1/\Delta t)\ln(|\xi_{n+1}|/|\xi_n|)$ gives the local stretching rate of the flow, and it is called *stretching number* (Voglis and Contopoulos, 1994). Then the LCE belonging to an orbit emanating from $\mathbf{x}_0$ can be calculated as the limit:

$$L^1(\mathbf{x}_0) = \lim_{n\to\infty} \frac{1}{n} \sum_{i=1}^{n} s_i. \tag{3}$$

If $L^1(\mathbf{x}_0) = 0$, the orbit emanating from $\mathbf{x}_0$ is regular (stable), if $L^1(\mathbf{x}_0) > 0$ it is chaotic, therefore unstable. A serious disadvantage of the calculation of the LCE is that it can be obtained as a limit, thus its value can only be extrapolated, which makes the identification of weakly chaotic orbits very uncertain. In recent years investigations have been focused on the development of fast chaos detection methods. One of the recently developed fast chaos detection techniques is the method of the relative Lyapunov indicators (Sándor et al., 2000). The relative Lyapunov indicator (RLI) is the absolut value of the difference between two finite time Lyapunov indicators related to two very nearby points $\mathbf{x}_0$ and $\mathbf{x}_0 + \Delta\mathbf{x}_0$:

$$\Delta L(n, \mathbf{x}_0) = |L(n, \mathbf{x}_0 + \Delta\mathbf{x}) - L(n, \mathbf{x}_0)|, \tag{4}$$

where $L(n, \mathbf{x}_0) = (1/n) \sum_{i=1}^{n} s_i$ is the finite-n approximation of the LCE, called *finite-time* Lyapunov indicator. The behaviour of $\Delta L(n, \mathbf{x}_0)$ as a function of $\mathbf{x}_0$ and n characterizes very efficiently the regular or chaotic nature of an orbit originating from $\mathbf{x}_0$. In Figure 1 the behaviour of $\Delta L(n, \mathbf{x}_0)$ can be seen for a regular and a chaotic asteroidal orbit in the Sun-Jupiter-Saturn-asteroid system. The curve oscillating around a constant value (falling into the magnitude of $|\Delta\mathbf{x}_0|$) represents regular behaviour, while the curve increasing rapidly indicates chaotic behaviour. Since the numerical integrations were carried out only for 1000 years, this method makes it possible to study a large number of initial conditions, thus to map the phase space of various dynamical systems. As a test of the method we investigated the $a - e$ plane of asteroids in the Sun-Jupiter-Saturn-asteroid system. For each pair of the initial conditions (a, e) we calculated the average value $\Delta L(t, a, e)$ for $t_{max} = 1000$ years:

$$\langle \Delta L(a, e) \rangle = \frac{1}{t_{max}} \sum_{i=1}^{t_{max}} \Delta L(i\Delta t, (a, e)), \tag{5}$$

and we assigned to each pair (a, e) the value $\langle \Delta L(a, e) \rangle$. This value is small for regular orbits, and larger for chaotic orbits, therefore a good visualization bf of

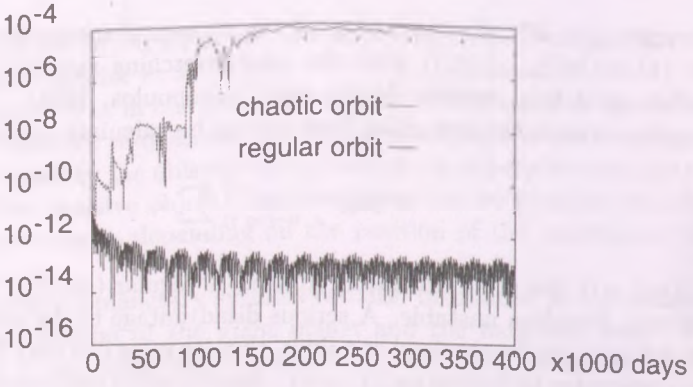

Figure 1: The evolution of $\Delta L(t, a, e)$ for a regular and a chaotic asteroidal orbit.

the dynamics can be obtained by using a gray scale representation in the $a - e$ plane, where light regions correspond to regular, while darker regions correspond to chaotic motions. The structure of the main belt of the asteroids is displayed in Figure 2a. In this figure we also show the osculating a and e values of about 7000 asteroids. It can be seen that the distribution of the asteroids is confined to the regular regions of the $a - e$ plane.

3. Dynamical map of the exoplanetary systems

The parameters of the studied systems are summarized in the table:

System	Mass of planet(s)	Orbital elements
HD 80606	$M_{\min} = 3.43 M_{\mathbf{Jup}}$	$a = 0.44\mathrm{AU}; e = 0.93$
70 Virginis	$M_{\min} = 7.42 M_{\mathbf{Jup}}$	$a = 0.48\mathrm{AU}; e = 0.40$
14 Herculis	$M_{\min} = 4.05 M_{\mathbf{Jup}}$	$a = 3.17\mathrm{AU}; e = 0.45$
ϵ Eridani	$M_{\min} = 0.88 M_{\mathbf{Jup}}$	$a = 3.36\mathrm{AU}; e = 0.60$
47 Ursae Maioris	$M_{\min,1} = 2.54 M_{\mathbf{Jup}}$	$a_1 = 2.09\mathrm{AU}; e_1 = 0.06$
	$M_{\min,2} = 0.76 M_{\mathbf{Jup}}$	$a_2 = 3.73\mathrm{AU}; e_2 = 0.10$

The observational method, based on the Doppler shift of the spectral lines of the central star, gives the quantity $M \sin i$ as the mass of the planet, which is its minimum value. Thus we performed our stability investigations with several masses. In our runs we used the following values: $M_1 = M \sin i$ as

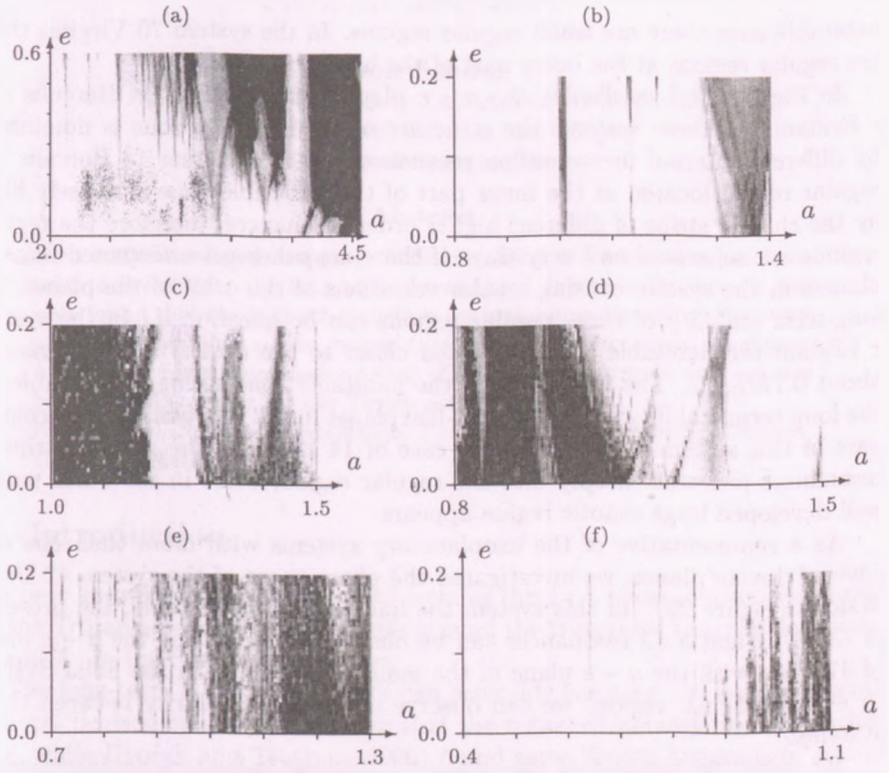

Figure 2: Dynamical map of the main asteroid belt in the Solar System (a), and of the habitable zones of the systems 47 UMa (b), HD 80606 (c), 70 Vir (d), 14 Her (e), and ε Eri (f).

minimal mass, $M_2 = \frac{4}{\pi} M \sin i$ as expected mass (obtained by integrating the angular momentum vector on a sphere), and $M_3 \approx 3.21 M \sin i$, in which case the probability that the real mass is larger than M_3 is 5%. Our results show that the use of the different masses M_i does not alter substantially the structure of the $a - e$ planes. As a minor difference we note that larger values of M_i resulted in the decreasing of the stability regions. In what follows, we show the dynamical maps of the studied systems obtained by using the mass M_2.

In Figures 2c,d the $a - e$ planes of the systems HD 80606 and 70 Virginis are shown. In the system HD 80606 it is unlikely the presence of terrestrial planets at small eccentricities. However, for larger eccentricities at the outer part of the

habitable zone there are small regular regions. In the system 70 Virginis there are regular regions at the outer part of the habitable zone.

In Figures 2e,f we display the $a - e$ plane of the systems 14 Herculis and ε Eridani. In these systems the structure of the habitabe zone is dominated by different internal mean-motion resonances. In the system 14 Herculis the regular region located at the inner part of the habitable zone is densely filled by the chaotic strips of different higher order resonances, therefore the regular regions are separated and very tiny. If there are other yet undetected massive planets in the system causing secular variations of the orbit of the planet, the long-term stability of these regular regions can be questioned. In the system ε Eridani the habitable zone is located closer to the central star (its mass is about $0.7 M_{\mathrm{Sun}}$). The inner part of the habitable zone seems to be stable, so the long-term stability of a terrestrial-like planet might be possible. The central part of this system is similar to the case of 14 Herculis, the chaotic strips of resonances penetrate deeply into the regular region, while in the outer part a well developed large chaotic region appears.

As a representative of the exoplanetary systems with more than one discovered Jovian planet, we investigated the phase space of the system 47 Ursae Maioris (Figure 2b). In this system the habitable zone is stable, the presence of the $3:1$ and $5:2$ resonances can be observed. Comparing the $a - e$ plane of 47 UMa with the $a - e$ plane of the main asteroid belt in the Solar System ($a \in [2.5, 3.5]$ AU region) we can observe dynamical similarity between these systems.

By using the method of the relative Lyapunov indicators we investigated the dynamical stability of different exoplanetary systems. We found that in some systems there are large regions of stable motion in the habitable zone. Thus from a dynamical point of view the presence of terrestrial planets in the habitable zones of some exoplanetary systems may be possible.

References

Kasting, J. F., Whitmire, D. P., and Reynolds, R. T.: 1993, *Icarus* **101**, 108

Sándor, Zs., Érdi, B., and Efthymiopoulos, C.: 2000, *Celest. Mech. & Dyn. Astron.* **78**, 113

Voglis, N and Contopoulos G.: 1994, *J. Phys. A* **27**, 4899

Some aspects of the chaotic diffusion of Trojan asteroids

Zsolt Sándor
Eötvös Loránd University, Department of Astronomy
H-1518 Budapest, P.O.Box 32., Hungary
E-mail: szsolt@astro.elte.hu

Abstract

A recently developed mapping model for the 1 : 1 resonance has been used to investigate the long term dynamics of Jupiter's Trojans. It has been found that the indirect planetary perturbations destabilize the outer part of the stability region, where there is a 13 : 1 secondary resonance. A conjecture has been risen up that this region might serve as a natural boundary of stability for the Trojan asteroids.
Keywords: *Symplectic mappings,* 1 : 1 *resonance, Trojan-type motion, Chaotic diffusion*

1. Introduction

The best known representatives of objects in the 1 : 1 mean-motion resonance are the Trojan asteroids, which librate around the triangular Lagrangian points L_4 and L_5 in the Sun-Jupiter system.

The long-term stability of the Trojan asteroids has been studied by several authors. Levison et al (1997) showed that the region of stability decreases with time, while Dvorak and Tsiganis (2000) found some Trojan asteroids in stable chaos being at the edge of strong chaos. Tsiganis et al (2000) showed also that (1868) Thersites could escape from the Trojan cloud with a quite high probability. These results indicate the presence of a slow chaotic diffusion at the boundary of the stability region.

In this paper we also study the long-term behaviour of Trojan-type dynamics. In our investigations we use a recently developed symplectic mapping model in the framework of the secularly changing planar elliptic restricted three-body problem (Sándor and Érdi, 2002).

In the next section we present the equations of the symplectic mapping and the most important of their derivation. (A detailed treatment of this mapping can be found in Sándor and Érdi, 2002.) In the third section we compare the phase space structure of the stability region in the cases of the circular, elliptic, and secularly changing elliptic restricted three-body problem.

2. Mapping model for Trojans

The symplectic mapping for the 1 : 1 resonance has been constructed by using the method suggested by Hadjidemetriou (1991), in which the averaged Hamiltonian is the generating function of the mapping. The Hamiltonian describing the motion of a massless body in the case of the 1 : 1 resonance is (Brown and Shook, 1964):

$$H = -\frac{1}{2(1+x)^2} - (1+x) - \frac{a'}{m_0+m'}R, \tag{1}$$

where R is the perturbing function:

$$R = m'\left(\frac{1}{\Delta} - \frac{1}{r} + \frac{1}{2}\frac{\Delta^2}{r'^3} - \frac{1}{2}\frac{r^2}{r'^3}\right), \tag{2}$$

m_0 and m' are the masses of the primaries P_0 and P_1 (assuming $m_0 >> m'$), r and r' are the distances of the massless body and the smaller primary from P_0, respectively, Δ is the distance of the massless body from P_1.

In the planar case the problem can be described by the following canonical variables:

$$x = \sqrt{\frac{a}{a'}} - 1\ ,\quad \tau = \lambda - \lambda'\ , y = \sqrt{\frac{a}{a'}}(\sqrt{1-e^2} - 1),\quad \varpi\ , \tag{3}$$

where a is the semi-major axis, e is the eccentricity, λ is the mean orbital longitude, ϖ is the longitude of the pericenter, and the primed quantities refer to the perturbing body. Keeping only the long-period terms the perturbation function up to second order in the eccentricities is (Brown and Shook, 1964):

$$\frac{a'}{m_0+m'}R = \mu R_0 + \mu e e' \sin(M - M')\frac{\partial R_0}{\partial \tau} + \\ + \mu[e^2 + e'^2 - 2ee'\cos(M - M')]\left(\frac{\partial^2 R_0}{\partial \tau^2} + \frac{\alpha^2}{4}\frac{\partial^2 R_0}{\partial \alpha^2}\right), \tag{4}$$

where $\mu = m'/(m_0+m')$, M and M' are the mean anomalies, $\alpha = a'/a = 1/(x+1)^2$, and $R_0 = \alpha(1+\alpha^2 - 2\alpha\cos\tau)^{-1/2} + 1/2 - \alpha^{-1}\cos\tau - \alpha$.

Since we study motions in the vicinity of the 1 : 1 resonance, we kept only the zero order terms in x in the above expansion:

$$\frac{a'}{m_0+m'}R = \mu R_{00} + \mu e' e_0 \sin(M - M')R_{0\tau} + \\ + \mu[{e_0}^2 + e'^2 - 2e'e_0\cos(M - M')]\left(R_{0\tau\tau} + \frac{1}{4}R_{0\alpha\alpha}\right), \tag{5}$$

where e_0 is the value of e at $x = 0$, the indices τ and α of R_0 denote partial derivation, and R_{00} is the value of R_0 at $x = 0$.

From Equations (1) and (5) we obtain an approximate averaged Hamiltonian $\bar{H}$, which can be used as the generating function of the mapping:

$$W = x_{n+1}\tau_n + y_{n+1}\varpi_n + \bar{H}(x_{n+1}, y_{n+1}, \tau_n, \varpi_n). \tag{6}$$

According to Hadjidemetriou (1991) the mapping can be obtained through the equations $x_{n+1} = \partial W/\partial\tau_n$, $y_{n+1} = \partial W/\partial\varpi_n$, $\tau_n = \partial W/\partial x_{n+1}$, and $\varpi_n = \partial W/\partial y_{n+1}$:

$$\begin{aligned}
x_{n+1} &= x_n + 2\pi\mu R_0'(\tau_n) + 2\pi\mu e' e_0(y_{n+1})\times \\
&\quad \times[\cos(\tau_n - \varpi_n + \varpi')R_{0\tau}(\tau_n) + \sin(\tau_n - \varpi_n + \varpi')R_{0\tau}'(\tau_n)] + \\
&\quad +4\pi\mu e' e_0(y_{n+1})\sin(\tau_n - \varpi_n + \varpi')[R_{0\tau\tau}(\tau_n) + \frac{1}{4}R_{0\alpha\alpha}(\tau_n)] + \\
&\quad +2\pi\mu[e_0(y_{n+1})^2 + e'^2 - 2e' e_0(y_{n+1})\cos(\tau_n - \varpi_n + \varpi')] \times \\
&\quad \times[R_{0\tau\tau}'(\tau_n) + \frac{1}{4}R_{0\alpha\alpha}'(\tau_n)], \\
\tau_{n+1} &= \tau_n + 2\pi\left[(1 + x_{n+1})^{-3} - 1\right], \\
y_{n+1} &= y_n - 2\pi\mu e' e_0(y_{n+1})\cos(\tau_n - \varpi_n + \varpi')R_{0\tau}(\tau_n) - \\
&\quad -4\pi\mu e' e_0(y_{n+1})\sin(\tau_n - \varpi_n + \varpi')[R_{0\tau\tau}(\tau_n) + \frac{1}{4}R_{0\alpha\alpha}(\tau_n)], \\
\varpi_{n+1} &= \varpi_n + 2\pi\mu e'\frac{y_{n+1} + 1}{e_0(y_{n+1})}\sin(\tau_n - \varpi_n + \varpi')R_0(\tau_n) + \\
&\quad +4\pi\mu(y_{n+1} + 1)[1 - \frac{e'}{e_0(y_{n+1})}\cos(\tau_n - \varpi_n + \varpi')] \times \\
&\quad \times[R_{0\tau\tau}(\tau_n) + \frac{1}{4}R_{0\alpha\alpha}(\tau_n)],
\end{aligned} \tag{7}$$

where the prime on the derivatives of R_0 denotes differentiation with respect to τ_n.

3. Chaotic diffusion at the boundary of the stability region

3.1. Mapping for the circular case $e' = 0$

As our previous investigations have shown (Sándor and Érdi , 2002), the mapping (7) can be efficiently used to study the phase space structure of the 1 : 1 resonance, and the long term behaviour of Jupiter's Trojans.

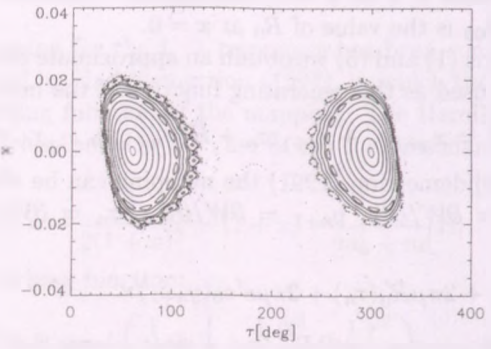

Figure 1: The structure of the phase space of the 1:1 resonance in the case of the circular restricted three–body problem ($e' = 0$) for $\mu = 0.001$ and $y = -0.002$.

As an application, here we present our results obtained by the mapping (7) for the location of the boundary of the stability region. First we investigated the resonant structure of the boundary of the stability region in the case of the circular restricted three-body problem, where the mapping (7) is reduced to a 2D mapping, thus it can be visualized easily. Setting $e' = 0$ in (7), we obtain a mapping for the co-orbital dynamics in the circular restricted problem:

$$\begin{aligned} x_{n+1} &= x_n + 2\pi\mu R_0'(\tau_n) + 2\pi\mu e(y)^2[R_{0\tau\tau}'(\tau_n) + \frac{1}{4}R_{0\alpha\alpha}'(\tau_n)], \\ \tau_{n+1} &= \tau_n + 2\pi[(1 + x_{n+1})^{-3} - 1]. \end{aligned} \tag{8}$$

In the circular case the parameters of the mappings are μ and y. In Figure 1 we displayed the phase space structure of the $1:1$ resonance for $\mu = 0.001$, corresponding to the Sun-Jupiter-asteroid system, and for $y = -0.002$. The properties of the mapping (8) for the circular case are the same as described in (Sándor et al 2001). The mapping (8) has three fixed points, two of them are stable at $x = 0$, $\tau = 60°$, $\tau = 300°$ ($\mathcal{L}_{4,5}$), and one ($\mathcal{L}_3$) is unstable at $x = 0$, $\tau = 180°$. These correspond to the Lagrangian solutions L_4, L_5, and L_3 of the real problem and therefore we refer to them as the Lagrangian fixed points of mapping (8).

Around the Lagrangian fixed points there are invariant circles corresponding to quasi-periodic librations around $L_{4,5}$ in the real, non-averaged system. In Figure 1 two chains of islands of the secondary resonances $13:1$ and $14:1$

between the long and short period part of Trojans' motion can be identified.

3.2. The elliptic and secularly changing case

In the case of the elliptic restricted three-body problem we kept $e' = 0.048$ and $\varpi' = 0$ constant. If we take into account the secular variations of e' and ϖ' due to the other massive planets of the Solar System, we can study the behaviour of Trojans in the secularly changing elliptic restriced three-body problem. (We note that in the case the Trojans the indirect perturbations seem to be more important than the direct ones, see Érdi, 1996, 1997.) The secular variations of e' and ϖ' are described by the theory of secular perturbations, see for instance the LONGSTOP numerical integration of the outer Solar System (Nobili et al., 1989). Thus the variation of e' and ϖ' can be easily calculated as a function of the time $t = iT$, where i is the ith iterate of the mapping and T is the period of Jupiter.

By applying the mapping (7) we studied the chaotic diffusion at the boundary of the stability region around L_4 for a large set of orbits and for various values of the initial osculating eccentricity e. We set $\tau = \varpi = \pi/3$, and we varied only x in the region $[0.013, 0.019]$ with a stepsize $\Delta x = 4 \times 10^{-5}$. (The corresponding y is calculated by using its definition.) We classified an orbit stable if it did not cross the axis of syzygium or equivalently if the condition $\tau < \pi$ held. Plotting the number of iterations N against x we can draw a curve for each initial e, showing the dependence of the stability on x. In Figure 2 we present the *curves of stability* obtained in this way for the case $e = 0.07$ and for $N_{max} = 10^7$ iterations (corresponding to 111.86 million years). The horizontal flat lines indicate stability for $N = N_{max}$. Figure 2a shows the curve of stability in the "pure" elliptic case (e', ϖ' are fixed), while in Figure 2b the curve of stability is displayed when e' and ϖ' are secularly changing. Studying Figure 2 we can conclude that in the case of the secularly changing elliptic problem the stability region of Trojans is smaller, than in the elliptic case. We also found that the orbits becoming unstable emerge from that region which contains the chain of islands of the 13 : 1 secondary resonance. (This chain of islands can be seen in Figure 1.) According to our experiences the secular variation of e' and ϖ' results in a destabilizing effect, a significant number of orbits becomes unstable in the region of the secondary resonance after $N = 10^6 - 10^7$ iterations of the mapping (7). This indicates that the chain of the 13 islands is partly destroyed by the variation of e' and ϖ'.

Thus we can conject that the stability region of Trojan asteroids is bounded by the islands of the 13 : 1 secondary resonance.

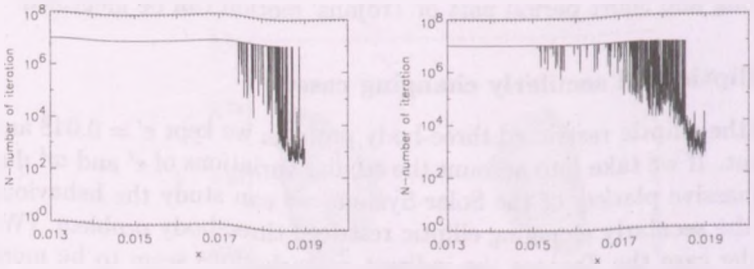

Figure 2: Boundary of the stability region around L_4 for $e = 0.07$ and for $N_{max} = 10^7$ iterations of the mapping (7); elliptic case left picture, secularly changing case right picture.

References

Brown, E. W. and Shook, C. A.: 1964 *Planetary Theory*, Dover Publications, New York.

Dvorak, R. and Tsiganis, K.: 2000, *Celest. Mech. & Dyn. Astron.* **78**, 125.

Érdi, B.: 1996, *IAU Symp.* **172**, 171.

Érdi, B.: 1997, *Celest. Mech. Dyn. Astron.* **65**, 149.

Hadjidemetriou, J. D.: 1991, in: A. E. Roy (ed.) *Predictability, Stability, and Chaos in N-body Dynamical Systems*, Plenum Press, New York, pp.157-175.

Levison, H., Shoemaker, E. M., and Shoemaker, C. S.: 1997, *Nature* **385**, 42.

Nobili, A. M., Milani, A., and Carpino, M.: 1989, *Astr. Astrophys.* **210**, 313.

Sándor, Zs., Érdi, B., and Murray, C. D.: 2002, *Celest. Mech. Dyn. Astron.* (accepted)

Sándor, Zs. and Érdi, B.: 2002, *Celest. Mech. & Dyn. Astron.* (submitted)

Tsiganis, K., Dvorak, R., and Pilat-Lohinger, E: 2000, *Astr. Astrophys.* **354**, 1091.

The fundamental frequencies of N-body systems

Áron Süli[1] and Rudolf Dvorak[2]
[1]Eötvös Loránd University, Department of Astronomy
H-1518 Budapest, P.O.Box 32., Hungary
[2]Institut für Astronomie der Universität Wien
Türkenschanzstraße 17, A-1180 Wien, Austria
E-mail:[1]saron@astro.elte.hu,[2]dvorak@univie.astro.ac.at

Abstract

In this article we determine the fundamental frequencies of different planetary systems similar to our Solar System configuration – but with larger masses for the planets – as possible model for exosolar systems. For this purpose we have implemented the Laplace-Lagrange theory (1st order secular theory) in the MAPLE computer algebra program. Two different models were investigated: one where the planets Venus, Earth and Mars had masses up to the one of Jupiter, and a second one where the inner planets were given the actual masses, but the giant planets Jupiter and Saturn had significantly larger masses. The respective results showed a simple linear increase in the fundamental frequencies (nodes and perihelion longitudes) with increasing masses.
KEYWORDS: *exosolar systems – fundamental frequencies – 1st order secular theory*

1. Introduction

Laplace and Lagrange (1781) developed an analytical theory to describe the motion of the outer planets. This approach was also used by Le Verrier (1855), Stockwell (1873) and Harzer (1895) and took into account only linear terms of the perturbation function These authors essentially differed in their choices of variables, and the gradual improvements they brought came from the better determinations of the planetary masses.

More recently Bretagnon (1974) computed the solution of the very long period terms with an iterative procedure through 3^{rd} degree and 2^{nd} order with respect to the masses. He improves this solution later on by considering in particular the effects of the Moon and relativity (Bretagnon, 1984).

The most advanced work with respect to the regarded time interval is that of Laskar (1986) who analyticaly computed the averaged differential system and

integrated then numerically giving the secular variations of the orbital elements for the 8 major planets (order 2 with respect to the masses and degree 5 in the eccentricity-inclination variables).

In this paper we briefly review the Laplace-Lagrange secular theory (section 2). We have implemented this method in the MAPLE computer algebra software in order to calculate the fundamental frequences of any arbitrary planetary system with one major dominating mass. Recently Dvorak & Süli (2002) investigated the stability of our simplified Solar System as a model for exosystems, where they found that the systems only decay for significantly larger masses of the inner planets Venus, Earth and Mars. In section 3 we determine the fundamental frequencies of these systems, and show how the frequences vary with the mass factor κ (this factor was used to uniformly increase the masses of the planets).

2. Laplace-Lagrange secular theory for the planetary system

In this analytical theory the main idea is that the Lagrange equations are solved for the secular part of the perturbing function which means that the periodic terms that contain the mean longitude of the planets in their arguments are ignored. Furthermore, the solution is in this first step limited to the terms in the secular part of the second order in small parameters eccentricities and inclinations. Because the indirect part of the disturbing function does not contain any secular terms only the direct part has to be taken into account. These assumptions lead to a relatively simple set of differential equations with constant coefficients, that can be solved with trigonometric functions. Accordingly with this secular theory the long period variations of e, i, $\tilde{\omega}$ and Ω can be determined. We suppose the semi-major axis to be constant $a_i = const., i = 1, 2 \ldots, n$, (that is a consequence of using only the secular part of the disturbing function). Let us assume we have a system consisting of the Sun and n planets.

The solution of the secular perturbation for such a dynamical system takes the following form (Brouwer and Clemence, 1961)

$$h_s = \sum_{j=1}^{8} L_s^{(j)} \sin(g_j t + \beta_j) \qquad k_s = \sum_{j=1}^{8} L_s^{(j)} \cos(g_j t + \beta_j) \tag{1}$$

where $L_s^{(j)}$ and β_j are the amplitudes and phases. Similiar equations are valid

for p_s and q_s. The coefficients $L_s^{(j)}$ are functions of the initial $e, \bar{\omega}$. In the above expressions g_j are the eigen frequencies, which are obtained from the following secular equations:

$$|\underline{A} - g \cdot \underline{E}| = 0 \tag{2}$$

where $\underline{A}$ is an $n \times n$ symmetrical matrix, of which element A_{ij} are functions only of the semi-major axis and the masses of n planets, and $\underline{E}$ is the unit matrix.

The values of g_j and f_j obtained in this solution (O1D1) are given in Table I. All the g's are positive, as a result the orbits are rotating prograde, while the f's are negative and therefore the orbital planes are rotating in the retrograde direction.

Fundamental frequencies derived by different approaches are given for the sake of a comparison in Table I. One can see that the solutions of O1D1 and BVW are very similiar, for BVW is basically a solution of O1D1 with additional terms of second order up to degree 5 in e coming from the great inequality of the pair Jupiter Saturn. The solutions of Bretagon (1984) is very close to that of NGT (Numerical General Theory), but there are still differencies caused on one side by the limitation with respect to small parameters (Laskar) and on the other side Bretagnons theory lacks higher orders in the masses. To improve the theory and incorporate higher degree terms in the eccentricity- inclination variables as well as higher order terms with respect to the masses is a task which has been started recently (Dvorak et al., 2002)

Table 1: Comparison of the fundamental frequencies of the Solar System obtained with different solution. Unit is arcsec/year.

O1D1	Solution of order 1 and degree 1 (present work)
BVW	Brouwer and Van Woerkom, 1950
B84	Bretagnon, 1984. Order 2, degree 3
NGT	Laskar, 1986. Order 2, degree 5

	O1D1	BVW	B84	NGT		O1D1	BVW	B84	NGT
g_1	5.4615	5.4633	5.6136	5.5689	f_1	-5.2007	-5.2015	-5.6109	-5.6043
g_2	7.3459	7.3447	7.4559	7.4555	f_2	-6.5701	-6.5708	-6.7710	-7.0530
g_3	17.3307	17.3283	17.2852	17.3769	f_3	-18.746	-18.7436	-18.8293	-18.8499
g_4	18.0042	18.0042	17.9025	17.9217	f_4	-17.636	-17.6333	-17.8188	-17.7614
g_5	3.7108	4.2959	4.3080	4.2489	f_5	0.0	0.0	0.0	0.0
g_6	22.2850	27.7741	27.1483	27.9606	f_6	-25.739	-25.7335	-26.2090	-26.3300
g_7	2.7013	2.7193	3.1534	3.0695	f_7	-2.9037	-2.9027	-2.9998	-2.9854
g_8	0.63328	0.6333	0.6735	0.6669	f_8	-0.6777	-0.6775	-0.6914	-0.6917

3. Fundamental frequencies as a function of the masses

Our dynamical model consists of the Sun, the three inner planets (Venus, Earth and Mars VEM), Jupiter and Saturn (JS). The masses of the inner planets were increased uniformly by multipling a mass factor, κ. We integrated in a preceding study each of these modified models of the actual Solar System with the Lie-integrator for 10^7 million years. The frequencies present in the system were determined by means of a precise analysis with a very sophisticated program by Chapront (1995). The respective results are discussed in Dvorak and Süli (2002). In the following we determine these frequencies with the aid of the MAPLE program which we have constructed; we thus can show how the fundamental frequencies vary with the masses involved.

These frequencies are listed in Table II. We note that these values are very close to that of Table I, where the complete Solar System was taken into account.

Table 2: Fundamental frequencies of the simplified Solar System from Venus to Saturn (g_i and f_i, i=2,6 from table 1 in the same units)

	Venus	Earth	Mars	Jupiter	Saturn
g	7.179103	17.25891	17.96289	3.493038	22.08120
f	-6.146103	-18.66197	-17.60199	0.0	-25.56508

3.1. A simple solution

Let us denote $g_1, g_2, \ldots g_5$ the solution of $|\underline{A} - g \cdot \underline{E}| = 0$ where $\underline{E}$ is the unit matrix, and examine first the frequencies when we uniformly increase the masses of all the planets. Let $\tilde{m}_l := \kappa \cdot m_l \quad l = 1, 2 \ldots 5$. One can easily calculate that the modified systems coefficient matrix ($\underline{\tilde{A}}$) is $\tilde{A}_{jl} := \kappa \cdot A_{jl}$. The new frequencies of this modified system can be easily determined:

$$|\underline{\tilde{A}} - g^* \cdot \underline{E}| = \kappa^5 |\underline{A} - \frac{g^*}{\kappa} \cdot \underline{E}| \quad = \quad 0 \tag{3}$$

$$g^{**} := \frac{g^*}{\kappa} \Rightarrow |\underline{A} - g^{**} \cdot \underline{E}| = 0 \tag{4}$$

Comparing equation (4) with the original systems secular equation (2) it is evident that $g_j^{**} = g_j,\ j = 1, 2 \ldots 5 \Rightarrow g_j^* = \kappa \cdot g_j,\ j = 1, 2 \ldots 5$

According to the structure of the solution these frequencies depend linearly on κ. This feature can be seen in Fig 1. Unfortunately the linear theory which we use is not capable of determining a stability limit for the mass paramter κ.

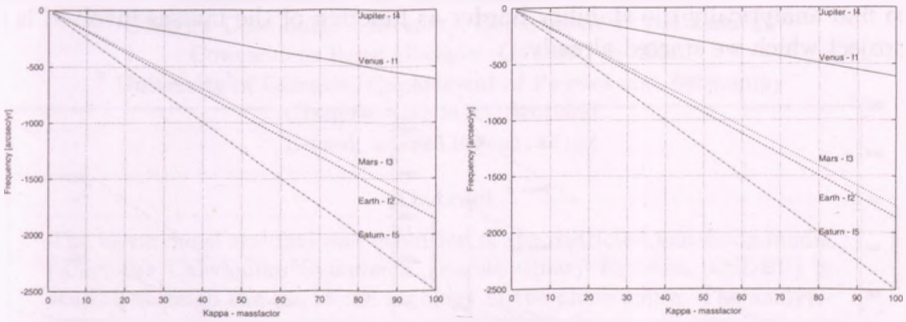

Figure 1: Each planets mass was magnified. The linearity is very well visible.

3.2. Frequencies versus κ

First we pay attention to the inner planets. We magnify their masses and using our MAPLE application we calculate the fundamental frequencies of this system. The results can be seen in Fig 2. The frequencies again depend linearly on κ; g_4 and g_5 are not visible in Fig 2. because they vary only very little (but linear!).

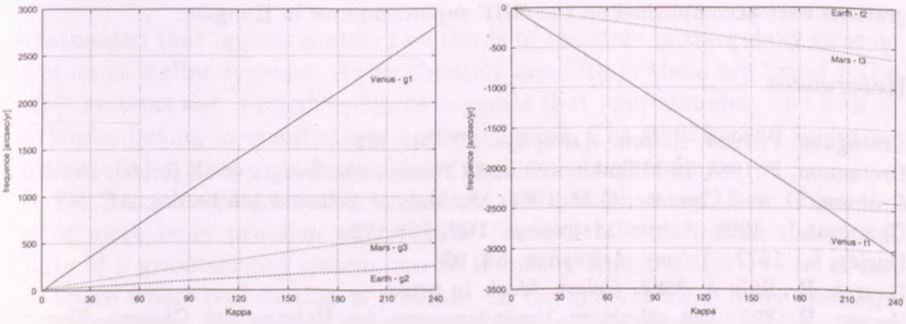

Figure 2: The frequencies of Venus, Earth and Mars. Only the mass of the VEM was increased.

In another test we increased the mass of the Jupiter-Saturn pair, and again

we plotted the frequencies against κ. Once more all the g and f depend linearly on κ!

These results are the first step for an analytical determination of the dependance of these frequencies on the masses of the system; the next step to be able to find analytically the stability border as function of the masses involved is a project which we started already.

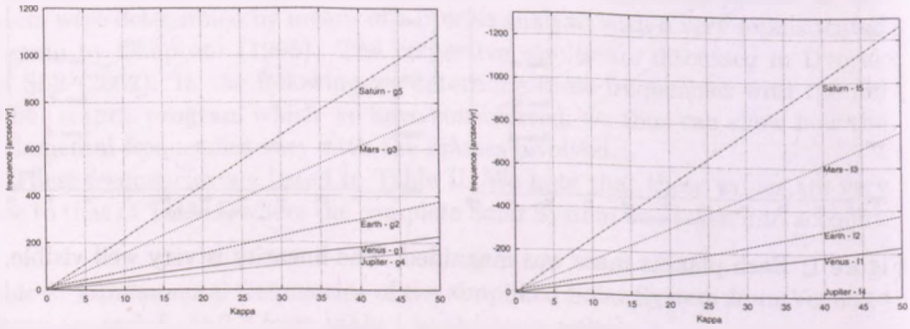

Figure 3: The frequencies of the planets. Only the mass of the JS pair was increased.

Acknowledgements

We express thank to B. Érdi for his fruitful discussions. Some of the numerical integrations were accomplished on the NIIF supercomputer in Hungary.

References

Bretagnon, P.:1984, *Astron. Astrophys.* **30**, 341-362
Bretagnon, P.:1984, in Milankovitch and Climate, eds. Berger et al, Reidel, Dordrecht
Brouwer, D. and Clemece, G.M.,1961, Methods of Celestial Mechanics, AC, NY
Chapront,J.: 1995, *Astron. Astrophys.* **109**, 181-192
Duriez, L.: 1977, *Astron. Astrophys.* **54**, 93
Dvorak, R., Süli, Á.:2002, *Celest. Mech.* in press
Harzer, P.:1895, Die säkuleren Veränderungen der Bahnen der Grossen Planeten, Leipzig, Preisschrift
Le Verrier, U.J.J.:1855-1876, Annales de l'Observatorie de Paris
Laskar, J.:1985 *Astron. Astrophys.* **144**, 133-146

Numerical Investigation of the Phase Space of the Caledonian Symmetric Double Binary Problem

András Széll[1], **B. A. Steves**[1], **A. E. Roy**[2]
[1] Glasgow Caledonian University, Department of Mathematics
Cowcaddens Road Glasgow, G4 0BA, Scotland
[2] University of Glasgow, Department of Physics and Astronomy
Glasgow, G12 8QQ, Scotland
E-mail: a.szell@gcal.ac.uk

Abstract

The hierarchical stability and evolution of the restricted four-body model called the Caledonian Symmetric Double Binary Problem (CSDBP) is studied through the use of the topology of the phase space. The analytical stability criterion derived for the CSDBP by Steves and Roy (2001) is verified numerically for the coplanar CSDBP. Numerical integrations were performed for a wide range of initial conditions and a variety of values of Szebehely's constant C_0, a combination of the total energy and angular momentum of the system. These show that for $C_0 > C_{0_{crit}}$ the systems undergo no change in their hierarchical arrangement, as predicted by the analytical stability criterion. They are therefore considered to be hierarchically stable.

Keywords: *four-body problem, hierarchical stability*

1. Introduction

It is estimated that approximately two thirds of the stars in the galaxy exist as part of multi-stellar systems. Approximately one-fifth of these are found to be in triple systems and a rough estimate suggests that approximately one-fifth of these triples belong to quadruple or higher systems. The stability and evolution of multi-stellar systems is a fundamental problem of astronomy.

It has been long-known that there are not enough integrals to solve the three or more body problem analytically; however information on the global stability of a gravitational system can be found by studying the regions of the phase space where real motion is possible. In the general three body problem, Zare, (1976, 1977) and Marchal and Saari (1975) showed that the energy H and angular momentum c integrals combine to form a stability criterion c^2H which, for a given critical value c^2H_{crit}, produces a phase space for the three body

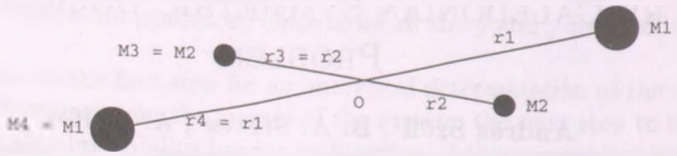

Figure 1: The Caledonian Double Binary configuration.

system which contains topologically separate sub-regions. Thus the hierarchical arrangement of the system which exists in one sub-region of real motion cannot physically evolve into the hierarchical arrangement of the system existing in another sub-region of real motion. In this situation the system can be said to be hierarchically stable for all time.

The large number of degrees of freedom in the four or more few body problems, make stability criteria of this form difficult to formulate. Recently, Roy and Steves (2001) have developed the Caledonian Symmetrical Double Binary Problem (CSDBP), a symmetrical four-body problem which utilises all possible symmetries so that it can easily be studied in 3- dimensional space. In this special symmetric problem, they have discovered a stability criterion Steves and Roy, (2001), based on a similar combination of the energy E and angular momentum c integrals. They show that the stability and possible evolutions of the symmetric four body system can be predicted solely from knowledge of the total energy and angular momentum of the system.

In this paper, we numerically integrate a wide range of coplanar CSDBP systems with differing total energy and angular momenta. By cataloguing the changes in the hierarchical arrangements of these systems, we can verify the validity of the analytical stability criterion in its ability to predict when a system will be hierarchically stable. Any system which does not change its hierarchical arrangement over a very long time period is defined to be hierarchically stable.

2. The Caledonian Symmetric Double Binary Model

The Caledonian Symmetric Double Binary problem is defined as follows. Let $\vec{r}_1, \vec{r}_2, \vec{r}_3, \vec{r}_4, \dot{\vec{r}}_1, \dot{\vec{r}}_2, \dot{\vec{r}}_3, \dot{\vec{r}}_4$ be the radius and velocity vectors of the four bodies measured with respect to the system's centre of mass. Let m_1, m_2, m_3, m_4 be the masses of the four bodies. In the CSDB model, all dynamical symmetries are utilised so that $\vec{r}_1 = -\vec{r}_4$, $\vec{r}_2 = -\vec{r}_3$, and $\dot{\vec{r}}_1 = -\dot{\vec{r}}_4$, $\dot{\vec{r}}_2 = -\dot{\vec{r}}_3$, and $m_1 = m_4$, $m_2 = m_3$ (Fig. 1). Initially the bodies are placed on a

line, in positions symmetrical to their center of mass. The initial velocities are also symmetric about the centre of mass and are directed perpendicular to the initial line formed by the bodies. These conditions mean the system begins in a mirror configuration Roy and Ovenden, (1955), ensuring that the evolution of the system is dynamically symmetric for positive or negative time values.

Introducing new variables $r_1 = |\vec{r}_1| = |\vec{r}_4|$, $r_2 = |\vec{r}_2| = |\vec{r}_3|$, $r_{12} = |\vec{r}_2 - \vec{r}_1|$, and $M = m_2$, $\mu = m_1/m_2$, the potential function of the system may be written as

$$U = -M^2 \left(2\mu \left(\frac{1}{r_{12}} + \frac{1}{\sqrt{2(r_1^2 + r_2^2) - r_{12}^2}} \right) + \frac{1}{2} \left(\frac{1}{r_2} + \frac{\mu^2}{r_1} \right) \right) ,$$

where units are chosen so that the gravitational constant $G = 1$. The total energy may be written as

$$E = T + U = \mu M \dot{\vec{r}}_1^2 + M \dot{\vec{r}}_2^2 + U(r_1, r_2, r_{12}) .$$

The energy integral can be used to derive surfaces of zero velocity in the r_1, r_2, r_{12} phase space which separate regions where the velocity is real from regions where the velocity is imaginary. Steves and Roy, (2001).

More restrictive boundary conditions for the regions of real motion can be determined using the Sundmann's inequality:

$$c^2 \leq 2IT ,$$

where c is the angular momentum, I is the moment of inertia of the system, and T is the kinetic energy . For the CSDB problem, $T = 2M(\mu r_1^2 + r_2^2)$. Roy and Steves (2001) derive useful information on the stability of the CSDBP from an examination of the projection of the boundary surface in r_1, r_2 and r_{12} space onto the r_1-r_2 plane.

3. The stability criterion using Szebehely's Constant

Steves and Roy (2001) show that the topology of the phase space r_1, r_2 and r_{12} depends solely on a constant they call Szebehely's constant where

$$C_0 = \frac{c^2 E_0}{G^2 M^5}$$

($E_0 = -E$). Depending on the value of C_0, the projection onto the r_1-r_2 plane of the boundary surface can separate into disconnected curves which indicate

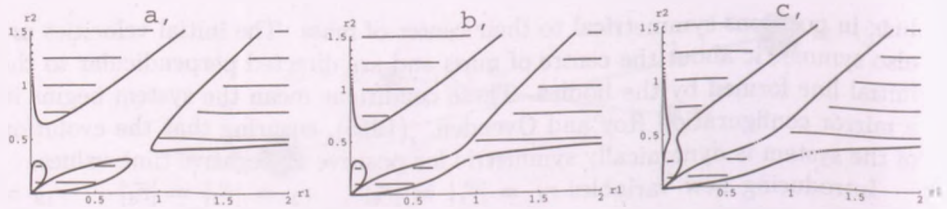

Figure 2: The projection of the phase space onto the r_1-r_2 plane for the case of a mass ratio of $\mu = 0.1$ where graphs a, b and c are for a range of values of $C_0 = 0.77$, 0.8, 0.9 respectively. The shaded regions denote regions where motion is not allowed.

the whole phase space becomes disconnected. Fig 2 shows the projection of the phase space onto the r_1 - r_2 plane for specific values of Szebehely's constant C_0. The greater the value of C_0, the more disconnected the phase space projection becomes until for a critical value of $C_{0_{crit}}$, the phase space becomes totally disconnected and evolution from one hierarchy to another is impossible, ensuring hierarchical stability for all time.

Each separate region in the r_1, r_2, r_{12} phase space describes a particular hierarchical arrangement of the four body system. The dynamical system can be found in one of four different hierarchy states:

"12" type hierarchy. The P_1 P_2 bodies and the P_3 P_4 bodies form binaries which orbit around the baricenter of the four-body system.

"13" type hierarchy. The P_1 P_3 bodies and P_2 P_4 bodies form binaries which orbit around the baricenter of the four-body system.

"23" type hierarchy. The P_2 P_3 bodies form a central binary and the P_1 and P_4 bodies orbit around it.

"14" type hierarchy. The P_1 P_4 bodies form a central binary and the P_2 and P_3 bodies orbit around it.

For example, in Figure 2 c, the allowed region of motion where r_2 is small and r_1 can be large depicts the "23" type hierarchy.

4. Numerical Results

Numerical investigations were carried out in order to verify the Steves and Roy (2001) analytical stability criterion for the CSDBP. The evolution of hierarchical arrangements of CSDBP systems with differing initial conditions in r_1, r_2, $\dot{r}_1$, $\dot{r}_2$ but the same Szebehely constant were studied. Each numerical integration

Table 1: The number of hierarchy changes

$\mu =$	1						$\mu =$	0.1				
$C_0 =$	10	29	30	40	46	47	0.4	0.6	0.65	0.7	0.8	0.9
$12 \rightarrow 23$	8	3	3	1	0	0	14	20	15	25	2	0
$12 \rightarrow 14$	3	8	1	1	1	0	40	13	20	21	1	0
$13 \rightarrow 23$	2	3	2	0	0	0	13	15	21	9	0	0
$13 \rightarrow 14$	2	0	3	0	0	0	14	20	22	28	0	0
$23 \rightarrow 12$	10	15	21	3	1	0	46	25	25	26	0	0
$23 \rightarrow 13$	10	13	20	7	0	0	24	34	27	26	0	0
$23 \rightarrow 14$	678	261	247	90	0	0	575	303	250	155	3	0
$14 \rightarrow 12$	8	1	1	0	0	0	33	29	40	39	2	0
$14 \rightarrow 13$	6	4	2	0	0	0	26	33	35	37	2	0
$14 \rightarrow 23$	527	185	165	52	0	0	463	222	156	92	1	0
$12 \rightarrow 13$	0	0	1	0	0	0	1	2	3	6	0	0
$13 \rightarrow 12$	0	0	1	0	0	0	4	2	1	4	1	0

was carried out until one of the following events occurred: a close encounter in which the energy integral showed change in value, at least 2 of the bodies escaped the system, or time span of 4 million time steps equivalent to 1.5×10^6 yrs was completed.

If a system changed its hierarchy state frequently, then the system was said to be chaotic. If it didn't change its hierarchy state at all over the integration time span, then it was said to be hierarchically stable.

Tables 1 and 2 show the number of hierarchy changes for four different values of the mass ratio μ , namely $\mu = 1, 0.1, 0.01, 0.001$. Over 1500 different initial conditions, all of which formed the same Szebehely's constant C_0 were numerically integrated to produce the results listed in each column of Tables 1 and 2.

The critical values of C_0 which give hierarchical stability for all time are derived from the analytical stability criterion of Steves and Roy (2001) to be 46.842, 0.888, 0.286, 0.254 for $\mu = 1, 0.1, 0.01, 0.001$ respectively. The numerical investigations show that when C_0 is increased beyond these critical values, the number of hierarchy changes is reduced to zero, confirming the validity of the Steves and Roy stability criterion. Numerical investigations also confirm that the CSDB system is more stable, ie it undergoes fewer hierarchical changes, as

Table 2: The number of hierarchy changes

$\mu =$	0.01					$\mu =$	0.001		
$C_0 =$	0.2	0.27	0.283	0.29	0.3	0.25	0.2525	0.253	0.2538
$12 \rightarrow 23$	2	3	0	0	0	0	0	0	0
$12 \rightarrow 14$	0	4	1	1	0	0	0	0	0
$13 \rightarrow 23$	3	2	1	0	0	3	1	0	0
$13 \rightarrow 14$	2	1	3	2	0	0	0	2	0
$23 \rightarrow 12$	4	7	5	1	0	0	0	0	0
$23 \rightarrow 13$	4	4	3	1	0	3	1	2	0
$23 \rightarrow 14$	95	41	14	2	0	56	10	5	0
$14 \rightarrow 12$	0	5	0	5	0	0	1	0	0
$14 \rightarrow 13$	1	0	3	6	0	0	1	1	0
$14 \rightarrow 23$	91	31	13	2	0	49	4	1	0
$12 \rightarrow 23$	0	0	1	4	0	0	0	0	0
$13 \rightarrow 12$	0	0	0	4	0	0	0	0	0

μ is decreased.

References

Marchal C and Saari D G, 1975, *Celest Mech* **12** 115.

Roy A E and Ovenden M W, 1955, *Mon Not Roy Astron Soc* **115**, 296 On the occurrence of commensurable mean motions in the solar system. The mirror theorem

Roy A E and Steves B A, 2001, *Celest Mech* **78** 299.

Steves B A and Roy A E, 2001, *in The Restless Universe: Application of Gravitational N-Body Dynamics to Planetary, Stellar and Galactic Systems*, eds. B. A. Steves and A. J. Maciejewski, IOP Publishing, Bristol, 301 - 325.

Zare K, 1976, *Celest Mech* **14** 73.

Zare K, 1977, *Celest Mech* **16** 35.

Extragalactic Astronomy

S. Frey
Zs. Győri
Cs. Kiss
L. Mosoni
Zs. Paragi

VLBI IMAGING OF WEAK EXTRAGALACTIC RADIO SOURCES

Sándor Frey[1] **and László Mosoni**[2]
FÖMI Satellite Geodetic Observatory
H-1373 Budapest, P.O. Box 546, Hungary
E-mail:[1]frey@sgo.fomi.hu,[2]mosoni@sgo.fomi.hu

Abstract

The improving sensitivity of the Very Long Baseline Interferometry (VLBI) arrays and the phase-referencing technique enable us to image mJy radio sources with milliarcsecond angular resolution. The potential targets can be orders of magnitude fainter than those objects traditionally imaged with VLBI. These include weak nuclei of large radio galaxies, radio-quiet quasars, distant but relatively luminous, or nearby low-luminosity active galactic nuclei. Here we briefly mention the most recent studies and outline the concept and initial results of the Deep Extragalactic VLBI-Optical Survey (DEVOS).
KEYWORDS: *techniques: interferometric – radio continuum: galaxies – galaxies: active – quasars: general – astrometry*

1. Introduction

In the last 35 years, VLBI images of up to a few thousand extragalactic radio sources (compact active galactic nuclei, AGNs) have been made with milliarcsecond (mas) angular resolution. The sample available is clearly just the tip of the iceberg. Although inhomogeneous in terms of observing parameters, the sample is in fact flux density limited, as illustrated in Fig. 1. The reason in principle is the sensitivity limit of the VLBI networks. In order to study the intrinsic physical properties of the sources as well as possible effects of cosmological models on the appearance of the objects, it is essential to image more distant ($z > 1$) sources with luminosities similar to those of nearby ($z \sim 0.1$) AGNs.

During the last couple of years, there have been successful attempts to enter the "unexplored region" of the radio luminosity–redshift space (Fig. 1). These observations (Garrington et al. (2001), and references therein) utilize the increasing sensitivity (observing bandwidth) of VLBI, and routinely apply the phase-referencing technique. The main scientific drivers are to understand the

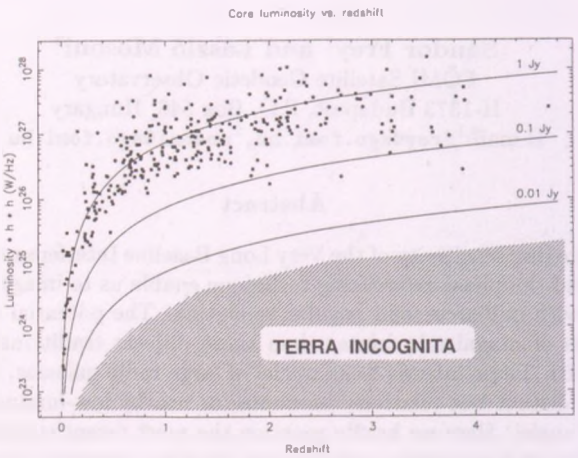

Figure 1: Luminosity (Lh^2) as a function of redshift for the sample of 330 sources (almost exclusively AGNs) at $\nu = 5$ GHz (rest-frame) frequency, adopted from Gurvits et al. (1999). The solid lines show luminosities of sources with flux density (S) of 1, 0.1 and 0.01 Jy, calculated assuming spectral index $\alpha = 0$ ($S \sim \nu^{\alpha}$). The plot indicates a strong luminosity selection effect in VLBI samples presently available.

evolution of galaxies and AGNs, in the light of the orientation-dependent unification models. Interferometric observations can distinguish between the different origins of radio emission (nuclear activity or startburst). VLBI images of thousands of optically identified AGNs could possibly be used to constrain the fundamental cosmological parameters Ω_m and Ω_Λ (Gurvits et al. (1999), and references therein). Owing to the positional accuracy of VLBI, astrometric data on a large sample of radio sources is essential to establish a precise, directly linked radio and optical celestial reference frame, through cross-identification of the optical targets of next-generation space astrometry missions (Fey et al., 2001).

A recent spectacular example of high resolution imaging of faint radio sources is the European VLBI Network (EVN) detection of three weak (100μJy-level) sources in the region of the Hubble Deep Field (Garrett et al., 2001). A low-

luminosity FR-I radio source ($z = 1.01$), a red spiral galaxy ($z = 0.96$) and a dust-obscured, nuclear starburst galaxy ($z = 4.42$) represent the variety of faint objects that can be studied with VLBI. The detection of compact radio-emitting regions in these sources suggest that they all harbour an embedded AGN.

2. Deep Extragalactic VLBI-Optical Survey (DEVOS)

In order to obtain mas-scale radio structure information on many ($\sim 10^4$) extragalactic radio sources, a dedicated survey is being proposed. For statistical studies concerning the cosmological evolution of the objects, and for the possible cosmological tests, it is essential that the sources have optical identifications and measured spectroscopic redshifts. These will be provided by the Sloan Digital Sky Survey, e.g. Stoughton et al. (2002), within the next couple of years. In the radio regime, the project would require a large amount of interferometer network observing time. Therefore a carefully selected sample and an effectively designed observing setup is needed to optimize the usage of the resources.

The DEVOS observing scheme, originally applied by Garrett & Garrington (1998) and Garrington et al. (1999), is based on the idea of selecting radio sources that are compact (unresolved) on arcsecond scale in the FIRST survey (White et al., 1997). The FIRST survey is being conducted with the US National Radio Astronomy Observatory (NRAO) Very Large Array (VLA) at 20 cm wavelength. Currently it contains about 800,000 sources down to 1 mJy flux density level, imaged with 5" resolution. For DEVOS, we select sources that are *unresolved* in the FIRST survey and stronger than 30 mJy. These sources are then observed with the Multi-Element Radio Linked Interferometer (MERLIN), an array of radio telescopes in Great Britain with a maximum antenna separation of 217 km. The angular resolution of MERLIN at 6 cm (5 GHz frequency) is ~ 50 mas. The objects that appear compact or unresolved with MERLIN are good candidates for future VLBI observations, most likely showing sufficient radio emission to be detected with 50 times better angular resolution.

The suitable observing technique to image faint sources with MERLIN (and VLBI) is the phase-referencing, e.g. Beasley & Conway (1995). It allows the determination of interferometric delay, delay-rate and phase corrections by interleaving observations of a nearby, strong calibrator object. Switching cycles of a few minutes and target–reference source separations of a few degrees are sufficient to image mJy radio sources. A key strategy for DEVOS is to select *the phase-reference source first*, then to look for potential target sources in its close

vicinity (within 2°). This allows us to minimize the time spent with telescope slewing. There are many suitable reference sources known, the most complete collection is found in the NRAO Very Long Baseline Array (VLBA) Calibrators List (http://magnolia.nrao.edu/vlba_calib). Therefore a sufficiently large sample of weak objects can be constructed this way.

3. Results of the MERLIN pilot observations

As the first step of a pilot survey for DEVOS, 5-GHz MERLIN observations of 89 sources were conducted in March 2001. The sample was selected from the FIRST survey, according to the following criteria: flux density at 1.4 GHz $S_{1.4} \geq 30$ mJy, angular size $\theta \leq 5$ ", angular distance from the refrence source $\delta \leq 2°$. The two phase-reference calibrator sources were the quasars J1549+0237 (nearly equatorial; Mosoni 2002, these proceedings) and J1257+3229 (close to the North Galactic Pole, NGP). This target-finding "filter" observation led to the identification of 41 and 28 compact sources stronger than ~ 2 mJy MERLIN peak flux density, out of the 47 and 42 objects in the NGP and the equatorial fields, respectively. Also, due to the phase-referencing technique and the accurate positional information available for the reference sources, the astrometric position of these mJy-level sources is considerably improved. This minimizes the chance of false VLBI detections. The objects found are suitable for VLBI phase-referencing observations. Based on earlier experience, it is likely to successfully image a large portion, up to 80% of the MERLIN-detected sources with VLBI (Garrington et al., 1999). MERLIN images of two sources are shown in Fig. 3 as an example.

4. Future VLBI observations

The DEVOS pilot observations of the 41 pre-selected faint sources in the field around J1257+3229 (NGP) will most likely take place in mid-2002 using a global VLBI network formed by the VLBA and the EVN at 5 GHz. By means of these observations, we would like to confirm the feasibility of the source selection method, to assess the amount of network resources and manpower required, to adjust the observing strategy and to experiment with the data reduction before the full-scale DEVOS is started. However, mas-resolution images of ~ 30 faint extragalactic radio sources, together with the sample of Garrington et al. (1999), would also allow scientific studies, such as the investigation of a hypothetic dependence of source compactness on luminosity.

Acknowledgements

The DEVOS project is a collaborative effort with L.I. Gurvits, M.A. Garrett, S.T. Garrington and Z.I. Tsvetanov. We acknowledge partial financial support received from the Netherlands Organization for Scientific Research (NWO) and the Hungarian Scientific Research Fund (OTKA) (grant no. N31721 & T031723). MERLIN is a National Facility operated by the University of Manchester at Jodrell Bank Observatory on behalf of the UK Particle Physics and Astronomy Research Council (PPARC).

References

Beasley A.J., Conway J.E. 1995, in: Very Long Baseline Interferometry and the VLBA, eds. Zensus J.A., Diamond P.J., Napier P.J., ASP Conference Series 82, San Francisco, 327

Fey A.L., Boboltz D.A., Gaume R.A., Eubanks T.M., Johnston K.J., 2001, AJ 121, 1741

Garrett M.A., Garrington S.T. 1998, in: Radio Emission from Galactic and Extragalactic Compact Sources, Proc. IAU Coll. 164, eds. Zensus J.A., Taylor G.B., Wrobel J.M., ASP Conference Series 144, San Francisco, 145

Garrett M.A., Muxlow T.W.B., Garrington S.T., Alef W., Alberdi A., van Langevelde H.J., Venturi T., Polatidis A.G., et al. 2001, A&A 366, L5

Garrington S.T., Garrett M.A., Polatidis A. 1999, NewAR 43, 629

Garrington S., Muxlow T., Garrett M. 2001, in: Galaxies and Their Constituents at the Highest Angular Resolution, Proc. IAU Symp. 205, eds. Schilizzi R.T., Vogel S., Paresce F., Elvis M., ASP, San Francisco, 102

Gurvits L.I., Kellermann K.I., Frey S. 1999, A&A 342, 378

Stoughton C.,Lupton R.H., Bernardi M., Blanton M.R., Burles S., Castander F.J., Connolly A.J., Eisenstein D.J., et al. 2002, AJ 123, 485

White R.L., Becker R.H., Helfand D.J., Gregg M.D. 1997, ApJ 475, 479

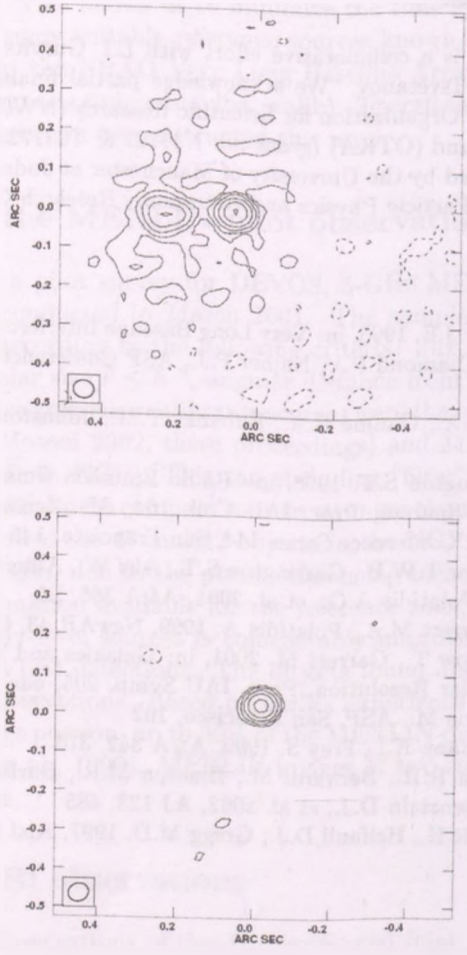

Figure 2: 5-GHz MERLIN images of two radio sources in the DEVOS NGP field. The contours are drawn at -2, 2, 4, 8, 16, 32 and 64 mJy/beam. The source NGP01 (top) is the strongest FIRST source in the field ($S_{1.4} = 478$ mJy). The MERLIN image shows a clearly resolved double structure surrounded by diffuse emission. The peak brightness is 68 mJy/beam. On the other hand, NGP15 (bottom) is compact on these angular scales. The peak brightness is 44 mJy/beam. The restoring beam size (~ 50 mas) is displayed in the bottom-left corner of the images. The phase-referencing technique allows us to refine the astrometric position of the sources. The improvement is indicated by the offset between the image field center and the location of the brightness peak.

Model Galaxy Spectra and Photometric Redshift Estimation

Zsuzsanna Győry
Eötvös Loránd University, Department of Physics of Complex Systems
H-1117 Budapest, Pázmány Péter sétány 1/A, Hungary
E-mail: gyory@complex.elte.hu

Abstract

We study the suitability of the Bruzual-Charlot galaxy isochrone synthesis spectral evolution models for being used as spectral templates for photometric redshift estimation of galaxies. We compare solar metallicity models with 64 composite galaxy spectra created from the Sloan Digital Sky Survey (SDSS) measurements. First results of the photometric redshift estimation using a spectral template library created from the best fitting model spectra are presented.
Keywords: *galaxies: photometry – galaxies: distances and redshifts*

1. Introduction

Measuring the redshift of distant objects is essential for determination of distances on large scales. We can calculate it from the shift of spectral lines using a high resolution spectrum, but spectroscopy is a time-consuming measurement. Photometric measurements are available even for distant and faint objects, for which spectroscopy is very difficult to carry out. While making photometry in five passbands of about 100 million of galaxies, SDSS will record spectra of only $\approx$ 1 million brightest of them.

Fortunately we can estimate the redshift of galaxies from multicolor broad-band photometry. In a photometric observation we sample the redshifted spectrum with broad-band filters. Due to the slowly varying continuum shape the shift of the spectrum can be detected in the photometric observations. If one has a catalog of typical galaxy spectra, one can mimic the whole process in a computer: redshift the template spectrum, pass through the filters and calculate magnitudes. Comparing these simulated magnitudes to the measured ones, one can find the spectral type and redshift that gives the best match (Gwyn & Hartwick, 1996). With this method – the so called photometric redshift estimation – redshift can be determined for distant objects, thus we can obtain information on the stucture of Universe at larger scales than by spectroscopy only.

When the photometric redshift estimation program searches for the best match between the measured and simulated photometry, usually a fine redshift-grid is used, but only few spectral templates, which limits the precision of the redshift estimation. In order to reduce this problem, the present version of the SDSS photo-z code interpolates between template spectra when guessing the spectral type.

We would like to find a more physically motivated approach of templating and create a template library from model galaxy spectra. The idea of using galaxy models for photometric redshift estimation is not new, Koo (1985) used synthetic spectra to trace iso-redshift lines in color-shape diagrams and estimated the redshifts for a hundred of faint galaxies.

Using synthetic spectra generated by the Bruzual & Charlot (2001) isochrone synthesis package we would like to find a set of model spectra optimal for being used as templates in redshift estimation. The finer the type-resolution is, it means, the more spectral templates of different types are used, the more exact estimates one may get. Naturally, the number of used templates is limited by the computational time of the photometric redshift estimation. We have to find a set of models that is not too large but in the same time gives a good enough resolution and covers all physical spectral types.

From this study we can also benefit by identifying the most relevant physical properties of galaxies, such as their age, star formation history and chemical composition.

2. Spectral templates for photometric redshift estimation

2.1. SDSS composite galaxy spectra

To proceed from a small number template set to a better spectral type resolution we created composite spectra from about 20 000 galaxy spectra measured by the SDSS as follows. We devided the 4-dimensional color-space into 64 cells which roughly correspond to galaxies of a common spectral class (even if colors are influenced by redshift as well). In each cell, using the redshift values determined by spectroscopy, we shifted the spectra back to rest-frame, normalized them to a common amplitude and computed the median value at each wavelength. In this way we can hope to get a fair resolution spectral library which covers most of the galaxy spectral types.

However, this composite spectra cannot be used dicertly as templates for redshift estimation, as they do not cover the whole possible wavelength range of the investigated objects due to their redshifts varying in a large range. Since

extrapolation without any extra physical input is not reliable, we would like to combine the benefits of our results obtained from observations and galaxy models describable with several physical parameters.

2.2. Isochrone synthesis spectral evolution

The Bruzual-Charlot model uses isochrones (evolutionary stages at a given time) of an instantaneous-burst stellar populations to calculate spectra of galaxies with given star formation histories (Bruzual & Charlot, 1993). The isochrones of the instantaneous-burst are interpolated from a refined set of stellar evolutionary tracks, so the distribution of stars of various masses and ages evolves smoothly in time. The evolutionary tracks of stars of different masses and metallicities are constructed from measured stellar spectra when available or are supplied by model spectra at some evolutionary stages.

Using these libraries one can compute the evolution of the spectral energy distribution $f_\lambda(t)$ of an instantaneous-burst stellar population. The spectrum $F_\lambda(t)$ of a stellar population with an arbitrary star formation rate (SFR) $\Psi(t)$ can be obtained using the convolution integral

$$F_\lambda(t) = \int_0^t \Psi(t - t')\, f_\lambda(t')\, dt'.$$

As input for the galaxy model, we have the freedom of selecting an initial mass function (IMF) and metallicity, as well as to define an arbitrary star formation rate.

2.3. The models

We preformed our analyses on a simple 2-dimensional subspace of models using stellar polulations with solar metallicity and the Kroupa (2001) universal IMF. We constrained the SFR to a one-parameter exponentially decreasing function of time t, $\Psi(t) \propto e^{-t/\tau}$. A set of synthetic spectra was generated on a 20×20 grid in both galaxy age t and the parameter τ, each ranging from 1 Gyr to 20 Gyr. We selected the synthetic spectra most similar to our SDSS composites by χ^2 minimization.

2.4. Results

As can be seen on Figure 1, even with this simplistic model assumptions we can approxiate our composites representing the typical galaxy spectra well enough. Figure 2 shows the models most preferred by the different main spectral types.

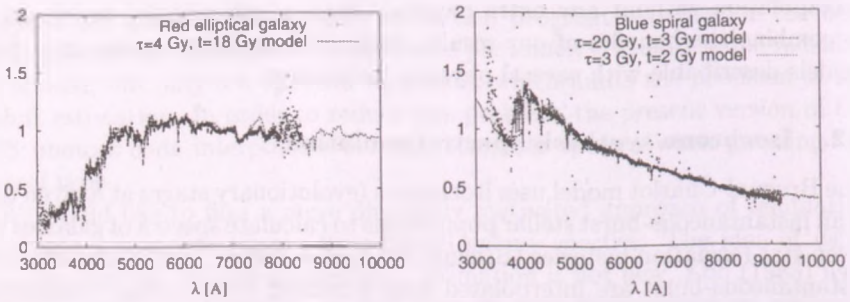

Figure 1: Red elliptical (left) and blue spiral (right) composite spectrum with the best fitting synthetic spectra. Illustration of degeneracy: the two best fitting models on the right panel are practically indistinguishable.

In accordance with our expectations, bluer spiral galaxies are best fitted by models with recent star formation, it means their age is comparable to the characteristic scale τ of star formation. Specrta of red elliptical galaxies do not show features implying presence of young stars, which can be in our exponentially decreasing SFR model achieved by small value of τ compared to the age.

An apparent feature of the model fitting is that blue galaxies are not very sensitive to the value of τ which results degeneracy in χ^2. Sometimes it produces multiple minima which differ only slightly in χ^2 but belong to completely different parameters. Even if it has no influence on the template library we construct, we have to pay attention to this effect when trying to identify the most relevant physical parameter combinations.

Models with age > 15 Gyr clearly cannot be physical and also fits with minimal χ^2 at the border of the parameter region are not reliable. We received this χ^2 minimizing parameters because of our constraints to the model.

The fact that in some cases our composite spectra cannot be fitted by physically reasonable models implies that we have to broaden our models. First of all metallicity should be treated as a free parameter as it has a great impact on color. Models with SFR different from exponential sould be included as well.

However, if we construct a library from the most preferred synthetic spectra and use them as templates for photometric redshift estimation, we can get relatively good agreement with the actual redshift values determined by spectroscopy. Figure 3 shows the photometric redshifts versus the spectroscopic values in the case of two different methods. In the first case, we used a set

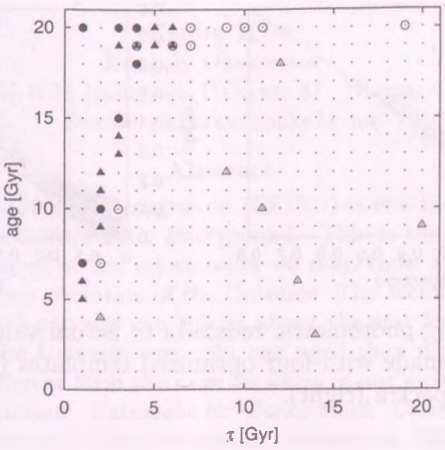

Figure 2: Model parameters best describing our SDSS composites. Galaxy types from bluest to the reddest: open triangle, open circle, solid triangle, solid circle.

of four optimized templates generated by template reconstruction described in Budavári et al. (2000) and Budavári et al. (2001). In the second case we used 40 synthetic spectra most similar to the composites. The better resolution apparently reduces the error of estimation in some redshift ranges but the studied model family is clearly still not sufficiently rich to be an optimal choice for redshift estimation, it also induces systematical deviations due to the insufficient coverage of spectral types.

3. Conclusions

We studied a subset of models generated by the Bruzual-Charlot galaxy isochrone synthesis spectral evolution code. Solar metallicity and exponentially decreasing SFR models most similar to the SDSS composite spectra were identified and implemented in photometric redshift estimation of galaxies. We concluded that our approach can lead to a better precision of redshift estimation if we extend the allowed region of considered models.

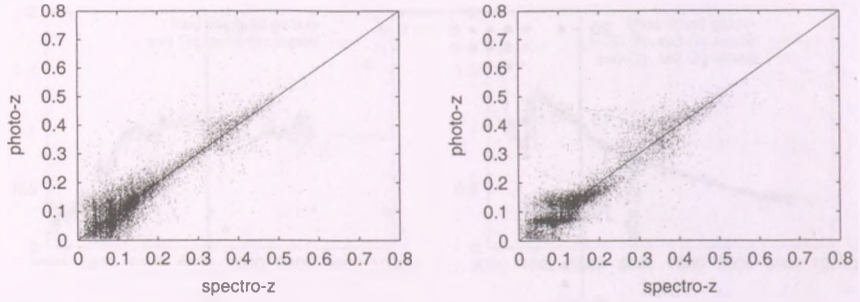

Figure 3: Comparing photometric redshifts to actual values from photometric redshift estimation made with four optimized templates (left) and with the 40 best fitting model spectra (right).

Acknowledgements

I would like to thank I. Csabai and T. Budavári for their help and inspiring discussions and acknowledge the support of the National Scientific Research Fundations (OTKA) grant no. T030836.

References

Bruzual G. & Charlot S., 1993, ApJ, 405, 538
Bruzual, G. & Charlot, S., 2001, http://www.sdss.mpg.de/sdssMPA/Spectral_Tools/
Budavári, T., Szalay, A.S., Conolly, A.J, Csabai, I. & Dickonson, M.E., 2000, AJ, 120, 1588
Budavári, T. et al., 2001, AJ, 122, 1163
Gwyn, S.D.J. & Hartwick, F.D.A., 1996, ApJ, 468, L77
Koo, D.C., 1985, AJ, 90, 148
Kroupa P., 2001, MNRAS, 322, 231

The Cosmic Far-Infrared Background

Csaba Kiss
Konkoly Observatory
H-1525 Budapest, P.O.Box 67., Hungary
E-mail: pkisscs@konkoly.hu

Abstract

The Cosmic Far-Infrared Background (CFIRB) is one the most interesting parts of the Extragalactic Background. This is the spectral range, which contains most of the information we may know about the – cosmologically – recent evolution of the Universe. The accumulated infrared light of unresolved galaxies can tell us about the star formation history at $z \approx 1$, when the Universe was only half aged than now, and galaxies looked pretty different form the ones we know in our vicinity today.
KEYWORDS: *cosmology: Extragalactic Background, Cosmic Far-Infrared Background – infrared: diffuse radiation – instument: ISO, ISOPHOT*

1. Origin of the Cosmic Far-Infrared Background

The Extragalactic Background (EB) is – by definition – an *isotropic* diffuse radiation originating form extragalactic distance. It covers the whole observable electromagnetic spectrum, from radio waves to gamma rays. The EB emission originates from different sources along the electromagnetic spectrum. At certain wavelenghts we look back to ages when there were still no indiviual objects, and the light what we can measure today is a fingerprint of the radiation field at that time (e.g. the Cosmic Microwave Background). In other bands we can observ the accumulated light of unresolved individual objects (typically galaxies), which are much too faint to be detected alone, as in the case of the CFIRB. In Fig. 1. we present the spectral components of the EB.

The spectral range of the CFIRB starts from $\sim 60\,\mu$m and last at $\sim 300\,\mu$m, where the CMB starts to be the dominant EB component. The major source of the FIR emission is the quasitermal emission of cold dust particles. The dust – despite its relatively low fraction in mass – plays a crucial role in the energy balance and radiation properties of the interstellar matter. It can absorb photons from the UV and visual range emitting energy back in the (far-)infrared. Although only one-third on the bolometric luminosity of local galaxies is radiated in the infrared, there is a growing evidence, that this fraction is actually increasing with redshift (Soifer & Neugebauer, 1991). On the other hand, significant amount of near- and mid-infrared light is shifted to the far-infrared at

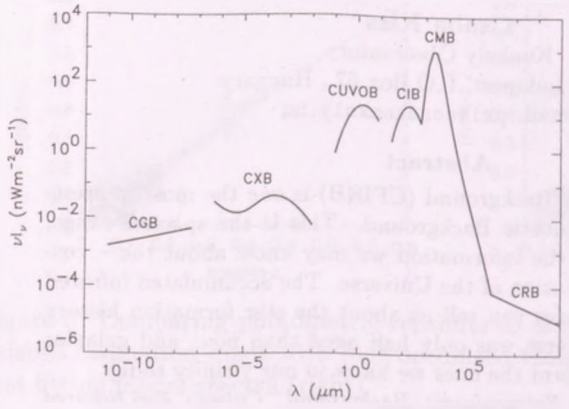

Figure 1: Spectral components of the Extragalactic Background (Hauser & Dwek 2001); CGB: Cosmic Gamma Background, CXB: Cosmic X-ray Background, CUVOB: Cosmic Ultra-Violet- and Optical Background, CIB: Cosmic Infrared Background, CMB: Cosmic Microwave Background, CRB: Cosmic Radio Background

higher redshifts. Current data suggest that the global star-formation rate of the Universe peaked at a redshift of $z \approx 1$, then subsequently declined (Lilly et al., 1996), leading to claims, that the bulk of the star formation in the Universe has been seen. Recent data from FIR-studying satellites (IRAS and ISO) indicates, that most of the star-formation may be hidden by dust. However we do not know yet how much star formation is completely hidden, recent results indicate a presence of a population of so called Ultra Luminous Infrared Galaxies (ULIRGs), which were discovered by IRAS (Sanders & Mirabell, 1996). These galaxies are very bright in the infrared, but are very faint in optical, indicating hidden star formation. Models assuming strong galaxy evolution indicated $\sim$5 times higher intensity in the FIR than no-evolution model predictions, obtained by a simple extrapolation of the FIR luminosities of local galaxies. This level is comparable to that of the 'cosmic optical background', estimated by summing the faint galaxy counts down to the deepest limit so far available, which is given by the Hubble Deep Field (Williams et al., 1996). The idea of strong galaxy evolution was recently confirmed by the infrared surveys of ISO (Abergel et al., 1999; Lagache et al. , 1998; Dole et al., 2001).

2. Foreground components of the CFIRB

Detecting the CFIRB is both technically and astrophysically very challenging. Technical difficulties come from the fact, that everything on the surface of the Earth radiates at wavelenths one has to observ the CFIRB at, due to the typical temperatures of $<$300 K. The other major source of the thermal FIR noise

is the telecope itself. Therefore in recent years telescopes observing at FIR wavelengths were spaceborn and cyrogenically cooled to ~4 K (IRAS and ISO). Another techincal deal was the straylight from very bright celestial bodies, like Earth, Moon, Sun, and the brightes planets Jupiter and Saturn.

Even in the case of a perfect observing tool, one has to deal with the astrophysical foreground components (shown in Fig. 2.) of the CFIRB which contribute to the measured emission: the zodiacal light, the galactic cirrus, the intergalactic dust, and – at very long FIR wavelenghts – the Cosmic Microwave Background. There are two major characteristics of the CFIRB to observ: the

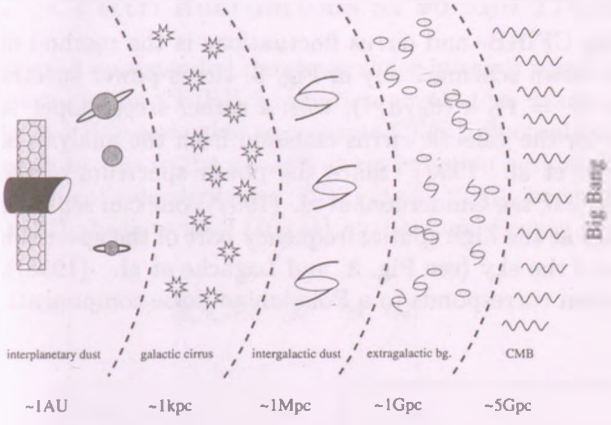

Figure 2: Foreground contaminators of the Cosmic Far-InfraRed Background

absolute level, and the relative strength of its fluctuation amplitude (Hauser & Dwek, 2001). The relative contribution of the foreground components depends on the wavelength and is different in the case of absolute level and fluctuation amplitude measurements.

The emission originated from the intergalactic dust is most probably negligible, as indicated by the measurement performed through the Coma galaxy cluster (Stickel et al., 1998). These measurements provided an excess emission from the intergalactic dust of $\Delta I \approx 0.03\,\mathrm{MJysr}^{-1}$, therefore this component is certainly weaker than $0.1\,\mathrm{MJysr}^{-1}$ for the Local Group.

The contribution of the zodiacal light emission at FIR wavelengths can be extrapolated from the shorter wavelength emission values, using the COBE/DIRBE zodiacal light model (Héraudeau et al., 2001). The zodiacal light emission is smooth on arcminute scales as shown by Ábrahám et al. (1997), therefore does not contribute to the fluctuation amplitude.

The galactic cirrus emission (Low et al., 1984) is originated from the irregulary shaped interstellar clouds of the Galaxy and dominates the far-infrared sky at higher galactic latitudes. This is the dominant foreground component of the CFIRB and also the most difficulte to separate, since this emission changes significantly from place to place in an unpredictable way, leading to a strong *confusion noise* (see e.g. Kiss et al. (2001)), which sets a final limit on the detectability of faint point-sources.

3. Separation of CFIRB- and galactic cirrus emission

The usual way of separating CFIRB- and cirrus fluctuations is the method of Fourier power spectra. As shown schematically in Fig. 3. cirrus power spectra has a power-law behaviour ($P = P_0 \times (d_0/d)^{\alpha}$), with a rather steep slope. A general $\alpha \approx -3$ was derived for the galactic cirrus emission from the analysis of 100 μm IRAS scans (Gautier et al., 1992). Since the power spectrum of the CFIRB is much shallower ($\alpha \approx 0$, see Guiderdoni et al. (1997)) one can separate these from cirrus fluctuations at the high spatial frequency part of the spectrum at the best cirrus windows of the sky (see Fig. 3. and Lagache et al. (1998)). The $\alpha \approx 0$ spectral distribution corresponds to a Poissionian noise component.

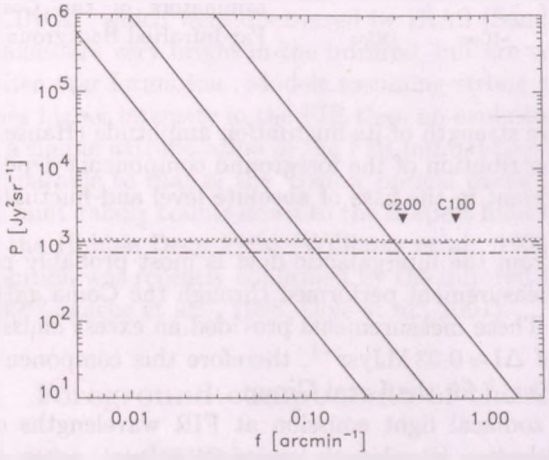

Figure 3: Model power spectra of the galactic cirrus emission and CFIRB fluctuations (Guiderdoni et al., 1997). Horizontal lines correspond to different CFIRB models, while steep linears represent cirrus power spectra of different strength. The resolution limits of the ISOPHOT C100 and C200 detectors are also marked.

Based on the results by Gautier et al. (1992) Helou & Beichman (1990) developed a formula for estimating the cirrus confusion noise in the far-infrared:

$$(N_{H\&B}/1\,mJy) = 0.3 \times (\lambda/100\,\mu m)^{2.5} (D_t/1\,m)^{-2.5} \times (\langle B_\lambda \rangle / 1\,MJysr^{-1})^{1.5}$$

where λ is the measurement wavelength, D_t is the diameter of the telescope primary mirror and $\langle B_\lambda \rangle$ is the average surface brightness of the field. Since the surface brightness of the CFIRB is constant (and so do the fluctuation amplitude), one should observ a deviation of the measure of the confusion noise from the Helou & Beichman (1990) formula at low surface brightness fields (Kiss et al., 2001). The amount of this deviation is closely related to the CFIRB fluctuation amplitude at this wavelength. This surface brightness dependence provides a new method to separate the CFIRB fluctuations from that of galactic cirrus.

4. CFIRB fluctuations at 90 and 170μm

We used an extended database of far-infrared maps observed by ISOPHOT to determine the CFIRB fluctuation amplitudes using the brightness-dependence method. We were able to separate CFIRB fluctuation ($\delta B_0(\lambda)$) from the confusion noise due to the galactic cirrus emission both at 90 and 170 μm. With some theoretical considerations (Bond et al., 1986), we were also able to estimate the CFIRB absolute level ($B_0(\lambda)$) at these wavelength (see Fig. 4.).

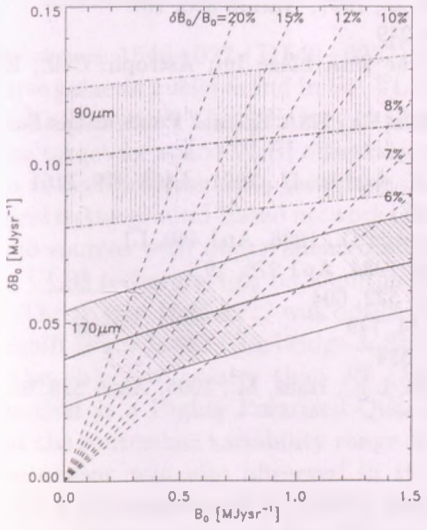

Figure 4: CFIRB fluctuation amplitudes versus the CFIRB absolute level assumed. The hatched regions represent the formal errors of the fits for 90 and 170 μm. A set of dashed lines marks $\delta B_0/B_0$ = 6, 7, 8, 10, 12, 15 and 20%.

At 170 μm $\delta B_0/B_0 = 7\%$ provides a CFIRB absolute level of $B_0 = 0.8 \pm 0.2\,\mathrm{MJysr^{-1}}$. At 90 μm the dependence of δB_0 on B_0 is even weaker than at 170 μm, therefore a well defined value of $0.11 \pm 0.03\,\mathrm{MJysr^{-1}}$ can

be determined. The B_0 value of $1.1 \pm 0.3\,\mathrm{MJysr^{-1}}$, is the same as the average surface brightness of the faintest $90\,\mu\mathrm{m}$ maps in our data set. The expected cirrus contribution in these fields – predicted from the $\sim 0.8\,\mathrm{MJysr^{-1}}$ value at $170\,\mu\mathrm{m}$ by using a typical cirrus spectrum (modified black-body SED, ν^2 emissivity law, 20 K temperature) – is about $0.3\,\mathrm{MJysr^{-1}}$. This result suggests that the $1.1\,\mathrm{MJysr^{-1}}$ is an upper limit and the most likely value of the CFIRB lies at the lower end of the uncertainty range, i.e. $\sim 0.8\,\mathrm{MJysr^{-1}}$. Our results are in very good agreement with theoretical calculations (Pei et al., 1999) and with results obtained by other methods (e.g. Lagache et al. (1998)). A more detailed description of our work is presented in our recent paper (Kiss et al., 2001)

References

Abergel, A., André, P., Backmann, A., et al., 1999, ESASP 427, 615
Ábrahám P., Leinert Ch., Lemke D., 1997, A&A 328, 702
Bond, J.R., Carr B.J., Hogan, C.J., 1986, ApJ 428, 306
Dole, H., Gispert, R., Lagache, G., et al., 2001, A&A 372, 364
Gautier III T.N., Boulanger F., Pérault M., Puget J.L., 1992, AJ 103, 1313
Guiderdoni B., Bouchet F.R., Puget J.L., et al., 1997, Nature 390, 257
Hauser, M.G., Dwek, E., 2001, ARA&A 39, 249
Helou G., Beichman C.A., 1990, Proc. of the 29th Liège Int. Astroph. Coll., ESA Publ., p. 117.
Héraudeau, Ph., Ábrahám, P., Klaas U., Kiss Cs., ESA Special Publications Series, Vol. 481., in press
Kiss, Cs., Ábrahám, P., Klaas, U., Juvela, M., Lemke, D., 2001, A&A 379, 1161
Lagache, G., Puget, J.-L., 2000, A&A 355, 17
Lilly, S.J., Le Fèvre, O., Hammer, F., Crampton D., 1996, ApJ 460, L1
Low F., Beintema D.A., Gautier T.N., et al., 1984, ApJ 278, 19
Pei Y.C., Fall M.S., Hauser M.G., 1999, ApJ 522, 604
Sanders, D.B., Mirabell, I.F., 1996, ARAA 34, 749
Soifer, B.T., Neugebauer, G., 1991, AJ 101, 354
Stickel, M., Lemke, D., Mattila, K., Haikalaa, L.K., Haas, M., 1998, A&A 329, 55
Williams, R.E., et al., 1996, AJ 112, 1335

1546+027: HIGH RESOLUTION RADIO STRUCTURE OF A COMPACT QUASAR

László Mosoni
FÖMI Satellite Geodetic Observatory
H-1373 Budapest, P.O. Box 546, Hungary
E-mail: mosoni@sgo.fomi.hu

Abstract

A 5-GHz space VLBI image of a very compact quasar 1546+027 is presented with an unprecedented angular resolution at this observing frequency. The source has been observed in a broad spectral region (radio, optical, X-ray, γ-ray) in the recent years. Our image shows changes in the source structure compared with earlier observations. These changes can also be seen at other radio frequencies. The source is a candidate for detecting apparent superluminal motion. We estimate the value of the rest-frame brightness temperature of the source, $T_B = 0.46 \times 10^{12}$ K.
KEYWORDS: *techniques: interferometric – galaxies: active – quasars: individual: 1546+027*

1. Introduction

The source 1546+027 (J1549+0237) is one of the brightest and most compact active galactic nuclei found in the VLBI Space Observatory Programme (VSOP) 5-GHz Prelaunch VLBA Survey in 1996 (Fomalont et al., 2000), therefore it is an ideal target for space VLBI observations. Space VLBI (Hirabayashi et al., 1998) is a radio interferometric technique involving an orbiting radio antenna that is linked to the ground-based network of radio telescopes in order to image compact radio sources with unprecedented angular resolution. A detailed description of the VLBI technique can be found in Zensus et al. (1995).

The source 1546+027 was optically identified by Bolton & Wall (1970). Its redshift is $z = 0.412$ (Burbridge & Strittmatter, 1972). The optical polarization of the object is greater than 3% (Moore & Stockman, 1981), therefore it is classified as a Highly Polarized Quasar (HPQ). Optical monitoring has shown that the source has variability range of almost 1 magnitude (Smith et al., 1994). The quasar was also observed in the high energy regime, in the X-rays by ROSAT (Brinkmann et al., 1995), and in the γ-rays by the EGRET instrument on the Compton Gamma Ray Observatory (Fichtel et al., 1994).

The source was often observed at different radio frequencies. There are

multi-frequency and monitoring data available. Using these data, changes can be tracked in the flux density and spectral index values. Until 1996, the source seemed to be unvariable at 327 MHz (Ghosh et al., 1994), at 22 and 37 GHz (Wiren et al., 1992), and in a multi-frequency radio survey covering the frequency range of 1.5–10.6 GHz (Neumann et al., 1994). At the beginning of 1996, Australia Telescope Compact Array monitoring (1996–1998, S. Tingay et al., in preparation) and other data indicate a prominent flux density outburst (Fig. 1).

The source can be found in some of the imaging radio surveys, for example the 1.64-GHz VLA survey (Murphy et al., 1993), the 5-GHz VLBA Prelaunch Survey (Fomalont et al., 2000), the 5-GHz VSOP Survey (Hirabayashi et al., 2000) and the Radio Optical Reference Frame image database (Fey & Charlot, 1997) at 2.3 and 8.4 GHz.

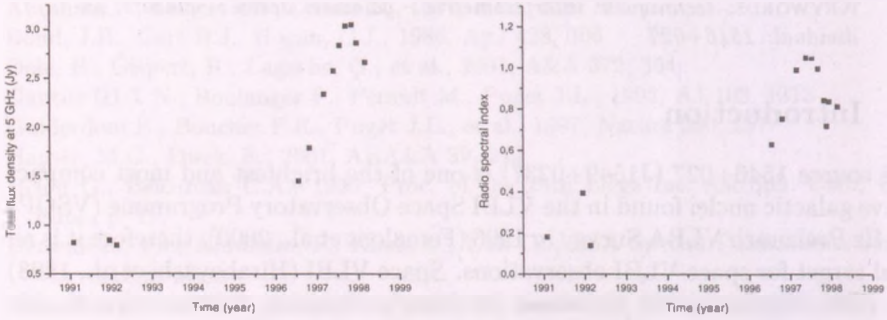

Figure 1: The 5-GHz total flux density (S, left) and the calculated radio spectral index (α, right) as a function of time. The spectral index is defined as $S \sim \nu^{\alpha}$, where ν is the frequency. The flux density data are taken from S. Tingay et al. (in preparation), Kovalev et al. (1999) and Neumann et al. (1994). Both curves indicate an outburst around 1995.

2. Observations, calibration and data reduction

The observations took place on 13 August 2000, with four antennas of the European VLBI Network (EVN), Effelsberg, Hartebeesthoek, Torun and Noto, and the HALCA satellite (Hirabayashi et al., 1998) at 5 GHz. The source was

Table 1: Fitted Gaussian model components of 1546+027.

Component	a	b	c
Flux density [Jy]	0.688	0.280	0.082
Radius [mas]	0.05	0.81	1.51
Position angle [°]	-22	179	179
Major axis [mas]	0.56	0.52	0.30
Minor axis [mas]	0.18	0.15	0
Major axis position angle [°]	-11	-27	-48

observed over 7 hours in left circular polarization. The data were recorded with 32 MHz bandwidth. The correlation took place at the NRAO correlator in Socorro (NM, USA).

Initial data calibration and fringe-fitting were done using the NRAO AIPS package (Cotton, 1995; Diamond, 1995). The Caltech DIFMAP package (Shepherd et al., 1994) was used for self-calibration, imaging and determining a brightness distribution model of the source.

3. Results and discussion

At the time of our observations, the total flux density of the source was decreasing, years after the 3-Jy maximum at 5 GHz (Fig. 1). Our space VLBI image of 1546+027 at 5 GHz is displayed in Fig. 2.2.. It shows a core-jet structure in N-S direction similar to other VLBI images with lower resolution. We fitted a brightness distribution model to the source visibility data. The model consists of three elliptical Gaussian components: the core (**a**), and two jet components (**b** and **c**) within 1.5 mas to the South of the core (Table 1).

Using the fitted model components, we can estimate the rest-frame brightness temperature of the core as

$$T_{\mathrm{B}}[\mathrm{K}] = 1.22 \times 10^{12} \frac{S}{\theta_{\mathrm{maj}} \theta_{\mathrm{min}}} \frac{1+z}{\nu^2},$$

where S is the component's flux density in Jy, θ_{maj} and θ_{min} are the major and minor axis of the component in mas, respectively (assuming optically thick

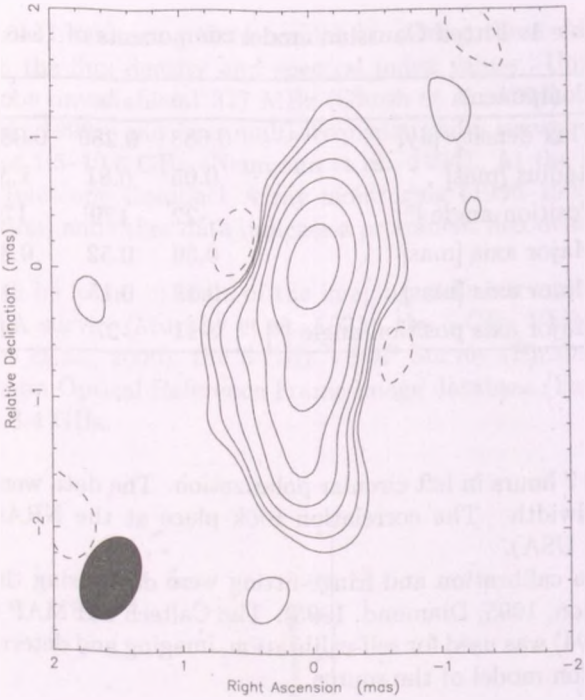

Figure 2: Clean image of the source 1546+027 with a clear N-S core-jet structure. The contours are drawn at -1, 1, 2, 4, 8, 16, 32 and 64% of the 0.535 Jy/beam peak brightness. The total flux density is 1.1 Jy. The restoring beam is shown in the bottom-left corner.

Gaussian brightness distribution), ν is the observing frequency (in GHz) and z is the redshift. We obtain $T_{\rm B} = 0.46 \times 10^{12}$K for the core brightness temeprature. This value is close to the inverse Compton limit, in agreement with independent estimates of $T_{\rm B}$ based on earlier data.

The linear core-jet distance between components **a** and **b** (Table 1) is $2.8/h$ pc (where h is the dimensionless Hubble constant; the Einstein–de Sitter cosmological model is assumed, $q_0 = 0.5$). According to the total flux density monitoring data (Fig. 1), an outburst has occured at about the end of 1995. If we associate component **b** with this outburst, then this change in the linear core-jet separation implies an apparent speed of $2c/h$ (c is the speed of light). This can be considered as a marginal evidence for a moderately superluminal

motion that could be verified with future high resolution VLBI observations.

In the arcminute resolution VLA image (Murphy et al., 1993), the orientation of the core-jet structure is different from what we see on VLBI scales. The misalignment angle between the kpc- and the pc-scale jet is nearly 35°. The object was observed with MERLIN as a phase-reference calibrator source (Frey & Mosoni 2002, these proceedings) in March 2001. The $\sim$ 50 mas resolution MERLIN image (Fig. 3) shows that the jet direction continues to the South, on intermediate scales between our sub-mas resolution space VLBI image (Fig. 2.2.) and the arcminute resolution VLA image.

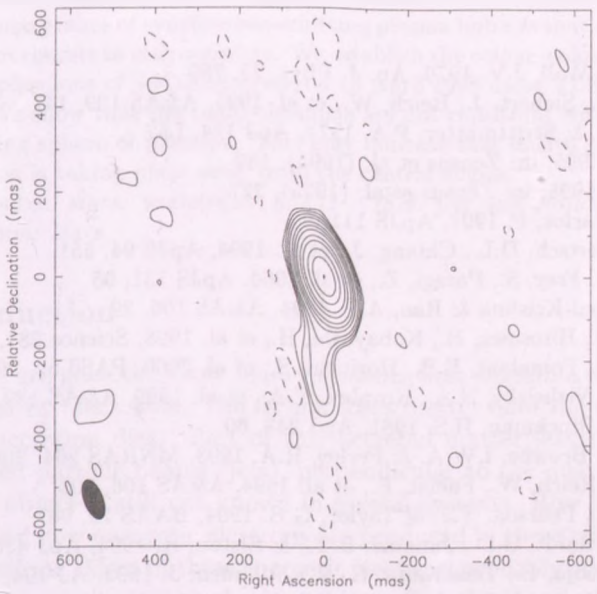

Figure 3: 5-GHz MERLIN image of 1546+027. The contours are drawn at −0.025, 0.025, 0.05, 0.1, 0.2, 0.5, 1, 2, 5, 10, 25, 50 and 99% of the 1.29 Jy/beam peak brightness. The restoring beam is shown in the bottom-left corner.

Acknowledgements

We gratefully acknowledge the VSOP Project, which is led by the Japanese Institute of Space and Astronautical Science in cooperation with many organizations and radio telescopes around the world. MERLIN is a National Facility operated by the University

of Manchester at Jodrell Bank Observatory on behalf of the UK Particle Physics and Astronomy Research Council (PPARC). This work has been done in collaboration with P.G. Edwards, I. Fejes, E.B. Fomalont, S. Frey, M.A. Garrett, S.T. Garrington, L.I. Gurvits, Z. Paragi, W.K. Scott and Z.I. Tsvetanov. We acknowledge partial financial support received from the Netherlands Organization for Scientific Research (NWO) and the Hungarian Scientific Research Fund (OTKA) (grant no. N31721 & T031723). This work was supported by the European Community under its Access to Research Infrastructure action of the Improving Human Potential Programme (contract no. HPRI-CT-1999-00045).

References

Bolton, J.G. & Wall, J.V. 1970, Au. J. Phys. 23, 789
Brinkmann, W., Siebert, J., Reich, W., et al. 1995, A&AS 109, 147
Burbidge, E.M. & Strittmatter, P.A. 1972, ApJ 174, L57
Cotton, W.D. 1995, in: Zensus et al. (1995), 189
Diamond, P.J. 1995, in: Zensus et al. (1995), 227
Fey, A.L. & Charlot, P. 1997, ApJS 111, 95
Fichtel, C.E.,Bertsch, D.L., Chiang, J., et al. 1994, ApJS 94, 551
Fomalont, E.B., Frey, S., Paragi, Z., et al. 2000, ApJS 131, 95
Ghosh, T., Gopal-Krishna & Rao, A.P. 1994, A&AS 106, 29
Hirabayashi, H., Hirosawa, H., Kobayashi, H., et al. 1998, Science 281, 1825
Hirabayashi, H., Fomalont, E.B., Horiuchi, S., et al. 2000, PASJ 52, 997
Kovalev, Y.Y., Nizhelsky, N.A., Kovalev, Y.A., et al. 1999, A&AS 139, 545
Moore, R.L. & Stockman, H.S. 1981, ApJ 243, 60
Murphy, D.W., Browne, I.W.A. & Perley, R.A. 1993, MNRAS 264, 298
Neumann, M., Reich, W., Fuerst, E., et al. 1994, A&AS 106, 303
Shepherd, M.C., Pearson, T.J. & Taylor, G.B. 1994, BAAS 26, 987
Smith, P.S., Schmidt, G.D., Jannuzi, B.T., & Elston, R. 1994, ApJ 426, 535
Wiren, S., Valtaoja, E., Terasranta, H. & Kotilainen, J. 1992, AJ 104, 1009
Zensus, J.A., Diamond, P.J. & Napier, P.J. (eds.) 1995, Very Long Baseline Interferometry and the VLBA, ASP Conference Series 82, ASP, San Francisco

The radio colour–colour diagram of Van der Laan Bubbles — an application to SS433

Zsolt Paragi*
Joint Institute for VLBI in Europe / FÖMI Satellite Geodetic Observatory
Postbus 2, 7990 AA Dwingeloo, The Netherlands
E-mail: paragi@jive.nl

Abstract

A radio "colour–colour" diagram is defined in order to determine the evolutionary state of synchrotron-emitting plasma bubbles that are ejected during outbursts in microquasars. We establish the colour–colour diagram for the plasmons of SS433 observed on 18 April 1998 using VLBI observations. We show that the radio plasmons are not consistent with a simple expanding sphere of plasmon. This may indicate that in-situ particle acceleration is taking place away from the central engine.
KEYWORDS: *stars: individual: SS433 – ISM: jets and outflows – radio continuum: stars*

1. Introduction

Microquasars are galactic X-ray binary systems that contain a normal star and a neutron star or black hole. The former loses matter onto the compact object through an accretion disk. Part of this accreted matter leaves the system in well collimated particle beams (jets), perpendicular to the disk. The nature of the compact object is still not known in several systems. How jets are formed, collimated, and how energetic electrons are produced in these relativistic beams are open questions. Most of these energetic electrons probably originate from the vicinity of the central engines of microquasars, but the Fermi-process (electron acceleration in shocks) within the jets may also play a role. Jet processes are briefly summarized by Spencer (1998).

An introduction to the Galactic radio-jet system SS433 as a microquasar and its high resolution properties determined in recent VLBI observations is

*This work has been carried out in collaboration with I. Fejes, R.C. Vermeulen, R.T. Schilizzi, R.E. Spencer and A.M. Stirling. Special thanks to Al Stirling for useful suggestions, István Fejes and Sándor Frey for careful reading. Financial support is acknowledged from the Hungarian Space Office (MŰI), the Netherlands Organization for Scientific Research (NWO) and the Hungarian Scientific Research Fund (OTKA, grant no. N31721 & T031723).

given in Paragi (2001). The particular VLBI experiment shown here and the data analysis are described in Paragi (2000).

Below we introduce the Van der Laan (1966) model (originally developed for quasars) that describes radio emission from spherical plasmons ejected from the central engine during an outburst. The spectral index evolution of these ejecta from the optically thick to the optically thin regime is demostrated on a radio colour-colour diagram. A spectral analysis of the radio components observed in SS433 follows.

2. Radio emission from spherically symmetric ejecta

Radiative properties of spherically symmetric ejecta depend on their instantaneous apparent size (θ), the number density of relativistic electrons (N), and the strength of the magnetic field (H). The energy distribution of synchrotron radiating particles is $N(E) = KE^{-s}$, where s is the energy spectral index. The emission and absorption coefficients of the synchrotron process have the following dependence on frequency: $j_\nu \propto \nu^{(1-s)/2}$ and $\kappa_\nu \propto \nu^{-(4+s)/2}$, respectively. The resulting spectrum is $S \propto \nu^\alpha$, α is the spectral index. In the optically thin domain the emission coefficient determines the spectrum, and $\alpha = (1-s)/2$. In the optically thick domain the spectrum depends on the source function (j_ν/κ_ν), resulting in $\alpha = 2.5$.

The time evolution of the received flux density (S) in a radio outburst as observed at different frequencies was calculated by Van der Laan (1966). The effect of the optical depth (τ) changing through different lines of sights in the source was considered by Hjellming & Johnston (1988). Their basic assumptions were that the ejected cloud of plasma expands adiabatically into the surrounding medium, and relativistic electrons are genarated within a short time range close to the central engine, and not somewhere in the extended the jet. This latter assumption seems to be valid for microquasars (Spencer, 1998).

The time evolution of the flux density at four different frequencies is shown in Fig. 1. The plasmon brightens in the optically thick stage (until $\tau \sim 1$) with increasing radius ($\theta \propto t$ for free expansion), and there is an exponential cutoff in the optically thin regime. Of course τ has a strong frequency dependence, this is why the radio lightcurves peak at different times.

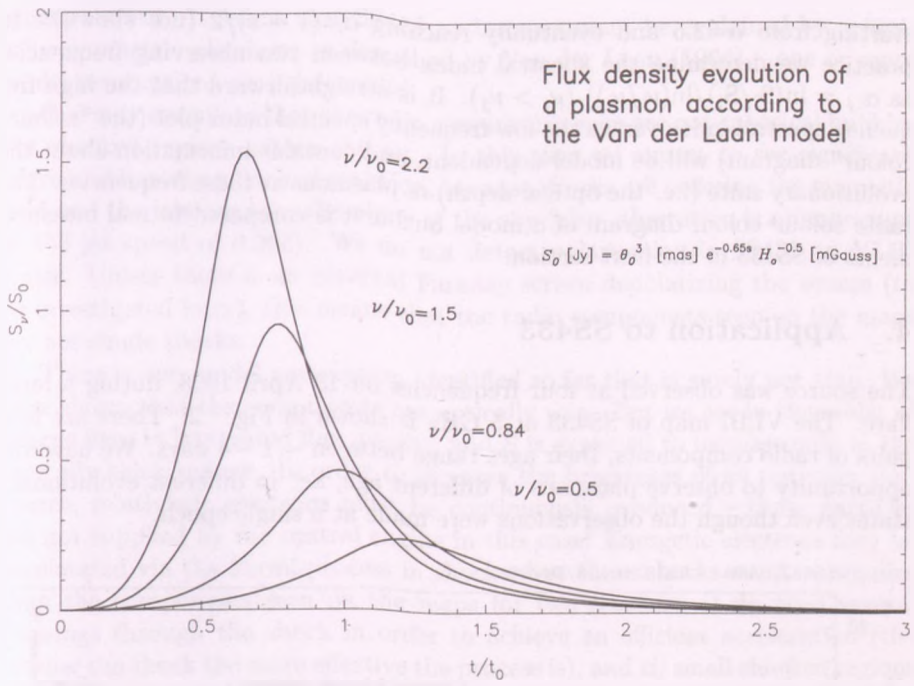

Figure 1: Flux density evolution of plasmons (Van der Laan, 1966; Hjellming & Johnston, 1988). Observing frequencies available in VLBI were selected (ν_0 =10 GHz, ν =22, 15, 8.4, 5 GHz)

3. The radio colour-colour diagram

The model outlined above might be checked in multi-frequency observations by monitoring the total flux density of the sources during outburst. However, there may be several radio components contributing to the total flux, therefore it is desirable to have high resolution imaging experiments using the Very Long Baseline Interferometry Technique (Zensus et al., 1995). VLBI observations are useful also because we can measure the size of the ejected plasmons, and this allows us to estimate the magnetic field strength. Even more information could be gathered if we could determine the optical depth of the component directly. In order to achieve this, we define a radio "colour–colour" diagram.

Similarly to Fig. 1, one might plot the spectral index evolution with time,

starting from α=2.5 and eventually reaching α=$(1 - s)/2$ (not shown). In practice we determine the spectral index between two observing frequencies as $\alpha_{ij} = \ln(S_i/S_j)/\ln(\nu_i/\nu_j))$ $(\nu_i > \nu_j)$. It is straightforward that the high frequency spectral index versus the low frequency spectral index plot (the "colour–colour" diagram) will be model dependent, and contains information about the evolutionary state (i.e. the optical depth) of plasmons at these frequencies. The radio colour–colour diagram of a model outburst is compared to real measurements of SS433 in the next section.

4. Application to SS433

The source was observed at four frequencies on 18 April 1998, during a large flare. The VLBI map of SS433 at 5 GHz is shown in Fig. 2. There are four pairs of radio components, their ages range between $\sim 1 - 4$ days. We have the opportunity to observe plasmons of different age, i.e. in different evolutionary states even though the observations were made at a single epoch.

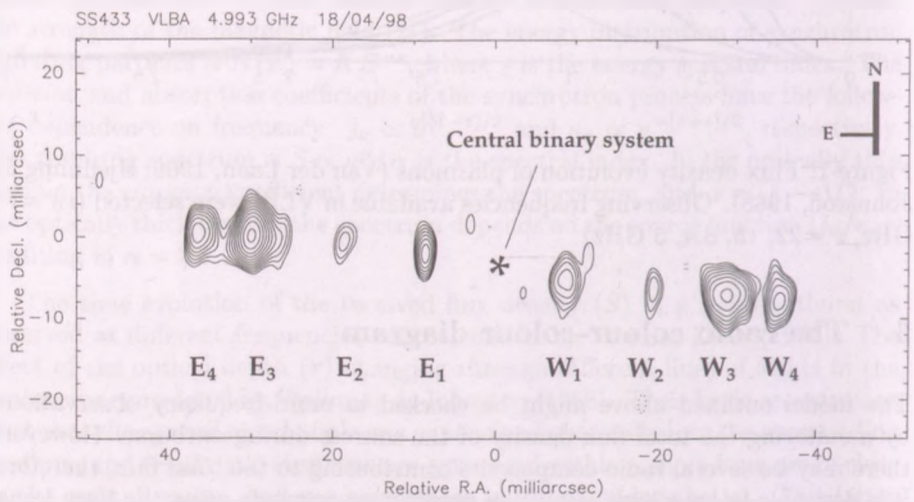

Figure 2: The plasmons of SS433 during a flare on 18 April 1998

It can be seen from the radio colour–colour diagram (Fig. 3) that the plasmons of SS433 are already in the optically thin regime at these frequencies. Even the youngest component has $\tau_{10} \sim 0.1$. Other components have spectral indices that are not compatible with the model (W_1 is located outside the

ranges shown). It seems that SS433 outbursts cannot be explained by spherically symmetric plasmons as described by Van der Laan (1966) – one or more model assumptions must be invalid.

One may speculate that the radio components seen are not spherical bubbles but shocked regions within the jet. In this case we expect to see significant degrees of linearly polarized emission, because shocks are ordering the magnetic field and the jets are near the plane of the sky (also, aberration is unimportant at the jet speed of 0.26c). We do not detect polarization in SS433 on VLBI scales. Unless there is an external Faraday screen depolarizing the source (to be investigated later), this means that the radio components seen on the maps are not single shocks.

There is one model assumption identified so far that is surely not true. We have shown that the components are optically thin. But we are in the midst of a large flare in integrated flux density, and S is expected to increase only in the optically thick regime. In order to increase the brightness of an optically thin source, relativistic electrons must be continuously produced – these particles are not supplied by the central engine in this case! Energetic electrons may be accelerated via the Fermi-process in shocks, but these shocks must be smaller than the components seen on the maps for two reasons: *i)* we need several crossings through the shock in order to achieve an efficient acceleration (the smaller the shock the more effective the process is), and *ii)* small shocked regions with different orientations of H may cancel out the net polarization, resulting in a depolarized source as we observe.

5. Conclusions

We define a radio colour–colour diagram and demonstrate its applicability in analysing radio flares by comparing a model with the observations. There must be ongoing production of relativistic particles in order to explain the optically thin nature of the components and at the same time the increasing brightness of the source. This is clear evidence that in microquasars the central engine is not the only place where electrons can be accelerated to relativistic energies.

References

Hjellming R.M., Johnston K.J., 1988, ApJ 328, 600

Paragi Z. 2000, Ph.D. Dissertation, Loránd Eötvös Univ., Budapest

Paragi Z. 2001, in: E. Forgács-Dajka and Zs. Sándor (eds.) National Postgrad. Reunion in Astron. Astrophys., Loránd Eötvös Univ. and Konkoly Obs., Budapest, p. 53

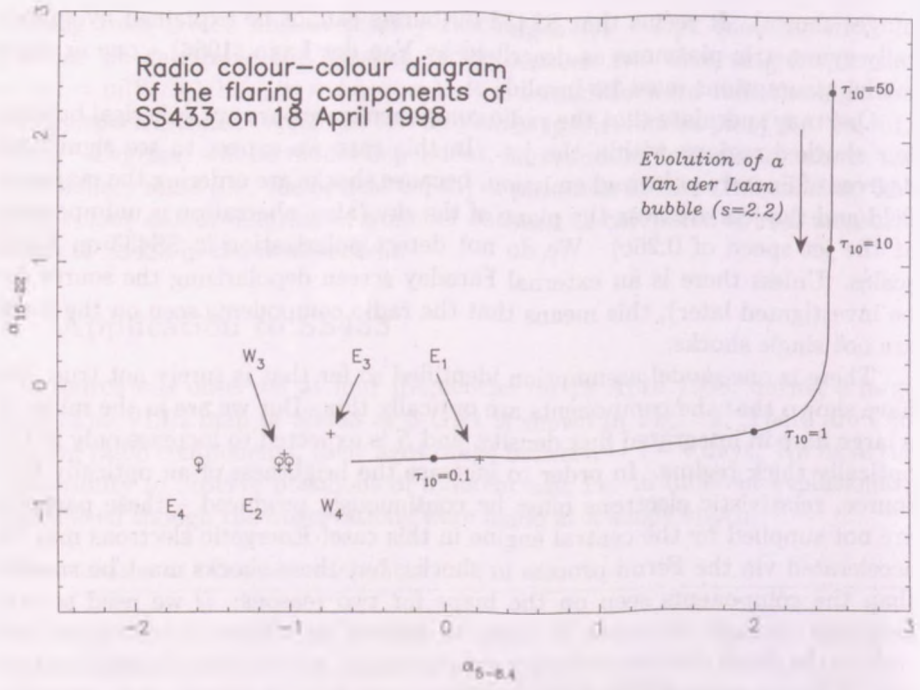

Figure 3: The SS433 radio components compared to the spherical plasmon model (solid curve). There are upper limits for α_{15-22} of some of the components that were not detected at the highest frequencies, W_2 was too faint even at 8 GHz, and W_1 lies out the ranges shown. The energy spectral index used in the model is $s = 2.2$

Spencer R.E., 1998, New Astron. Rev. 42, 653
Van der Laan H., 1966, Nature 211, 1131
Zensus J.A., Diamond P.J., Napier P.J. (eds.) Very Long Baseline Interferometry and the VLBA, ASP Cenference Series 82, 1995

Interstellar Matter

Cs. Kiss
Z. Kiss
V. Könyves
A. Moór
L.V. Tóth

Cold cloud cores in the Cepheus Flare region

Zoltán Kiss[1], L. Viktor Tóth[1,2]
[1] Eötvös Loránd University, Department of Astronomy
H-1518 Budapest, P.O.Box 32., Hungary
[2] Max Planck Institut für Astronomie
Königstuhl 17, 69117 Heidelberg, Germany
E-mail:[1]kissz@astro.elte.hu

Abstract

We study the physical parameters of the interstellar medium in the Cepheus Flare region. We investigated the large scale dust temperature and density distribution based on COBE DIRBE, IRAS and ISOSS data. We give optical B band extinction maps of 61 opaque objects in the $\approx$ 220 square-degree region. We have selected 41 starless, dense cloud cores among these, based on infrared and optical images. As much as 21 cores showed very low ($T < 15K$) FIR colour temperatures. These are considered as candidate pre-protpstellar cores and will be further investigated. [1]

KEYWORDS: *interstellar dust, low mass star formation, Cepheus Flare*

1. Introduction

As recently reviewed by Ward-Thompson (D. Ward-Thompson, 2002, Science, 295, 76.) there are several debates describing the phisical processes and the initial conditions for early phases of interstellar cloud collapse. We intend to gather and analyse multiwavelength data on nearby low mass star forming regions focusing on the phases when no embedded young stellar object (YSO) is seen. Low mass star formation is expected in low and moderate mass (from ten to few hundred solar masses) clouds, in dense ($n(\mathrm{H_2}) > 10^3\mathrm{cm}^{-3}$) and cold ($T \approx 10\mathrm{K}$) cloud cores. As a first step we identify such objects without YSOs in the Ceheus Flare region which is a well known scene of low mass star formation (see eg. M. Kun, ApJS, 1998).

These dense cloud cores are optically thick for the visible light and can be identified as obscuring spots on optical images when they are nearby (up to few hundred pc). On the other hand they are optically thin for their own quasithermal emission, which has a spectral maximum in the very far infrared

[1]This research is part of our observational study of the initial conditions of low mass star formation in the vicinity of Solar System.

(100 to 200μm) The FIR radiation can effectively cool the clouds, and also helps us revealing these cold clouds. In this paper we use the optical extinction, and FIR emission data exploring the clouds of the Cepheus Flare region.

2. Data analysis

2.1. Optical data

We examined the 15×15 degree region of Cepheus Flare centered at $RA = 21^h40^m, Dec = 68°$. We selected 26 subfields of this area with a size of 1×1 degree, according to the positions of clouds listed in LDN (Lynds , 1962) and Barnard catalogues. The optical extinction of these subfields were mapped by Dickman's (Dickman , 1978) method, counting stars in predefined grid cells up to a limiting magnitude in blue, using the data of the USNO A2.0 catalogue. The size of the reseau was $3' \times 3'$, and counting was performed up to 18^m in all subfields. Extinction free values of star counts were taken from a galaxy model by Wainscoat realised by L. Balázs in FORTRAN. The actual value of extinction in magnitudes can be obtained according to the following formula

$$A = \frac{1}{b} lg \left(\frac{n}{n_{ref}} \right), \qquad (1)$$

where n is the star count in the actual cell, n_{ref} is the reference count taken from the model up to the same limiting magnitude and b is the slope of the $lg\, n(m)$ function at the actual position taken from the model.

The individual objects we examined were defined by drawing ellipses, which contained each cell showing at least 2^m extinction (figure 1). We estimated the mass of each cloud based on the optical extinction, following Dickman (1978)

$$M = (\alpha_c d)^2 (N_{H_2}/A_V) \mu \sum_i A_V^i \qquad (2)$$

where α is the size of a grid cell in radians, d is the distance of cloud, (N_{H_2}/A_V) is the considered ratio of H_2 column density and visual extinction, μ is the average mass of particles in the cloud and A_V is the visual extinction obtained. Distance data were taken from Hilton & Lahulla (1995).

2.2. Infrared data

The infrared colour excess were also mapped in 26 subfields identical to the subfields of the extinction maps. Colour excess is related to the temperature of

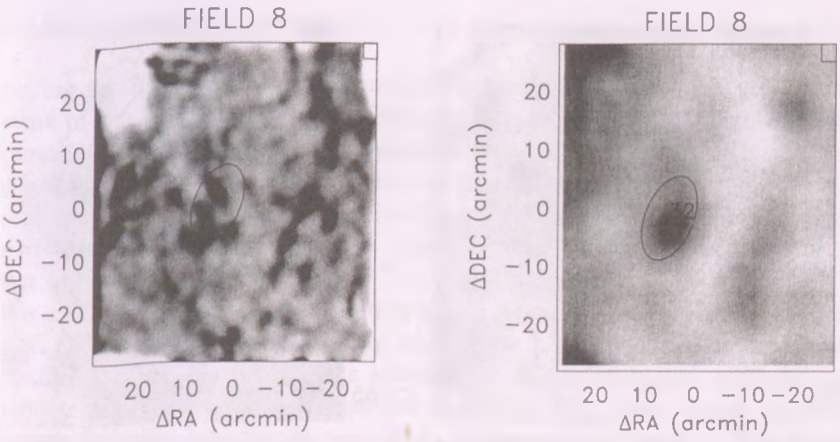

Figure 1: 100 μm excess and extinction map of LDN 1168 field containing the object no. 32 of our sample. $E_{max} = 1.05\,\mathrm{M\,Jy\,sr^{-1}}$, $A(B)_{max} = 3.0^m$, field center: $RA = 20^h56^m18^s$, $Dec = 67 \circ 41'16"$.

the dust, emitting a $10 - 20$ K thermal radiation, higher excess values indicate lower dust temperatures. Colour excess was computed from the HIRES 60 and 100 μm data according to the definition $E_{100} = I_{100} - I_{60}/\theta$, where θ is the characteristic I_{60}/I_{100} intensity ratio of galactic cirrus emission ≈ 0.2 (figure 1). HIRES data were calibrated by the COBE DIRBE through the ISSA data

The colour temperature map of the whole region were computed fitting a modified Planck-function to the DIRBE 100, 140 and 240 μm data, assuming a ν^2 emissivity law (figure 2). We have determined the DIRBE colour temperature, the average and maximal extinction, the average and maximal 100 μm excess, and the average ratio of extinction and 100 μm excess inside for all of the individual objects.

Searching for starless cores To find out cores with no stars we considered, in addition to the extinction and infrared maps described above, the positions of young pointlike sources in the region examined. The positions of these pointlike objects were taken from M. Kun (Kun , 1998). Considering this position data we selected the cloud cores having no such object. We also compared the positions of previously detected molecular emission in ^{13}CO (Yonekura et al., 1997) and NH_3 lines (Jijina et al. , 1999) to those of our clouds.

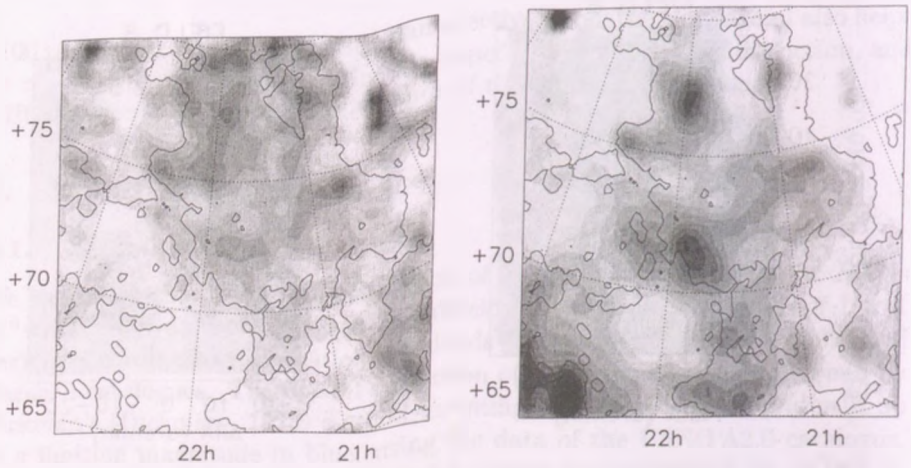

Figure 2: Overall distribution of the infrared colour temperature and 100 μm optical depth in the Cepheus Flare drawn from the DIRBE data with the 1.5 K km s^{-1} CO contour overlaid.

3. Results

General view We obtained from the DIRBE 100, 140 and 240 μm data $T_D \approx 17$ K typical temperature of the examined region. The lowest DIRBE temperature values in the region were $T_D \approx 15$ K.

Individual objects We have defined 61 objects on the subfields of extinction maps. All of these show more than 2^m maximal extinction by definition. In the case of the most opaqe ones the maximum values of extinction obtained is greater than 4^m. In the case of some objects, the maximum colour excess observed reaches or exceeds $2\,M\,Jy\,sr^{-1}$ indicating that, their temperature is notably lower than that of galactic cirrus. We recognised 31 objects with this high colour excess.

Considering the positions of YSO candidates and H_α emission stars we recognised 41 clouds in our sample suspected to be starless. We examined the former molecular measurements in ^{13}CO and NH_3 and we found 27 objects associated with molecular detections.

4. Discussion

According to the DIRBE colour temperature map the $T_D \approx 17\,K$ typical temperature of the region is obviously lower than its environment, which shows the characteristic temperature of the galactic cirrus emission $T_D \approx 18\,K$. This low temperature region can also be observed in the optical depth and the ^{12}CO contour map indicating higher density (figure 2). In the positions of our clouds defined the DIRBE temperature is typically even lower, $T_D \approx 15\,K$ for the coldest ones.

We can trace the optical extinction up to $A_B \approx 4^m$ and recognise 61 dense clouds. Constrained by the limiting magnitude higher extinction values were not available. We have 7 objects showing an exinction higher than 4^m, and 18 objects show a maximal extinction less than 3^m. The values of average extinction in individual clouds were all in the range of $1^m.7 - 2^m.5$. The mass of individual clouds obtained from these extinction values was found between 50 and $200\,M_\odot$ in agreement with former theoretical predictions.

In the positions of the densest clouds the colour excess can grow above $3\,M\,Jy\,sr^{-1}$, however the highest extinction does not always coincide with the highest colour excess values. In some cases the dense clouds contain embedded heating sources. Such objects even if their extinction exceeds 3 or 4^m, have low colour excess values even in the position of the maximum. On the other hand, in the case of all clouds showing high colour excess values, the maximum extinction is higher than 3^m.

There are 20 objects among the 61 defined containing one or more YSO candidates, H_α emission stars, or both of them. From te 41 suspected starless core 21 shows notably low temperature acoording to colour excess maps.

Considered the former CO and NH_3 detections 23 of our clouds, 7 of the suspected starless clouds with notably low temperature, are situated in a ^{13}CO cloud, and 9 clouds, 1 of the suspected starless cold clouds, show ammonia peaks.

4.1. Summary

We have mapped the extinction in blue, and the $100\,\mu m$ excess in 26 subfields with a size of $1° \times 1°$ of the Cepheus Flare region looking for dense cold clouds with no embedded pointlike protostellar objects. We found 61 dense clouds, 21 among them show an extinction higher than 3^m, have higher $100\,\mu m$ excess than $1\,M\,Jy\,sr^{-1}$, and containing no embedded star. Some of them can be recognised in ^{13}CO and NH_3 lines. We have determined the infrared colour temperature

of these clouds from DIRBE measurements, and these data also indicated low temperature. We are intended to use ISOSS 170 μm data combined with IRAS 100 μm to obtain a higher resolution colour temperature map. We are also intended to perform further radio measurements in NH_3 lines to find out the physical conditions in the clouds, which are found to be the most promising in the aspect of exposing observationally the very beginning phase of low mass star formation.

Acknowledgements

We would like to thank Lajos Balázs for supplying his FORTRAN program of Wianscoat model, Mária Kun and Péter Ábrahám for their useful help. This research has made use of the USNOFS Image and Catalogue Archive operated by the United States Naval Observatory, Flagstaff Station (http://www.nofs.navy.mil/data/fchpix/). This work was funded by the OTKA project no. T034998.

References

Dickman, R. L. 1978, AJ, 83, 363

Hilton, J., Lahulla, J., F. 1995, A&AS, 113, 325

Jijina, J., Myers, P., C., Adams, F., C., 1999, ApJS, 125, 161

Kun, M. 1998, ApJS, 115, 59

Lagache, G., Abergel, A., Boulanger, F., Puget, J.-L., 1998, A&A, 333, 709

Lynds, B., T. 1962, ApJS, 7, 1

Yonekura, Y., Dobashi, K., Mizuno, A., Ogawa, H., Fukui, Y. 1997, ApJS, 110, 21

Comparison of the large scale structure of the ISM in the 2^{nd} and 3^{rd} Galactic Quadrants

Vera Könyves[1] and Csaba Kiss[2]
[1]Eötvös Loránd University, Department of Astronomy
H-1518 Budapest, P.O.Box 32., Hungary
[2]Konkoly Observatory of the Hungarian Academy of Sciences
H-1525 Budapest, P.O.Box 67., Hungary
E-mail:[1]V.Konyves@astro.elte.hu,[2]pkisscs@konkoly.hu

Abstract

In this paper we are questing the large scale structure of the interstellar medium (ISM) using IRAS/ISSA 60 and 100 μm maps in the 3^{rd} Galactic Quadrant (GQ). Here we identified 41 loop-like intensity enhancements and analysed their far-infrared (FIR) properties. We found major differences in the distribution and characteristics of these features when comparing the results of the 2^{nd} and the 3^{rd} GQs. This discrepancy can be satisfactorily explained by basic differences of the structure of the ISM in these two Galactic Quadrants.
Keywords: *ISM, far-infrared: diffuse emission, galactic structure*

1. Introduction

Shell or arc like local density enhancements have been long since known. These structures may be formed by various processes and are reported in many tracers of the ISM, including radio, infrared, optical, ultraviolet and X-ray wavelengths. Most of the loops are explained as dense expanding shells of supernova (SN) explosions and stellar winds of supermassive stars. Moreover it is just possible that gas and dust loops form as a result of supersonic turbulences of the interstellar medium.

Loop-like structures were detected in the far-infrared wavelength range owing to the features of the dust emission and the characteristics in the distribution of young embedded objects. Loops containing diffuse and discrete emission can be found on IRAS images. Schwartz (1987) catalogued 16 star-forming loops in the outer Galaxy ($60° \leq l \leq 300°$ and $|b| \leq 7°$). The study by Marston (1996) presented IRAS Skyflux images of 49 suspected shells in the environment of galactic Wolf-Rayet stars. One of the most prominent far-infrared loops, the Cepheus bubble was discovered by Kun et al. (1987). The 2D projected easily visible ring, both at 60 and 100 microns, might well be a result of stellar winds

from massive stars in the Cep OB2 associations and several supernova events. Besides these events the infall of high-velocity clouds from the galactic halo has also been proposed to form large shells in the HI disc (Tenorio-Tagle, 1980). The North Celestial Pole (NCP) loop is the most remarkable example of infalling cloud – galactic disc interactions (Meyerdierks et al. , 1991).

Tóth et al. (1996) performed a survey of FIR loops in the 2^{nd} Galactic Quadrant ($90° \leq l \leq 180°$). This survey extended to high galactic latitudes ($-90° \leq b \leq 90°$) and significantly increased the number of known loops (141).

In this paper we present the results of a similar survey in the 3^{rd} Galactic Quadrant ($180° \leq l \leq 270°$; $-90° \leq b \leq 90°$), as part of our all-sky survey program.

2. Data analysis

2.1. Searching for loops on IRAS/ISSA images

The visual search for loop like features has been carried out on the computer readable, zodiacal light removed ISSA (IRAS Sky Survey Atlas) plates (Wheelock et al., 1994) especially at 60 and 100 μm. The investigation required huge connected areas, much larger than the $12.^{\circ}5 \times 12.^{\circ}5$ sized ISSA maps. The final images (with a size of $\sim 40° \times 40°$) on which the search was carried out were built up by using the "geom" and "mosaic" procedures of the IPAC-Skyview package.

According to the definition (Tóth et al., 1996) loops must show an excess FIR intensity as compared to its surrounding. A shell - by definition - must be at least 60 % of a complete ellipse-shaped ring. It may consists of a set of bright spots, or may be a diffuse ring or part of a ring.

2.2. Parameters of the loops

Using the IPAC-Skyview package, we fitted an ellipse to our suspected loops on the 100 μm ISSA images. The fitted parameters were the central galactic coordinates, the minor and major semiaxes of the ellipse and the inclination of the major axis to the circle of galactic latitude at the center of the ellipse. This was defined to be '+' from East to North.

We extracted a radially averaged surface intensity profile for the loops, extended to a distance of twice the axes of the fitted ellipse, using 20 concentric ellipsoidal rings. In the following calculations we used these surface-brightness profiles to obtain e.g. the significance of the loops.

Loop-like intensity enhancements were searched by eye on our ISSA mosaic maps because man's eye is the best pattern-recognition tool, especially in such cases when strict role can hardly be defined. In order to filter out many subjective effects due to the eye-investigation and check if our loops really show the FIR intensity excess over the local background, we derived a "significance" parameter, denoted as "Ψ" in the following. Ψ was defined as the relative intensity excess over the background in the radially averaged intensity profile (for a more detailed explanation see Kiss et al. 2002).

Another characteristic of the loops is the "color index" $\Delta I(60)/\Delta I(100)$, defined as the slope of the COBE/DIRBE corrected ISSA 60 and 100 μm scatter plot, which may account for temperature differences in the shells.

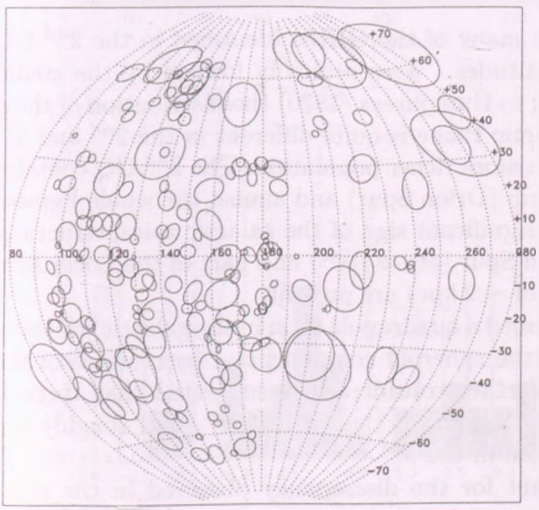

Figure 1: Sky distribution of GIRLs in the 2^{nd} and 3^{rd} GQs (galactic coordinate system). Ellipses were drawn using the fitted parameters of the loops (see text).

3. Statistical results

In the 3^{rd} GQ we found 41 Galactic far-InfraRed Loops (GIRLs), identified on ISSA 100 μm images. The catalogue is available at the following URL: `http://astro.elte.hu/IRASLoops3/IRASLoops3e.html`. The distribution of GIRLs in the 2^{nd} and 3^{rd} Galactic Quadrants is presented together in Fig. 1.

We have defined a characteristic size for our loops as the geometrical mean of the semi minor and -major axis of the fitted ellipse, $\langle R_{eff} \rangle = \langle \sqrt{a_i \times b_i} \rangle_i$.

This yielded $\langle R_{eff} \rangle = 3.'2$ and $3.'9$ for the 2^{nd} and 3^{rd} quadrants, respectively.

The distribution of GIRLs found in the 2^{nd} and 3^{rd} GQs (see Fig 2.) were expected to somehow reflect the exponential disc hypothesis. The Galactic Disc contains most of the ISM in the Galaxy, accordingly regions closed to the galactic plane should be the most populated parts of sky in loops, and this number should decrease nearly exponentially by the increasing galactic latitude.

Color indices distribute uniformly in galactic latitude and approximately show cirrus-like color, in contrast to the 2^{nd} GQ where a significant deviation can be observed at low galactic latitudes to higher color indices.

3.1. Comparison of the GIRL distribution in the 2^{nd} and 3^{rd} Galactic Quadrants

As shown by Kiss et al. (2002) many of the GIRLs identified in the 2^{nd} GQ - and located at low galactic latitudes - were probably formed by the stellar wind of massive stars. According to Humphreys (1970) the distribution of these energetic sources along the Galactic Plane is quite different in the 2^{nd} and 3^{rd} GQs, since the 2^{nd} one contains a more richer population. The 2^{nd} GQ contains a significant part of the Local Arm (Orion Spur) and almost the whole Perseus Arm. In the 3^{rd} GQ there is no significant sign of the galactic spiral structure, only a small fraction of the Orion Spur (at $l \approx 180°$) and part of the Local Arm (along $l \approx 270°$ up to a distance of ~ 2 kpc) are present.

Blitz and Spergel (1991) assumed a quadrupole term in the galactic potential derived from the asymmetry of the spheroid component. Observations of the 21 cm absorpsion features and further considerations suggested that there is roughly 20 % more gas in the 4^{th} quadrant than in the 1^{st}, and roughly the same amount more in the 2^{nd} than in the 3^{rd}.

These differences may account for the discrepancy observed in the characteristics in the GIRL properties and distribution in the 2^{nd} and 3^{rd} GQs. Additional differences between the two quadrants may be conspitious because of the relatively high number of small arcs and shells which were ignored in the 3^{rd} GQ, while kept in the 2^{nd}. These small features did not show an obvious FIR intensity excess over the background. Smaller bubble candidates of this quadrant - perhaps formed by turbulence in a lower amount of ISM - cannot form shells dense phased and bright enough to significantly exceed the background intensity. On the other hand loops may grow larger in the 3^{rd} GQ than in the 2^{nd} in the case of the same input energy due to the smaller amount of ISM .

It seems that the mass and density in the 3^{rd} GQ are not high enough to

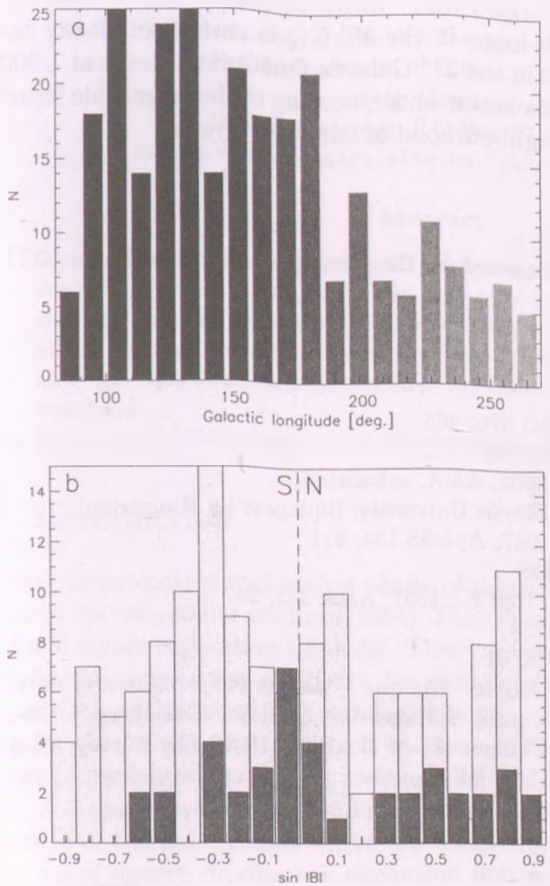

Figure 2: Distribution of GIRLs in the 2^{nd} and 3^{rd} GQs. (a) Loop-counts vs. galactic longitude. (b) Loop-counts vs. galactic latitude for the 2^{nd} quadrant (light grey bars) and for the 3^{rd} GQ (dark grey bars).

produce star-formation in an efficiency comparable to that in the 2^{nd} GQ. The relatively low intensity excess of the loops in the 3^{rd} GQ also explains the fact, that these loops show cirrus-like $\Delta I(60)/\Delta I(100)$ values, in contrast to the 2^{nd} quadrant.

4. Summary

In this paper we presented the results of a search for GIRLs (Galactic InfraRed Loops) in the 3^{rd} Galactic Quadrant. Our objects are suspected to be the remnants of high pressure events, seen as far-infrared intensity enhancements

on IRAS/ISSA plates.

The investigation for FIR loops in the 3^{rd} GQ is part of an all-sky survey program, - which was first set in the 2^{nd} Galactic Quadrant (Kiss et al. , 2002) - and will have an impact on the better understanding of the large scale structure of the ISM in the galactic neighbourhood of our Solar System.

Acknowledgements

This research was partially supported by the Hungarian Research Found (OTKA), under the number T034998.

References

Blitz L., Spergel D.N., 1991, ApJ 370, 205
Humphreys R.M., 1970, ApJ 75, 602
Kiss Cs., Moór A., Tóth L.V., 2002, A&A, submitted
Könyves V., 2001, MS Thesis, Eötvös University, Budapest [in Hungarian]
Kun M., Balázs L.G., Toth I., 1987, Ap&SS 134, 211
Marston A.P., 1996, AJ 112, 2828
Meyerdierks H., Heithausen A., Reif K., 1991, A&A 245, 247
Schwartz P.R., 1987, ApJ 320, 258
Tenorio-Tagle, G., 1980, A&A 88, 61
Tóth L.V., Kiss Cs., Moór A., 1996, in: *The role of dust in the formation of stars*, eds. Käufl H.U., Siebenmorgen R., publ. Springer-Verlag Berlin Heidelberg, p.125-128
Wheelock S.L., Gautier T.N., Chillemi J., et al., 1994, IRAS Sky Survey Atlas Explanatory Supplement, JPL Publ. 94-11

SUPERSHELL AROUND CAS OB5

Attila Moór[1] and Csaba Kiss[2]
[1]Eötvös Loránd University, Department of Astronomy
H-1518 Budapest, P.O.Box 32., Hungary
[2]Konkoly Observatory of the Hungarian Academy of Sciences
H-1525 Budapest, P.O.Box 67., Hungary
E-mail:[1]A.Moor@astro.elte.hu,[2]pkisscs@konkoly.hu

Abstract

We identified a large expanding HI shell around Cas OB5 analyzing Leiden/Dwingeloo HI data. With the help of objects apparently associated with the bubble, we could estimate a distance of 2.5 kpc and we determined the main characteristics of the shell. Model calculations have shown that Cas OB5 had the power to form the observed structure in its neighbourhood.
KEYWORDS: *ISM:bubbles – ISM:individual(Cas OB5)*

1. Introduction

Supernova explosions and stellar winds of massive stars generate strong shock waves in the interstellar medium (ISM). They sweep out the surrounding gas and dust and create expanding HI shells. There are many evidences that these large shell-like structures are relatively common in the disk of the spiral galaxies. In our Galaxy Heiles (1979) cataloged many large HI shells. In the galaxy M31 Brinks (1981) also managed to observed similar features. The kinetic energy of the largest structures are exceeded by a few orders of magnitude than that of a single event. Formation of these bubbles can be explained by the influence of OB associations where the massive stars of the association provide a source of energy driving the expansion first by their stellar wind and then the subsequent SN events enlarge the former hole. In the last decades several neutral hydrogen shells were investigated apparently related to galactic OB associations and open clusters (Per OB2, Sco OB2, (Sancisi, 1974); Cep OB3, (Read, 1980);Cep OB2, (Kun et al., 1987); Lac OB1, (Cappa de Nicolau & Olano, 1990); Scorpio-Centaurus, (de Geus, 1992); Ara OB1 (Rizzo & Bajaja, 1994); Orion OB1, (Brown et al. , 1995); Ocl 352, (Normandeau et al., 1996); Perseus OB1, (Cappa & Herbstmeier, 2000)). In this paper we present the results of an investigation of neutral HI structure of the ISM in the vicinity Cas OB5. In this area a large elongated HI shell was found by (Fich, 1986)

with a center position of $l = 117.5°, b = 1.5°$. It was also suspected that some SN events occured in the pre-rarified medium of the HI shell and these supernovae actively engaged in enlarging the HI shell. Schwartz (1987) found a far infrared ring ($l = 118°, b = 2°$, diameter $= 5°$) close to the HI shell defined by Fich. Using the diffuse infrared emission originating from this region Kiss et al. (2002) identified a far infrared loop GIRL 117+01 in a position similar to Schwartz's.

2. HI data analysis

In order to analyze the distribution of HI gas in the environment of the Cas OB5, the data were taken from the Leiden Dwingeloo HI survey by Hartmann et al. (1997). The Leiden Dwingeloo survey covers the entire sky above declination $-30°$, on a half degree grid both in l and b, with half-power beamwidth (HPBW) of 0.6°, sampled at $1.03\,\mathrm{kms}^{-1}$. The limiting brightness temperature sensitivity was $< 0.07\,\mathrm{K}$.

Investigating the HI distribution around Cas OB5 we analyzed the HI emission in the region $108° \leq l \leq 127°$ and $-7° \leq b \leq 9°$ within the velocity interval from $-100\,\mathrm{kms}^{-1}$ to $+30\,\mathrm{kms}^{-1}$. This investigation revealed a large HI shell in the velocity range from $-60\,\mathrm{kms}^{-1}$ to $+3\,\mathrm{kms}^{-1}$ surrounding the OB association. In Fig. 1 we display the distribution of the neutral hydrogen emission integrated within the velocity range above.

The projected image of the loop extends to $\sim 8.5°$ in both directions. The lowest HI brightness temperature in the hole occures at the position of $l = 117.5°$, $b = 0°$.

When the emission is optically thin, one can determine the neutral hydrogen column density distribution N_{HI} in this region. This assumption was tested comparing IRAS 100μm with HI data. At each position the column density were determined from the current HI emission multiplied by $1.8224 \times 10^{18}\,(\mathrm{Kkm/s})^{-1}\mathrm{cm}^{-2}$ (Hartmann et al., 1997).

To estimate the HI mass of the shell we performed a removal of the background from the map. The background was determined by fitting a third order polinomial in b through an unobscured region close to the shell. The final mass was calculated by summing up the column densities of the individual points which we associated to the shell. We obtained $M_s \sim 1.0 \pm 0.2 \times 10^5 \times d^2[\mathrm{kpc}] M_\odot$ taking into account the He mass as 40% of total hydrogen mass.

The approaching side of the shell has a mass twice than that of the receding side. This feature sets the true systemic velocity of the center of the expansion

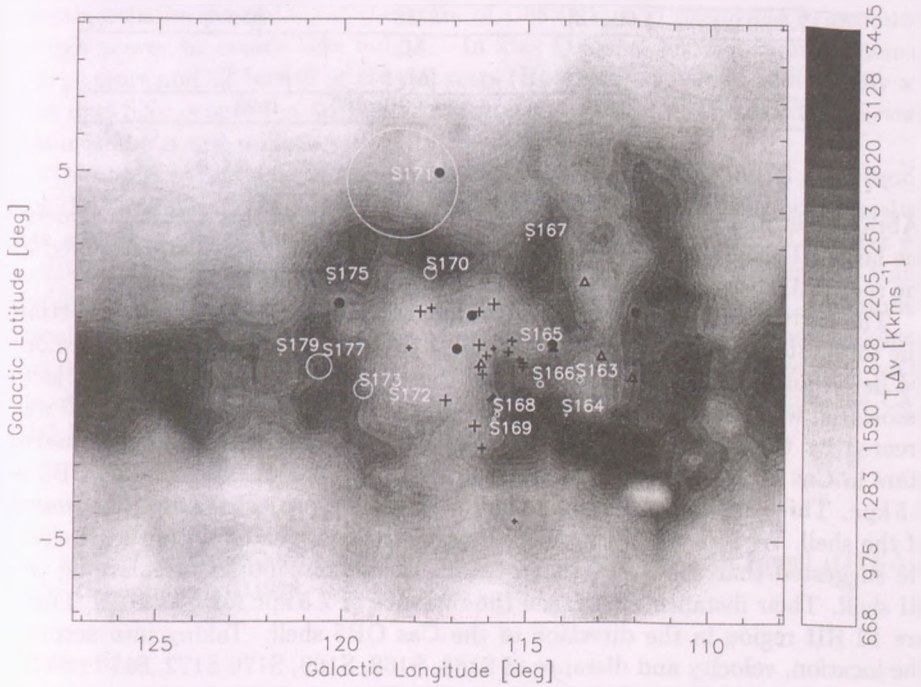

Figure 1: The integrated HI emission map through the velocity range $-60\,\mathrm{kms}^{-1}$ to $+3\,\mathrm{kms}^{-1}$. The O and B stars of the association denote plus signs, the pulsars and SNRs indicate triangle and filled circle signs respectively. Moreover we displayed the Sharpless HII regions (Sharpless, 1959) ($113° \leq l \leq 122°$ and $-5° \leq b \leq 6°$) indicated by circles which have diameter show the angular extent of the HII region.

to $v_{LSR} \approx -38\mathrm{kms}^{-1}$ and provides a momentum-weighted expansion velocity

Table 1: Parameters of the shells

Name	velocity interval [kms^{-1}]	v_{sys} [kms^{-1}]	v_s [kms^{-1}]	distance [kpc]
G117.5+0.0	[-60,+3]	-38	20	2.5
	R_s [pc]	M_s [$M_\odot$]	n_0 [cm^{-3}]	
G117.5+0.0	187	$6.32 \pm 1.26 \times 10^5$	0.93	

(Ábrahám et al., 2000) of $v_{eff} \approx 20 kms^{-1}$. According to this systemic velocity the large HI shell belongs to the Perseus spiral arm which is clearly outlined in the second Galactic quadrant on the HI maps of Kulkarni et al. (1981).

The derivation of the kinematic distance is quite uncertain in this direction due to the streaming motions in the galactic disk (Humphreys, 1976). Therefore we determined the distance of the shell based on the distance of the objects associated with the bubble. We suggest that the expanding shell structure was created by the stellar wind and subsequent supernova explosions of massive stars in Cas OB5. According to Humphreys (1978) the distance of Cas OB5 is 2.5 kpc. Three supernova remnants and a pulsar are projected onto the interior of the shell. As Fich (1986) verified, these SNRs are located within a HI shell. He suggested that these supernovae are actively contributed in enlarging the HI shell. Their distance strengthen the distance of 2.5 kpc for Cas OB5. There are 13 HII region in the direction of the Cas OB5 shell. Taking into account the location, velocity and distance of S163, S168, S169, S170 S172 ,S173 , S177, they may be part of the shell structure. The distance of these objects conform the distance of 2.5 kpc. Therefore we finally adopt 2.5 kpc as distance to this bubble.

3. Results

We summarize the characteristics of the shell - based on the distance of 2.5 kpc - in Table 1. Using the formulae by McCray & Kafatos (1987) one can estimate the kinematic age (t_{kin}) and the energy (E_s) necessary to form the shell.

$$R_s = 267 \times (L_{38} \times t_7^3 / n_0)^{\frac{1}{5}} \text{ pc} \quad (1)$$

$$v_s = 15.7 \times (L_{38} \times t_7^{-2} / n_0)^{\frac{1}{5}} \text{ kms}^{-1} \quad (2)$$

where $L_{38} = (L_w + L_{SN})/10^{38}$ergs/s, L_w is the combined mechanical luminosity of all the stellar winds in the association, L_{SN} is the mean power produced by the supernova explosions, $t_7 = t/(10^7\,\mathrm{yr})$ is the age of the shell and n_0 is the ambient gas density. In the case of G117.5+0.0 $t_{kin} = 5.6\,$Myr and $E_s = 1.57 \times 10^{52}\,$erg. Using the Starburst99 model (Leitherer et al., 1999) we investigated the possibility if the stars of Cas OB5 had been able to produce enough power to create this bubble. In Cas OB5 we know 3 main-sequence O-type stars and 11 late O or B-type stars (Humphreys, 1978). Additionally at least four SNe occured in the association (see in Sect. 2.). The oldest observed pulsar is about one million year old (Taylor et el., 1993).

The input parameters of the model were the following: the initial mass function IMF was $\xi(\lg M) = A{*}M^{-2.1}$, spontaneous star formation, the most massive star was $M = 100\,M_\odot$ and we assumed the stellar wind model by Leitherer et al. (1992). After six million years the model yielded four main-sequence O stars and 9 late O or B stars, 10 SN events (4 events in the last 1.2 Myr). The model association supplied 2.03×10^{52}erg to its environment. Based on the formulae, this resulted $R_s = 202$pc and $v_s = 19.8\mathrm{kms}^{-1}$, which is in good agreement with the observed characteristics of the shell. Finally we can conclude that the Cas OB5 had the power to form this large HI shell.

Acknowledgements

The research was partially supported by the Hungarian Research Found (OTKA), under the number T034998

References

Ábrahám P., Balázs L.G., Kun M., 2000, A&A 354, 645
Brinks,E. 1981, A&A 95, L1
Brown A.G.A., Hartmann D., Burton W.B., 1995, A&A 300, 903
Cappa C.E., Herbstmeier U., 2000, AJ 120, 1963
Cappa de Nicolau C.E., Olano C.A.., 1990, Rev. Mex. Astron. Astrofis., 21, 273
de Geus E.J., 1992, A&A 262, 258
Fich M., 1986, ApJ 303, 465
Hartmann D., Burton W. B., 1997, Atlas of Galactic Neutral Hydrogen, Cambridge: Cambridge Univ. Press
Heiles C., 1979, ApJ 229, 533
Heiles C., 1990, ApJ 354, 483
Humphreys R.M., 1976, ApJ 206, 114
Humphreys R.M., 1978, ApJS 38, 309

Kiss Cs., Moór A., Tóth L.V., 2002, A&A, submitted
Koo, B.-C., Heiles C., Reach W.T., 1992, ApJ 390, 108
Kulkarni S.R., Blitz L., Heiles C., 1981, ApJ 259, L63
Kun M., Balázs L.G., Tóth I., 1987, Ap&SS 134, 211
Leitherer, C., Robert, C., Drissen, L 1992, ApJ 401, 596
Leitherer, C. et al. 1999, ApJS, 123, 3
McCray R., Kafatos M.C., 1987, ApJ 317, 190
Normandeau M., Taylor A.R., Dewdney P.E., 1996, Nature, 380, 687
Read P.R., 1980, MNRAS 193, 487
Rizzo J.R., Bajaja E., 1994, A&A 289, 922
Roberts W.W., 1972, ApJ 173, 259
Sancisi, 1974, In: Galactic Radio Astronomy, eds. F. J. Kerr, S. C. Simonson III, Reidel, Dordrecht, p. 115
Schwartz P.R., 1987, ApJ 320, 258
Sharpless S., 1959, ApJS 4, 257
Taylor J.H., Manchester R.N., Lyne A.G., 1993, ApJS 88, 529

Variable Stars

T. Borkovits
Sz. Csizmadia
Z. Csubry
Zs. Kővári
L. Patkós
M. Pócs
G. Ribárik

Period Variations in IM Aurigae

Tamás Borkovits[1] and Szilárd Csizmadia[2]
[1]Baja Astronomical Observatory of Bács-Kiskun County,
H-6500 Baja, P.O.Box 766. Hungary,
[2]Konkoly Observatory of Hungarian Academy of Sciences,
H-1525 Budapest, P. O. Box 67. Hungary,
E-mail:[1]borko@electra.bajaobs.hu,[2]csizmadi@konkoly.hu

Abstract

In the present paper we study the behaviour of the $O-C$ diagram of IM Aurige system. We confirm the former statement of Bartolini & Zoffoli (1986) that the periodic term arise from light-time effect (LITE). We demonstrate that supposing an almost edge-on orbit for the third companion, its possible mass is in good agreement with the amount of the third light found from the reanalyzed BV light-curve of Gülmen et al. (1985). We show that another kind of variation (secular or sudden) is also present in the $O-C$ curve. We give a parabolic ephemeris for this phenomenon. Finally we conclude, that neither mass-flow nor some orbital perturbations of the third body can cause this effect.
Keywords: *binaries: close – binaries: eclipsing – Stars: individual: IM Aur*

1. New light-curve solution

Gülmen et al. (1985) published a BV light-curve obtained with a one-channel photomultiplier-based photometer. There are several circumstances why a new light-curve solution is required.

These are the followings:

(i) The primary component of IM Aur was taken to be a B9 star according to Mammano et al. (1967) and that is why its surface temperature was fixed at 10 500K in Gülmen et al. (1985). However, other studies give earlier spectral type for the primary (e.g. Bruhweiler et al. 1986 give B5V or B6V). In our study we accepted B7V from SIMBAD database for the main component, which would yield a higher surface temperature ($T_1 = 13\,000$K).

(ii) The presence of the third companion was not considered in the former analysis. Nevertheless, according to LITE solution of Bartolini & Zoffoli (1986) as well as our new one (see below) this star might produce extra radiation increasing the luminosity of the system. Disregarding this effect should necessarily

modify the physical parameters of the eclipsing pair. Regarding these facts we decided to reanalyse the original observational data of Gülmen et al. (1985).

The following set of parameters was adjusted: inclination (i), secondary's surface temperature (T_2), surface potentials of the components (Ω_1,Ω_2), secondary's luminosity (L_2) and third light (l_3). As an initial parameter set, the solution of Gülmen et al. (1985) was applied. We used the Wilson-Devinney Code (Wilson, 1998). Instead of the normal points (which were used in Gülmen et al. 1985) the original individual points were applied.

Our best fit was obtained using Mode 5 of Wilson-Devinney Code, which means that the secondary star fills out its Roche-lobe. A relatively high value of l_3 was obtained in this mode (approximately 9%). The results of the solution will be presented somewhere else. Here we concentrate only for the third light.

From the light-curve solutions in different colours, the colour index of the tertiary component can be determined from the colour index of e.g. the primary by the following expression:

$$(B-V)_3 = -2.5\left[\log\left(\frac{L_{3,B}}{L_{3,V}}\right) - \log\left(\frac{L_{1,B}}{L_{1,V}}\right)\right] + (B-V)_1, \qquad (1)$$

where $(B-V)_i$ is referring to the i-th component's colour index, $L_3 \approx 4\pi l_3$ where l_3 is the third light obtained from the light-curve solution, and the luminosities of the components are given in arbitrary units as used by Wilson-Devinney Code. Supposing that the B7V primary has a $(B-V) = -0\overset{\text{m}}{.}13$, we get that the $(B-V)$ colour index of the tertiary is $+0\overset{\text{m}}{.}25$ magnitude. If this object is a main-sequence one its spectral type should be about A8V, which results $L_3 = 8.6\mathrm{L}_\odot$ (Lang, 1992). Applying the mass-luminosity relation of McCluskey & Kondo (1972) the corresponding mass of the third object is $m_3 \approx 1.7\mathrm{M}_\odot$.

2. Period-variations

Up to now, it has been spent almost the same time since the discovery of the light-time effect of IM Aur by Bartolini & Zoffoli (1986) than the time span between the first published minima by Kondo (1966) and their work. Now we are at the position to realize that the $O-C$ curve reveals rather complex behaviour (see Fig. 1). A quasi-sinusoidal curve is superimposed onto some other kinds of period variations. For the first sight, this latter feature could be either a continous secular period decrease or an abrupt period change. Due to the short time interval over which the minima times are distributed and the relatively large amplitude of the periodic variation we are not the position yet

Table 1: The LITE solution of this paper comparing it with the earlier results. The orbital elements refer to the wide orbit of the eclipsing binary in the triple system. $f(m_3)$ is the mass-function of the tertiary, m_3 is its mass at different inclinations.

		present value	paper p.e.	Bartolini&Zoffoli (1986) value
P'	(d)	1372	1	1382
e'		0.59	10	0.7
ω'	(°)	279	7	300
τ'	(HJD − 2 400 000)	52085	25	52175
$a' \sin i'$	(10^6km)	158	9	186
$f(m_3)$	($M_\odot$)	0.084	0.015	0.124
m_3	90°	1.71	0.13	1.99
	60°	2.03	0.16	2.37
	30°	4.09	0.35	4.90

to decide which interpretation could be correct. Despite of this fact, we applied the usual quadratic description for the modelling of the long-term behaviour of our curve. The analysis of the $O - C$ curve was done by the same manner as it can be found in Borkovits & Hegedüs (1996) with one fundamental difference, namely that the parabola was not subtracted previously, but its coefficients were fitted simultanously with the Fourier-coefficients of the periodic terms.

The interpretation of the periodic terms in the $O - C$ variation as LITE seems to be less problematic. We examine this case firstly.

2.1. Light-time effect

The orbital elements of the close binary in the triple system, as well as the mass function of the tertiary component can be read in Table 1.

Assuming that the primary is a normal B7V star its mass is $m_1 = 4.5M_\odot$ (Lang, 1992). Adopting the mass ratio $q = 0.32$ from Gülmen et al. (1985) we obtain a total mass of $5.94M_\odot$ for the eclipsing pair. Using this, one can get a minimum mass of $1.67M_\odot$ for the third companion. Comparing the third-body mass calculated in Sect. 2 with the mass which was determined from the mass function for different visible inclinations (see Table 1) one can found that the orbit of the wide binary is can be seen almost exactly on the edge. (We have to

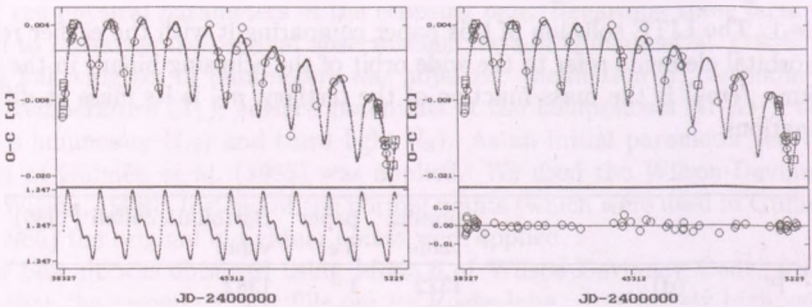

Figure 1: Left: The simultaneous LSQ parabola and Fourirer fit (above), and its derivative, the instantanous 'period' (below). Right: The LITE solution superimposed to the parabola (above), and the residuals (below).

note that since we have no any information about the direction of the nodes of the orbits, from the knowledge of the visible inclinations of the orbits we cannot tell anything about the mutual inclination of the two orbital planes.)

2.2. Secular variation

The following quadratic ephemeris was obtained by the simultaneous least-squares (LSQ) fit of a second order polinom and Fourier-terms containing a (fixed) fundamental frequency and its first two overtones:

$$\mathrm{MIN_I} = 2438327.7970(3) + 1.2472899(8)E - 1.73(12) \times 10^{-10}E^2 \qquad (2)$$

Interpreting this period change we examine first the possibility of some mass-flows, and then the rarely studied question: whether the perturbations of the third companion could cause such kind of variation?

2.2.1. Mass flow in (from) the system

The period decrease suggests some mass-flows from the more massive primary to the secondary, or some mass-loss events. For the first sight, it seems to be in a good agreement with the IUE UV spectrum data (Bruhweiler et al., 1986), where sharp absorption features of the spectra arising in a shell or mass stream were observed. The relation between the mass and the period variation is (see

e.g. Tout & Hall, 1991):

$$\frac{\dot{P}}{P} = -\frac{2\dot{m}_{12}}{m_{12}} + \frac{3\dot{m}_2(m_2 - m_1)}{m_1 m_2} + 3K, \tag{3}$$

where the first term in the rhs. stands for the total mass-loss of the system, the second one describes conservative mass-exchange, while the third one is the so-called Alfvén-term. Since the main component has a B spectral type we think this latter term can be neglected. If the mass-loss would be the only source of the observed period variation we obtain a value of $\dot{m}_{12} \approx 12.43 \times 10^{-7} M_\odot y^{-1}$. However, this value is three or four orders larger, than the usual annual rate of wind-driven mass loss of a typical B5-6V star. Calculating only with mass-flow from the primary component to the secondary one we get $m_2 = 6.03 \times 10^{-8} M_\odot y^{-1}$, which is again too large. So we have to look for some other interpretation.

2.2.2. Perturbations by the third body

The variations of the orbital elements of a double stellar system due to a distant third body were studied by several authors. The typical periods of the different classes of periodic perturbations are P, P', P'^2/P (see e.g. Söderhjelm, 1975). As it is well-known from the textbooks on celestial mechanics the longer the period of a perturbation the larger its amplitude. It is clear that only the third type of these perturbations (the so-called 'apse-node' terms) is interesting for us. As long as the orbit of the close binary is (almost) circular, the effect of the apsidal motion can be neglected, so we can concentrate to the nodal motion. Its typical amplitude (in the $O - C$ surve) is $A_n = (P/2\pi) i_1 \cot I$, where i_1 is the inclination of the eclipsing binary to the invariable plane, while I is the observable inclination of the invariable plane (Luyten, 1938). From the fact, that the ratio of the angular momenta of the two orbits is $G_2/G_1 \approx 11.6$, it follows, that $I \approx i'$ is a good approximation. According to the third light, if the tertiary is not a degenerate object the observable inclination of the wide orbit (i') must be greater than 80°, so $A_n \leq 0^d.035 i_1$. The approximate period of this nodal regression (see again Söderhjelm, 1975) is

$$P_n = \frac{4}{3}\left(1 + \frac{m_{12}}{m_3}\right)\frac{P'^2}{P}(1 - e'^2)^{3/2}\left(\frac{C}{G_2}\cos i_m\right)^{-1}, \tag{4}$$

where C is the total angular momentum, while $i_m \approx i_1$ is the mutual inclination of the two orbital planes. In the case of IM Aurigae $P_n \approx 1^a.3 \times 10^4 (\cos i_1)^{-1}$.

This (minimal) period is longer by almost 50% comparing with the value given by Mayer (1990) due to the smaller mass function and larger masses for the primaries. According to the quadratic term, in the last four decades the amplitude of the $O-C$ is about $0\overset{d}{.}02$ which evidently discloses the long period nodal regression as a possible source of this feature of our curve.

Acknowledgements

This work was supported by the OTKA F030147, and T030743 grants of the National Science and Research Found (Hungary).

References

Bartoloni, M., & Zoffoli, C., 1986, A&A 168, 377

Borkovits T., & Hegedüs T., 1996, A&AS 120, 63

Bruhweiler, F. C., Feibelman, W. A., & Kondo, Y., 1986, AJ 92, 441

Gülmen, Ö, Sezer, C., Güdür, N., 1985, A&AS 60, 389

Kondo, Y., 1966, AJ 71, 46

Lang, K.R., 1992, *Astrophysical Data*, Springer-Verlag

Luyten, W.J., Z. Astrophys. 15, 97

Mammano et al., 1967, Asiago Contr., No. 192

Mayer, P., 1990, BAIC 41, 231

McCluskey, G. E., Kondo. Y, 1972, ApSS 17, 134

Söderhjelm, S., 1975, A& 42, 229

Tout, C.A., Hall, D.S., 1991, MNRAS 253, 9

Wilson, R.E., 1998, *Computing Binary Star Observables*, Astron. Dept., Univ. of Florida

A NEW DISTANCE DETERMINATION WITH W UMA-STARS

Szilárd Csizmadia, László Patkós
Konkoly Observatory of the Hungarian Academy of Sciences
H-1525 Budapest, P.O.Box 67., Hungary
E-mail: csizmadia@konkoly.hu, patkos@konkoly.hu

Abstract

A new method is developed to determine geometrical and physical parameters of contact binary stars. Error of the mass-determination is only a few percent. We examined the possibility of using W UMa-stars as distance indicators.

KEYWORDS: *stars: evolution – stars: structure – method: distance determination – stars: individual: 44 Boo, BI CVn*

1. Introduction

W UMa-stars were suggested to use as primary distance indicators by Rucinski (1996). However, the Rucinski & Duerbeck's (1997) calibration shows relatively large error in the distance. Here we present our new method which is a combination of the Barnes-Evans–relation and the dynamical parallax method.

There are several methods for the determination of geometrical and physical parameters of contact binaries. Unfortunately, W UMa-stars are faint objects ($M_V = +1^m ... + 6^m$) and therefore there are only a few precise radial velocity curve available. The recent works of Lu and Rucinski (Lu & Rucinski, 1999, Rucinski & Lu, 1999 and references therein) yielded several new radial velocity curves of bright systems, but there are more and more discoveries of faint systems. Main advantage of our method that it does not require radial-velocity curve data.

2. The method

In usual case we have standard Johnson-Cousins V and R photometry and light-curve solutions for a certain contact binary. From the Barnes-Evans relation the apperant angular radii of the primary and the secondary can be derived.

The radii of the components can be written as follows

$$R_1 = \Phi_1 d/2, \qquad R_2 = \Phi_2 d/2 \tag{1}$$

$$R_1 = Ar_1, \qquad R_2 = Ar_2 \tag{2}$$

where $R_{1,2}$ are the radii of the components, $\Phi_{1,2}$ are the apperant angular radii of the components, d is the distance of the system, A is the semi-major axis of the orbit and $r_{1,2}$ are the fractional radii. The known quantities are $\Phi_{1,2}$ (from the VR photometry) and the $r_{1,2}$ (from the light-curve solution).

In that case

$$\frac{A}{d} = \frac{1}{2}(\frac{\Phi_1}{2r_1} + \frac{\Phi_2}{2r_2}) \tag{3}$$

where $\alpha = A/d$ is the apperant angular radius of the orbit.

Determining α we apply the dynamical parallax method. The equations are:

$$M_V = V - A_V + 5 - 5logd \tag{4}$$

$$d = \frac{A}{\alpha} \tag{5}$$

$$A^3 = P^2 M_{1+2} \tag{6}$$

$$M_{1+2} = \frac{1+q}{q} M_2 \tag{7}$$

$$M_V = 4.81 - 2.5logL_{1+2} \tag{8}$$

$$L_{1+2} = \frac{1+\lambda_V}{\lambda_V} L_{2,V} \qquad /\lambda_V = \frac{L_{2,V}}{{}_{1,V}}/ \tag{9}$$

$$L_{2,bol} = L_{2,V} 10^{-0.4BC_2} \tag{10}$$

$$L_{2,bol} = CM_2^{\delta}, \tag{11}$$

where the symbols mean the followings: M_V and V are the absolute and apperant visual magnitudes of the system, A_V is the interstellar absorption, P is the orbital period, M_{1+2} is the total mass, $M_2, L_{2,V}, L_{2,bol}$ are the secondary's mass, visual and bolometric luminosities, q is the mass ratio, L_{1+2} is the total visual luminosity, λ_V is the luminosity ratio and BC_2 is the bolometric correction for the secondary.

Constants C and δ in Eq. (11) were determined as we took mass and luminosity data at ZAMS from the theoretical modells of Claret and Gimenez (1992). These data pairs were fitted and $C = 0.68$ and $\delta = 4.63$ were found. We applied modells with $Z = 0.02$ which seems to be a good compromise, as W UMa stars were observed in open clusters after an age of about some hundred Myr as well as in old open and even in some globular clusters. According to our estimation the uncertainities in mass-luminosity law could cause no more

than $0.05 - 0.1 M_{\odot}$ error in the final results. We intend to apply the metallicity-period-colour-absolute magnitude relation of W UMa stars (Rucinski, 1997) to determine the constants in the mass-luminosity law more accurately.

The luminosity ratios of the light-curve solutions cannot be used directly for this procedure. A certain part of the luminosity of the primary is transferred to the secondary star. Therefore the real luminosity of primary is higher than the observed one. After this correction main-sequence mass-luminosity law can be used because primaries are on or a little above the main-sequence (Mochnacki, 1981). Assuming $L = CM^{4.63}$ we found that

$$(\frac{L_2}{L_1})_{corr} = q^{4.63} \tag{12}$$

During the procedure of the dynamical parallax method we used this ratio. In the case of semi-detached and detached systems - where no significant luminosity exchange is present - there is no need for this correction. (However, in that case the correct form of the M-L law can be different from the one used in this paper.)

The question is wether main-sequence mass-luminosity law can be applied in this case. Note that to determine the mass of the system we used the secondary component instead of the primary one which is a major difference from the previous similar photometric methods (e. g. Mochnacki, 1981, Maceroni & van't Veer, 1996) and yielded more accurate results due to the followings. Primary components which are the more massive ones can be evolved stars. Secondary components are less massive: masses of secondaries of late-type contact binaries are tipically less than 0.5 $M_{\odot}$ and in every known cases they are less than 1.2 $M_{\odot}$ (XZ Leo seems to have the most massive secondary component with $1.20 M_{\odot}$). Life-times of such stars on the main-sequence are longer than the age of the Universe. MS M-L law can be applied because we may expect that the secondary components are non-evolved main-sequence stars.

The situation could be complicated by mass-exchange. There are several theoretical modells of contact binaries but all of them predict mass-exchanges. The modell developed by Shu et al. (1979) was disproved e.g. by Mochnacki (1981). The thermal relaxation theory (TRO) which is frequently called cyclic theory states that such systems oscillate between semi-detached and contact phase on a time-scale of an order of ten million years (Lucy 1976, Flannery 1976, Robertson and Eggleton 1977). However, Mochnacki (1981) and recently Hazlehurst (2001) rejected TRO as evolution theory of contact binaries because we do not see appropriate number of β Lyr-type light-curves within the typical period intervalls of W UMa systems. Another evolutionary theory is the one of Mochnacki (1981) whose fundamental assumption is that the systems are

remaining in contact state during the evolution after forming a contact binary up to the hydrogen core exhaustion. After detailed investigations Kähler (1997) concluded that the rate of mass-transfer can be large in semi-detached phase but due to the nearly equal potentials there is very small mass-transfer in contact phase.

3. Application of the method

Results obtained by our method can be found in Table 1-2. In the case of 44 Boo we listed the results of Hill et al. (1989) and in the case of BI CVn we used the results of Liu & Tan (1989) (both of them are a combination of spectroscopic and photometric data). As one can see our results are in good agreement with the combined data. (Note that these results are free from any assumption of the exact form of mass-luminosity law).

Table 1: Comparison of data of 44 Boo obtained by different methods

Parameter	Hill et al. (1989)	Present study	Unit
M_1	0.98	1.04 ± 0.07	$M_\odot$
M_2	0.55	0.52 ± 0.03	$M_\odot$
R_1	0.87	0.85 ± 0.02	$R_\odot$
R_2	0.66	0.64 ± 0.02	$R_\odot$
L_1	0.53	0.62 ± 0.12	$L_\odot$
L_2	0.25	0.42 ± 0.08	$L_\odot$
A	2.01	2.04 ± 0.04	$R_\odot$

4. How far?

Usability of the method depends on the available limiting magnitudes. It is usual to observe stars at magnitude 27 with very large telescopes. In this case W UMa stars can be used as distance-indicators up to 1.6 Mpc. It is not hopeless to reach the limiting magnitude of 30. Then the available distances could be located as far as 6 Mpc.

Regarding the possibilities of the largest Hungarian telescope (1m RCC telescope of the Konkoly Observatory) the approximately distance limit using W UMa's is 50kpc. This allow us to use them as galactic distance indicators.

Table 2: Comparison of data of BI CVn obtained by different methods

Parameter	Liu and Tan (1988)	Present study	Unit
M_1	1.18	1.11 ± 0.05	$M_\odot$
M_2	1.02	0.96 ± 0.04	$M_\odot$
R_1	1.49	1.15 ± 0.06	$R_\odot$
R_2	1.40	1.08 ± 0.06	$R_\odot$
L_1	4.06	2.40 ± 0.36	$L_\odot$
L_2	3.52	2.09 ± 0.36	$L_\odot$
A	2.89	2.85 ± 0.04	$R_\odot$

5. Summary

The results of our investigations can be summarized as follows.

1. In order to compute absolute dimensions (masses, radii, luminosity, semi-major axis, distance) a new method was suggested. The method requires only photometric data. Although we have checked the results only for two stars agreement is good with other results and the accuracy is relatively high in masses.

2. We also suggest the determination of $V - R_C$ colour indeces at least at maximum light. These data can help checking our method and/or can help to increase the sample of well-parametrized systems down to fainter magnitudes.

3. We studied the possible role of W UMa-stars as distance indicators. We found that these objects can be used as galactic distance indicators and as distance indicators for some nearby galaxy within 1 Mpc.

Acknowledgments

This work was supported by the Hungarian Research Fund (OTKA), grant No. T034155. We thank Mr A. Moor (Dept. of Astronomy, Eötvös University) for his help in determining the interstellar reddening.

References

Claret, A., Gimenez, A., 1992, A&AS 96, 255
Maceroni, C., van't Veer, F., 1996, A&A 311, 523

Mochnacki, S. W., 1981, ApJ 245, 650
Rucinski, S. M., 1996, ASP Conf. Ser. 90, 270
Rucinski, S. M., Duerbeck, H. W., 1997, PASP 109, 1340
Rucinski, S. M., Lu, W., 1999, AJ 118, 2451
Lu, W., Rucinski, S. M., 1999, AJ 118, 515
Rucinski, S. M., 1997, AJ 113, 407
Shu, F. H., Anderson, L., Lubow, S. H., 1979, ApJ 229, 223
Lucy, L. B., 1976, ApJ 205, 208
Flannery, B. P. 1976, ApJ 205, 217
Robertson, J. A., Eggleton, P. P., 1977, MNRAS 179, 359
Hazlehurst, J., 2001, The Observatory 121, 86
Kähler, H., 1997, A&A 320, 787
Hill, G., Fisher, W. A., Holmgren, D., 1989, A&A 211, 81
Liu, X. F., Tan, H. S., 1988, AcASn 29, 16

Time-frequency Analysis of Variable Star Light Curves - The Program Package TiFrAn

Zoltán Csubry
Konkoly Observatory
H-1518 Budapest, P.O.Box 32., Hungary
E-mail: csubry@konkoly.hu

Abstract

We present the properties of the new software, TiFrAn developed for scientific applications of time-frequency analysis. We implemented the general (Cohen's type) kernel method for calculating time-frequency distributions in our program. We show the efficiency and usefullnes of this package by means of analysing semi-regular variable star light curves.
Keywords: *variable stars, time-frequency analysis*

1. Introduction

The development of the TiFrAn (Time-Frequency Analyser) program package was started in 2001. Our goal was to build a program for examination of time-dependent periodic and quasi-periodic processes. TiFrAn can perform several time-frequency methods. An additional aim was to extend the analysing power of the code with a data acquisition system for real-time signal processing.

The major part of the program (without the data acquisition system) is available freely for scientific and educational purposes, and it is running on UNIX based and MS Windows operating systems.[1]

TiFrAn already has been used in many scientific applications successfully. Several semi-regular variable star light curves were analysed with its help (Buchler&Kolláth, 2001).

2. Properties of TiFrAn

2.1. Main components

- Software engine (C): This engine performs the data processing, the calculation of several time-frequency distributions (for example STFT, Gábor, Wavelet, Wigner-Ville, Choi-Williams, Zhao-Atlas-Marks, see 2.2.), and

[1] See the web site *http://www.konkoly.hu/tifran*.

provides additional functionalities (Fourier-transformation, interpolation, filtering, whitening).

- Programmable Graphic User Interface (extended Tcl/Tk): With this simple language, the user can easily define a new graphical interface for special purposes. Menus, buttons, plot fields can be easily created. Several example GUIs are provided with the package.
- Extended Tcl script language: Our script language is suitable for definition of complex (and repeatable) tasks, and creating high-quality Postscript figures.
- Data acquisition system: The full version of the software includes sound card and data acquisition card support, and real-time data processing routines.

2.2. Time-frequency methods

We used the Cohen type kernel method for calculating time-frequency distributions. Different type of distributions can be defined with this formalism, which can be written in the following form:

$$C(t,\omega) = \frac{1}{4\Pi^2} \iiint s^*(u - \frac{\tau}{2}) s(u + \frac{\tau}{2}) \Phi(\theta,\tau) e^{-j\theta t - j\tau\omega + j\theta u} du d\tau d\theta \quad (1)$$

where s is the signal and $\Phi(\theta,\tau)$ is the kernel function (Cohen, 1995). In the case of $\Phi(\theta,\tau) = 1$, Eq (1) gives the Wigner-Ville distribution (Wigner, 1932), (Ville, 1948). The main problem with the Wigner-Ville distribution is the appearance of cross terms in multi-periodic signals. By using a suitable kernel the cross-terms are efficiently reducible but at the cost of some loss in resolution, so we have to make a compromise at choosing the correct kernel. Choice of the optimal kernel is a hard problem in many applications. The kernel functions of Wigner-Ville, Choi-Williams (Choi&Williams, 1989) and Zhao-Atlas-Marks (Zhao et al, 1990) distributions can be found in Table 1.

3. Light curve analysis

3.1. S Draconis - Comparison of time-frequency methods

In Fig 1 we show the light curve of the semi-regular variable star S Draconis and the time-frequency representations calculated by three different methods.

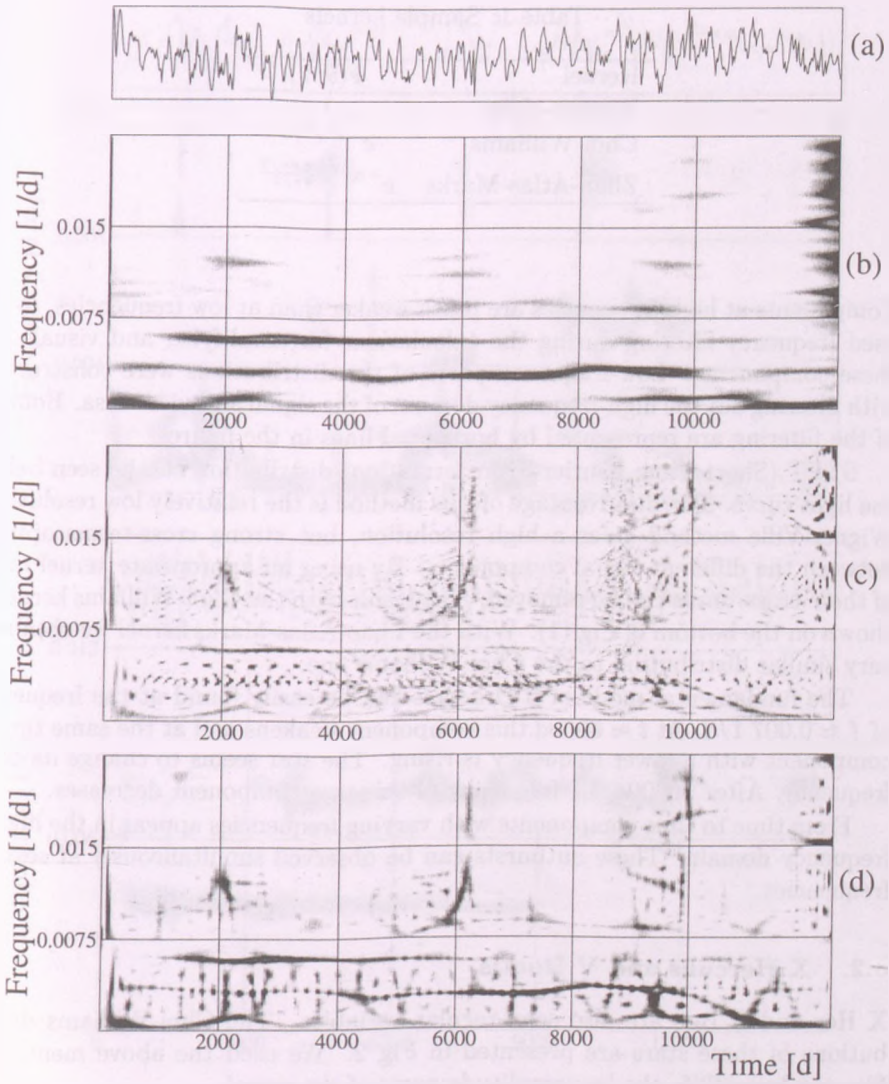

Figure 1: Light curve (a), STFT (b), Wigner-Ville (c) and Choi-Williams (d) distribution of semi-regular variable star S Draconis.

Table 1: Sample kernels

Kernel	$\Phi(\theta, \tau)$
Wigner-Ville	1
Choi-Williams	$e^{-\theta^2\tau^2/\sigma}$
Zhao-Atlas-Marks	$e^{-\alpha\tau^2}\frac{\sin\theta\tau/2}{\theta\tau/2}$

Components at high frequencies are much weaker than at low frequencies, so we used frequency filtering during the calculations for amplifying and visualizing these components. Low-frequency parts of the distributions were constructed with filtering out the high-frequency domain of the signal and vice versa. Bounds of the filtering are represented by horizontal lines in the figures.

STFT (Short Time Fourier Transformation) distribution can be seen below the light curve. The disadvantage of this method is the relatively low resolution. Wigner-Ville method gives a high resolution, but strong cross-terms appear between the different signal components. By using an appropriate kernel most of these cross-terms can be removed. The result with the Choi-Williams kernel is shown on the bottom of Fig (1). With the Zhao-Atlas-Marks kernel we obtained very similar distribution to the Choi-Williams one.

The fundamental mode of S Draconis can be easily found at the frequency of $f \approx 0.007\ 1/d$. At $t \approx 6000d$ this component weakens and at the same time a component with a lower frequency is rising. The star seems to change its base frequency. After $10000d$ the frequency of this new component decreases.

From time to time components with varying frequencies appear in the higher frequency domain. These outbursts can be observed simultaneously at several frequencies.

3.2. X Herculis and V Bootis

X Her and B Boo are also semi-regular variables. The Choi-Williams distributions of these stars are presented in Fig 2. We used the above mentioned filtering to amplify the low amplitude parts of the signal.

High amplitude modulation can be detected in the main period of X Her ($f \approx 0.01$). A low frequency component with a strongly varying frequency and amplitude also exists in the light curve. The amplitude variation of these two components are in opposite phase, alluding to the interaction between them.

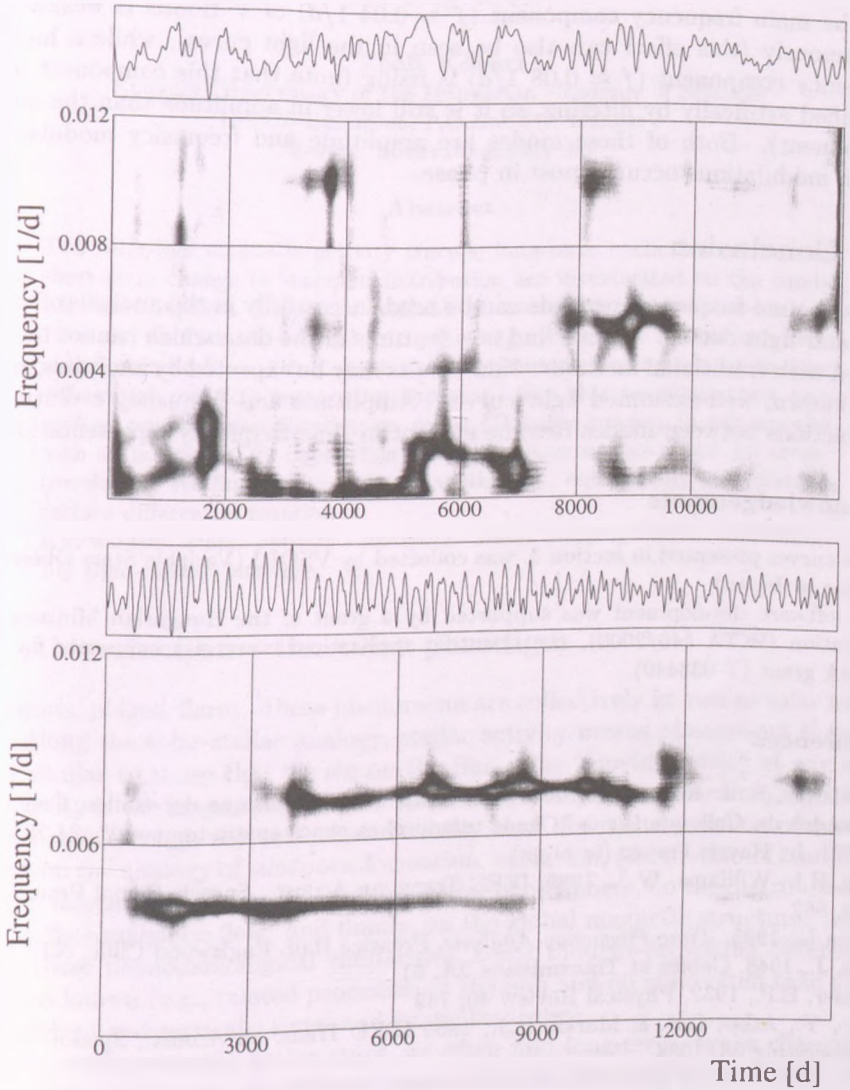

Figure 2: Light curve and Choi-Williams distribution of two semi-regular variable stars: X Herculis (top) and V Bootis (bottom).

The main frequency component ($f \approx 0.04\ 1/d$) of V Bootis is weakening continuously (this effect can also be seen in the light curve), while a higher frequency component ($f \approx 0.08\ 1/d$) is rising (note that this component was amplified artifically by filtering, so it is still lower in amplitude than the main component). Both of these modes are amplitude and frequency modulated, which modulations occur almost in phase.

4. Conclusion

Modern time-frequency methods can be used successfully in the analysis of variable star light curves. We can find new features in the data which cannot be detected with traditional methods. New results may be expected by analysing even well-known, well-examined light curves. Amplitude and frequency evolutions, interactions between modes become evident in time-frequency representations.

Acknowledgements

Light curves presented in section 3. was collected by VSOLJ (Variable Stars Observer League in Japan).
The software development was supported by a grant of the Hungarian Ministry of Education (IKTA 140/2000), the scientific applications were also supported by an OTKA grant (T-038440).

References

Buchler, J. R. & Kolláth, Z., 2001, Du chaos dans la musique des étoiles, Comptes Rendus du Colloque sur le "Chaos temporel et chaos spatio-temporel", 24-25 sep. 2001, Le Havre, France (in press)
Choi, H.I., Williams, W.J., 1989, IEEE Trans. on Acoust., Speech, Signal Processing 37, 862
Cohen L., 1995, *Time-Frequency Analysis*, Prentice Hall, Englewood Cliffs, NJ
Ville, J., 1948, Cables at Transmission 2A, 61
Wigner, E.P., 1932, Physical Review 40, 749
Zhao, Y., Atlas, L.E. & Marks, R.J., 1990 IEEE Trans. on Acoust., Speech, Signal Processing 38, 1084

Photometric Cycles and Starspot Tracking on LQ Hya

Zsolt Kővári
Konkoly Observatory of the Hungarian Academy of Sciences
H-1525 Budapest, P.O.Box 67., Hungary
E-mail: kovari@konkoly.hu

Abstract

Two solar-like magnetic activity tracers, long-term cyclic behaviour and short-term change in starspot distribution are investigated on the single K2 dwarf LQ Hya. Using the available photoelectric observations back to 17 years, we find 2.7, 4.2 and ≈13 year-long cycles, that remind us of the multi-periodic Sun. On a much shorter timescale, we search for surface differential rotation pattern on the star. For this we reconstruct two surface temperature distribution maps (Doppler-images) in two epochs with an interval of 20 days, then the consecutive surface maps are cross-correlated. We find evidence for solar-like (i.e., equatorially accelerated) surface differential rotation.
Keywords: *stars: activity - starspots - stars: imaging - stars: individual: LQ Hya - stars: late-type*

1. Introduction - the solar paradigm

Sunspots, plages, flares - these phenomena are collectively known as solar activity. Along the solar-stellar analogy, stellar activity means phenomena that are very similar to those that we see on the Sun. The "moving spirit" of any kind of activity is the magnetic field. Sunspots occur, where the inner magnetic field lines break through the surface and locally slow down the emission of energy. Thus, on the analogy of sunspots, formation, evolution, and motion of starspots, give us information on the state of the stellar photosphere, on the distribution of the surface magnetic field, and finally, on the global magnetic structure. Apart from these phenomenological similarities, some thought-provoking differences are also known (e.g., related processes on the Sun and on stars often take place on different geometrical-, time- and energetic scales).

On rapidly rotating active stars, we often find long-term, cyclic changes in the overall brightness, on different timescales (cf. Baulinas et al., 1996; Oláh et al., 2000, and references therein). Solar observations also show evidence for long-term quasi-periodic cycles. Beside the 11 year-long spot cycle, the one

with ≈90 years length is also widely known as Gleissberg-cycle (Gleissberg, 1966). Recently, Pipin (1999) introduced a promising numerical model based on a spherical shell dynamo to give explanation of this secular solar cycle. In Sect. 2 the long-term photometric variability of the fast-rotating solar-type star, LQ Hya is analysed and different cycles are shown.

Differential rotation, when the angular rotation has an equator-to-pole gradient, is necessary to maintain the magnetic dynamo, which is responsible for raising the magnetic flux from the base of the convective zone. While differential rotation can easily be observed on the solar surface, stellar differential rotation cannot be detected directly, because today's most advanced telescope with an angular resolution of mas cannot even resolve the nearest stellar surface. On the other hand, the indirect mapping technique Doppler-imaging (Vogt & Penrod, 1983) can reach an equivalent resolution of mmas, sometimes even higher. In Sect. 3 we apply this technique to map the surface of LQ Hya for two epochs. The time gap of 20 days between the two maps makes it possible to search for differential rotation pattern. The results are compared to the solar case.

2. Photometric cycles on different timescales

2.1. The data

The V data of LQ Hya collected in Oláh et al. (2000) is supplemented with another two years of photoelectric observations, made by the T7-Automatic Photoelectric Telescope of University of Vienna at Fairborn Observatory in Arizona. The completed light curve is plotted in the top left panel of Fig. 1, where a sinusoidal light variation on a time-scale of $\tau_1 \approx 13$ys is clearly seen (dashed line fit). However, a long-term cycle length comparable to the 17 year-long time base may not be real.

2.2. The method and the result

For the period analysis the MUFRAN (Kolláth, 1990) package is used. The program calculates discrete Fourier transforms for the unevenly sampled data then the recovered frequencies can be refined. The Fourier spectrum is displayed in the top right panel of Fig. 1. The first step was to prewhiten the long-term trend seen in the data, with a 0.00015677c/d frequency and two of its harmonics. Re-analysing the residual spectrum, two photometric cycles are found: $\tau_2 \approx 4.2$ys and $\tau_3 \approx 2.7$ys (see the middle and bottom panels of Fig. 1. This latter confirms the result in Oláh et al. (2000), where the authors also

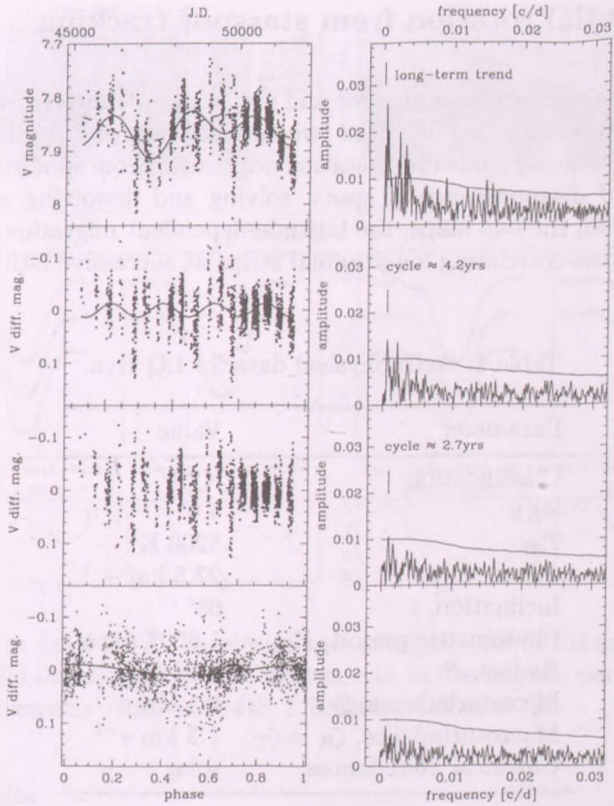

Figure 1: Frequency analysis: top panels show the original data and the frequency spectrum. Dashed fit is the longest (13ys) possible cycle, continuous fit follows the trend (see also the text). Below plotted are the prewhitened data and the corresponding spectra. At the bottom, the light curve is folded with the shortest ($\tau_3 \approx 2.7$ys) cycle length.

argued for a shortest cycle-length of 2.8ys, noting that the scatter of the folded data did not make it conclusive. In the bottom left panel of Fig. 1 the light curve, prewhitened by the long-term trend and then by τ_2, is folded with $\tau_3 \approx 2.7$ys, proving the existence of this shortest cycle with an amplitude of 0.02 mag.

3. Differential rotation from starspot tracking

Short-term starspot tracking is the one and only tool today to search for surface differential rotation on stars. We need two surface maps of a spotted star close enough in time to avoid a misinterpretation originating from spot evolution (i.e., appearance and disappearance of spots, solving and dissolving neighbouring spots, etc.). From the two maps, the latitude-dependent migration pattern can be drawn by cross-correlating longitudinal strips at successive latitudes.

Table 1: Astrophysical data for LQ Hya.

Parameter	Value
Classification	K2 V
$\log g$	4.0
$T_{\rm eff}$	5200 K
$v \sin i$	27.5 km s^{-1}
Inclination, i	65°
Photometric period, $P_{\rm rot}$	1.6007 days
Radius, R	0.98 $R_\odot$
Microturbulence, $\xi_{\rm Fe}$	0.5 km s^{-1}
Macroturbulence, $\zeta_{\rm R} = \zeta_{\rm T}$	1.5 km s^{-1}
Chemical abundances	solar

3.1. The data

We use ten new spectra, obtained with the Coudé feed telescope at Kitt Peak National Observatory during April 2000. A 3000×1000 CCD (15μ pixels) with an instrumental resolution of 32,000 was employed. The Fe I 6411Å mapping line, used for the Doppler-imaging, has an average signal-to-noise (S/N) ratio of ≈300:1. From our data we formed two subsets, for which the mean HJDs are 2,451,642.179 (08/04/2000) and 2,451,662.675 (28/04/2000). Basic astrophysical data for LQ Hya are listed in Tab. 1 (Kővári et al., 2002).

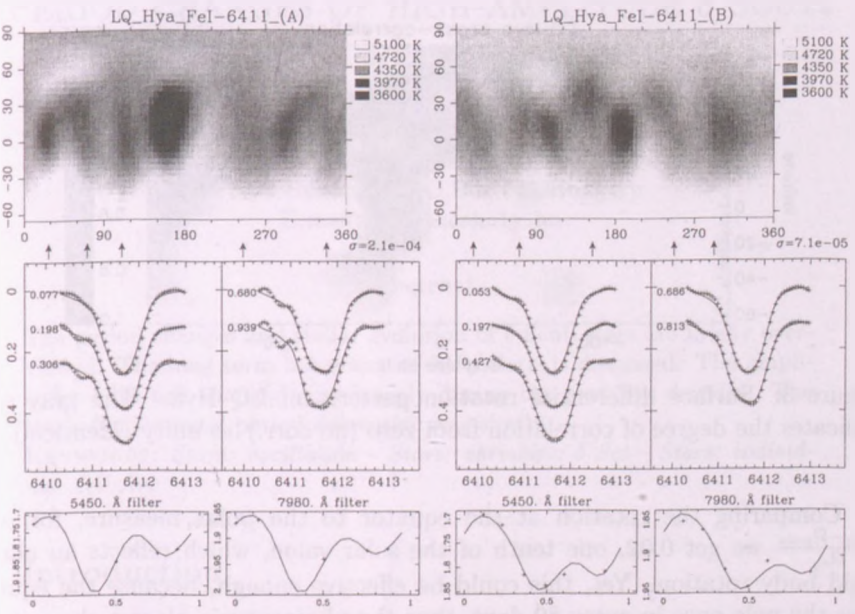

Figure 2: Top: FeI 6411 Å Doppler-images of LQ Hya for 08/04 and 28/04/2000. Spectra in the middle panels and light curves in the bottom panels are phased using the ephemeris $HJD = 2,448,270.0000 + 1.6007 \times E$.

3.2. Results

Our Doppler-imaging code `TempMap` is based on the Ap-star code by Rice (1991). The method includes a full spectrum synthesis via solving the equation of transfer through a set of (Kurucz, 1993) model atmospheres. All computations were performed on a Sun Ultra-2 workstation at Konkoly Observatory and required on average 15 CPU-minutes for one run with 8 blends and 15 iterations.

The resulting Doppler-maps are showed in Fig.2. Dominant spots and less-dominant features are recovered on both maps, however, mainly low-latitude spottedness is found, without polar spots, in agreement with previous maps obtained for the 1995 data of Rice & Strassmeier (1998). The result of cross-correlating the two maps is shown in Fig. 3. The equatorial zone rotates faster with respect to the average rotation, while polar region lags behind. Fitting the best correlated regions by a $\sin^2\beta + C$ function, we estimate the differential rotation law as $\Omega(\beta) = 3.929 - 0.075 \sin^2\beta$ [rad/day].

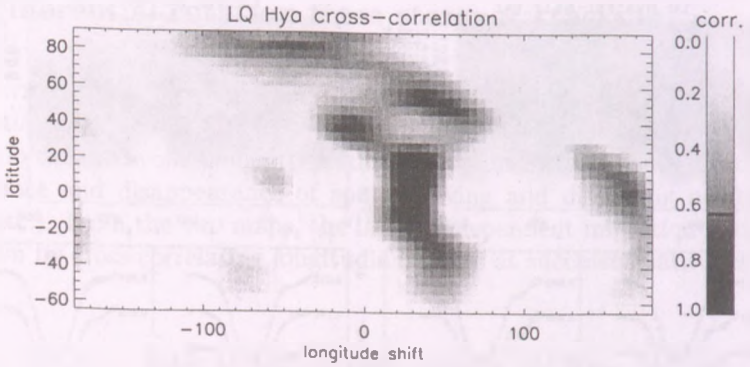

Figure 3: Surface differential rotation pattern on LQ Hya. The gray scale indicates the degree of correlation from zero (no corr.) to unity (identical).

Comparing the rotation at the equator to the polar measure, for $\alpha = \frac{\Omega_{eq} - \Omega_{pole}}{\Omega_{eq}}$ we get 0.02, one tenth of the solar value, which reflects an almost rigid body rotation. Yet, this could be effective enough, because the equator laps the pole once in every 80 days, thus the photospheric plasma shear is one and a half times greater than on the Sun.

Acknowledgements

It is a great pleasure to thank J. Jurcsik, K. Oláh, K.G.Strassmeier and Z. Kolláth for useful discussions. The author is supported by OTKA T-032846 and the German-Hungarian S&T cooperative program D-21/2001.

References

Baliunas S. L., Nesme-Ribes E., Sokoloff D., Soon W. H. 1996, ApJ 460, 848
Gleissberg W., 1966, J. British Astron. Assoc. 76, 265
Kolláth Z. 1990, MUFRAN, Occasional Technical Notes of Konkoly Observatory, No.1
Kővári Zs., Strassmeier K.G., Weber M., et al. 2002, in preparation
Kurucz R. L. 1993, VizieR Online Data Catalog, 6039, 0
Oláh K., Kolláth Z., Strassmeier K.G. 2000, A&A 356, 643
Vogt S. S., Penrod G. D. 1983, PASP 95, 565
Pipin V.V. 1999, A&A 346, 295
Rice J.B. 1991, A&A 245, 561
Rice, J.B., Strassmeier, K.G. 1998, A&A 336, 972

Period changes of high-amplitude δ Scuti stars

Miklós Pócs
Konkoly Observatory
H-1525 Budapest, P.O.Box 67., Hungary
E-mail: pocs@konkoly.hu

Abstract

The period changes and stellar evolution of δ Scuti stars are briefly overviewed. The long term behaviour of RV Arietis is discussed. The amplitudes have not changed significantly during the past five decades. The star's fundamental period decreased very slowly.
Keywords: *Stars: oscillation – Stars: variables: δ Sct – Stars: individual: RV Ari*

1. Introduction

δ Scuti stars (Breger, 1972) are short period pulsating variables within the classical instability strip on or near the main sequence (MS). Their masses range between 1.5 $M_\odot$ and about 2.5 $M_\odot$. They pulsate in various radial and non-radial p- and g-modes with multiple periods from 0.02 to 0.2 days. The amplitudes of most δ Scuti stars are relatively low around 0.001 mag. but a numerically small subgroup can be characterized by exceptionally high amplitudes over 0.3 mag. some reaching even 1 mag. In the past these high amplitude δ Scuti stars (HADS) were referred to as "dwarf Cepheids" or AI Vel stars.

2. Period changes and stellar evolution

The physical parameter of a high amplitude δ Scuti star which can be determined with the highest accuracy is the pulsational period. The period is related to the structure of the star through the pulsation equation $P\sqrt{\varrho} = Q$, the period change is therefore related to the evolutionary radius change, if we assume that the mass of the star does not vary. As a consequence, the period changes caused by stellar evolution in and across the instability strip make it possible to reveal evolutionary changes in the stellar structure long before they can be detected in any other measurable quantity (Szeidl , 2000).

Evolutionary models developed by Breger and Pamyathnykh (1998) predict that in pre-MS stage the period decreases rapidly ($P_1{}^{-1}\mathrm{d}P_1/\mathrm{d}t = 10^{-6}$–$10^{-8}$ year^{-1}), while in the MS and post-MS stages (where the majority of δ Scuti stars can be found) the period is constant or slowly increasing. (In some cases even very slow decrease in the period is possible).

A comparison with the observed period changes, however, showed large discrepancies: the observed increase in periods of some stars was a factor of about ten times larger than the value predicted by the theory. Considering the side of observations the question arises, whether the real period changes of these stars are known sufficiently well for comparison with the theoretical expectations. It may happen for example that due to large gaps in the observational data the number of cycles elapsed between two observed maxima is not properly known and is incorrectly taken into account. This problem occurred in the case of AE UMa which had earlier been treated as a pre-MS star with fast period decrease. A detailed analysis of the available observations led to the conclusion that the fundamental period is essentially constant and the star is in the post-main sequence evolutionary state (Pócs and Szeidl, 2001). Another possible reason for misinterpretation of the period changes is the light-time effect, that is, the star is a member of a binary system and the orbitational period is longer than the time base of the observational data. In these cases only a short part of the sinusoidal $O - C$ diagram is investigated and a linear period change is derived. This offers a possible solution for the question of DY Her. Using the data of over 40 years of observations of DY Her suggests that the previous erroneous interpretations of its period changes can be explained by assuming that the star belongs to a binary system (Pócs and Szeidl, 2000).

3. RV Arietis

3.1. Discovery and observations

The variability of RV Ari was discovered by Hoffmeister (1934) on Sonneberg plates. Soon after its discovery the star was intensively observed visually by Lange (1935) who derived 8 times of maxima. Later Detre (1937) made an attempt at determining the period of the star from his photographic observations, however, he arrived at an erroneous result. At Merate Observatory Broglia and Pestarino (1955) commenced the photoelectric observations of RV Ari in blue and yellow lights. They derived the correct value of the dominant period: $P_0 = 0.09312819$ days and came to the conclusion that the light curve of the star was strongly modulated by a second period. Detre (1956) used Broglia

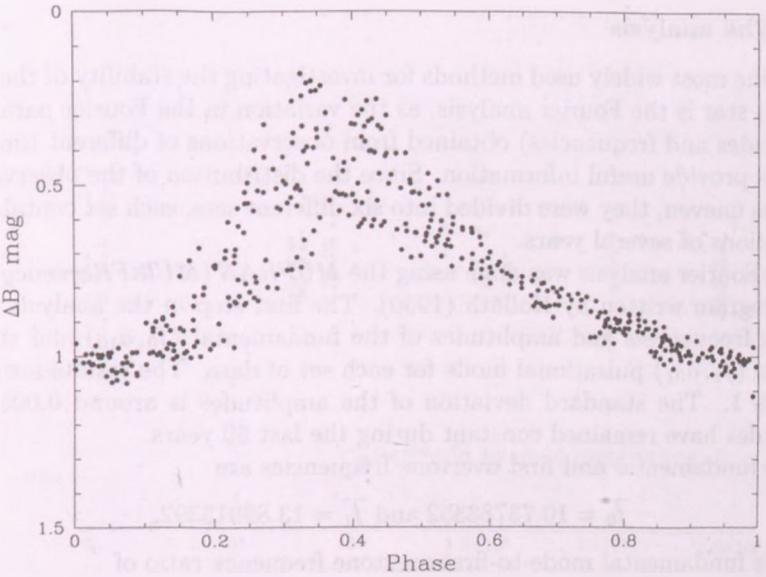

Figure 1: Light curve of RV Ari folded with the period 0.093128224 days based on the 1996-97 observations made by the Konkoly Observatory's 1m RCC telescope. The light curve is modulated with the 0.316330525 day period, which manifests itself as scatter.

and Pestarino's observations and was able to determine the modulation period: $P_{\rm m} = 0.316256$ days. Subsequent photographic (Balázs, 1956) and photoelectric observations affirmed these results. Rodríguez et al. (1992) observed RV Ari in the Strömgren photometric system and derived the star's physical parameters. RV Ari is a normal Pop. I star with near solar abundance and very close to the end of the main sequence evolutionary stage with the age of $1.1(\pm 0.2) \times 10^9$ years.

The photometry at the Konkoly Observatory between 1958 and 1997 was carried out in B, V, R_c, and I_c colours. Fig.1 demonstrates the light curve obtained from the Konkoly observations. For the investigation of the stability of the frequencies 104 published and 50 unpublished epochs were available.

3.2. The analysis

One of the most widely used methods for investigating the stability of the pulsation of a star is the Fourier analysis, as the variation in the Fourier parameters (amplitudes and frequencies) obtained from observations of different time periods may provide useful information. Since the distribution of the observational data was uneven, they were divided into six different sets, each set containig the observations of several years.

The Fourier analysis was done using the *MUFRAN* (*MUltiFRequency ANalysis*) program written by Kolláth (1990). The first step in the analysis was to find the frequencies and amplitudes of the fundamental (f_0, a_{10}) and the first overtone (f_1, a_{01}) pulsational mode for each set of data. The results are shown in Table 1. The standard deviation of the amplitudes is around 0.005. The amplitudes have remained constant during the last 50 years.

The fundamental and first overtone frequencies are

$$\overline{f_0} = 10.73788352 \text{ and } \overline{f_1} = 13.89913392,$$

with the fundamental mode-to-first overtone frequency ratio of

$$\frac{f_0}{f_1} = 0.77256.$$

The importance of the frequency ratio lies within those stellar pulsation models where it helps to determine other stellar parameters like mass, metal content etc. (Petersen and Christensen-Dalsgaard, 1996).

Table 1: Amplitudes obtained from the first and last series of photoelectric observations.

	$a_{10}(V)$	$a_{01}(V)$	$a_{10}(B)$	$a_{01}(B)$
1954–58	0.210	0.060	0.271	0.074
1996–97	0.211	0.065	0.265	0.079

3.3. The $O-C$ diagram

The Fourier analysis is definetely useful for determining the pulsational frequencies especially when all the photometric observations are included in the

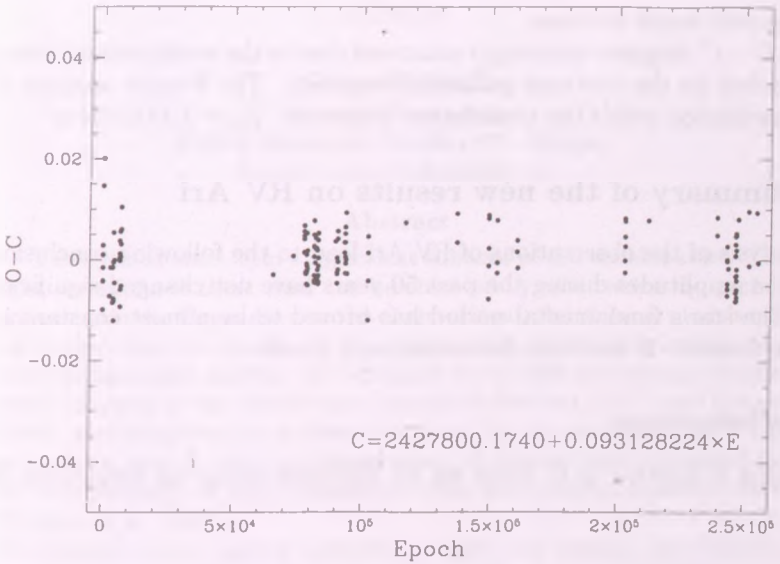

Figure 2: $O-C$ vs. epoch number diagram for the fundamental mode of RV Ari. The covered time interval is 61 years.

analysis. However, it is not capable of detecting small changes in the frequencies, because the standard errors are much greater than the changes taking place in a period of a few decades. Nevertheless, when a large enough number of maxima is available the construction of the $O-C$ diagram may surmount this problem.

The $O-C$ values obtained from all the available observations (154 times of maxima over 61 years, including the visual and photographic data as well) were fitted with a quadratic polynomial using the least-squares method, which resulted in the following formula:

$$O-C = 2427800.1730 + 0.093128251 \times E - 0.91 \times 10^{-13} \times E^2$$
$$\pm.0010 \quad \pm .000000018 \qquad \pm .66$$

Hence the relative period change

$$\frac{1}{P}\frac{\mathrm{d}P}{\mathrm{d}E} = -0.196 \times 10^{-11}\frac{1}{\text{cycle}} = -0.77 \pm .56 \times 10^{-8}\mathrm{y}^{-1}$$

indicates very small decrease.

The $O - C$ diagram is strongly scattered due to the modulation in the light curve caused by the overtone pulsation frequency. The Fourier analysis of the $O - C$ oscillation yields the modulation frequency: $f_{\mathrm{m}} = 3.1612504\ \mathrm{d}^{-1}$.

4. Summary of the new results on RV Ari

The analysis of the observations of RV Ari lead to the following conclusions:

i) The amplitudes during the past 50 years have not changed significantly.

ii) The star's fundamental period has proved to be almost constant in the past six decades. It has been decreasing very slowly.

Acknowledgements

The author is indebted to B. Szeidl for his kind help during the preparation of this paper.

References

Balázs, J. 1956, Budapest, Mitt. No. 40, 8
Breger, M. 1972, ApJ, 171, 539
Breger, M., Pamyathnikh, A. A., 1998, A&A 332, 958
Broglia, P., Pestarino, E. 1995, Mem. Soc. Astr. It. 26, 429
Detre, L. 1937, Astron. Nachr. 262, 81
Detre, L. 1956, Budapest, Mitt. No. 40, 3
Hoffmeister, C. 1934, Astron. Nachr. 253, 195
Kolláth, Z. 1990, Occasional Technical Notes, Konkoly Obs. No. 1
Lange, G. A. 1935, Tadjik Circ. No. 4
Petersen, J. O., Christensen-Dalsgaard, J. 1996, A&A 312, 463
Pócs, M. D., Szeidl, B. 2000, IBVS No. 4832
Pócs, M. D., Szeidl, B. 2001, A&A 368, 880
Rodríguez, E., Rolland, A., López de Coca, P., García-Lobo, E., and Sedano, J. L. 1992, A&AS, 93, 189
Szeidl, B. 2000, ASP Conference Series, Vol. 210

Analysis of multicolor light curves of active stars

Gábor Ribárik
Konkoly Observatory
H-1525 Budapest, P.O.Box 67., Hungary
E-mail: ribarik@konkoly.hu

Abstract

The spotted stars form a significant subclass of the variable stars. The light variations of these stars can be observed by *photometric* or *spectroscopic* methods. Depending on the observational, the physical models can be divided into two groups: (i) the photometric spot models and (ii) the spectroscopic spot models. In this paper the author presents the fundamental aspects of the *analytic* spot models of Budding (1977) and Dorren (1987) and the principles of their application for the determination of the geometrical and physical spot parameters. A new method is proposed for the determination of spot temperature from multicolor photometric data (Ribárik et al., 2002).

Keywords: *stars: spotted variables, analytic spot models, spot temperature, nonlinear least-squares fitting*

1. Analytic spot models

In the analytic spot model of Budding (1977) or Dorren (1987) it is assumed that the loss of light is caused by a circular spot with center (λ, β) and with angular radius γ. The radius of the star is the unit length.

1. The loss of light due to the presence of the spot depend only on the γ size of the spot and on the ε angle between the surface normal at the spot center and the line of the sight (see: Fig. 1).

2. The equation determining the angle ε at time t (see: Fig. 2):

$$z_0 = \cos\varepsilon = \cos(\lambda - \Phi)\cos\beta\sin i + \sin\beta\cos i, \tag{1}$$

where i is the inclination of the rotation axis of the line of sight, and Φ is the phase of rotation defined by:

$$\Phi = 2\pi \frac{t - E}{P}. \tag{2}$$

3. Budding defined the following integrals (see: Fig. 1):

$$\sigma_n^m = \frac{1}{\pi} \iint\limits_{\text{spot's area}} x^m z^n \, \mathrm{d}x\mathrm{d}y. \tag{3}$$

In the following we call it σ-integrals.

- The integral σ_0^0 is the projected spot's area. Therefore it is is the most important quantity in the description of the light loss.
- The integral σ_1^0 describes the effect of the linear limb darkening.

4. Depending on the position of the spot, there are three possible cases (see: Fig. 1):

- the entire outline of the spot is visible: $\varepsilon \leq \frac{\pi}{2} - \gamma$.
- the spot is partially in view: $\frac{\pi}{2} - \gamma < \varepsilon < \frac{\pi}{2} + \gamma$.
- the spot is out of view: $\varepsilon \geq \frac{\pi}{2} + \gamma$. In this case: $\sigma_0^0 = \sigma_1^0 = 0$.

5. The explicit analytic forms of the σ_0^0 and σ_1^0 integrals are given by Budding (1977) and by Dorren (1987), in a slightly different way.

6. By introducing the linear limb darkening coefficient u, Budding defined the following spot-darkening function (Budding, 1977):

$$\sigma_c(u, \gamma, z_0(t)) = \frac{3}{3-u} \left\{ (1-u)\, \sigma_0^0 + u\, \sigma_1^0 \right\}. \tag{4}$$

7. Using these notations, the intensity of the spotted star is:

$$I_c(t) = U \left\{ 1 - (1 - \kappa_w) \sigma_c(u, \gamma, z_0(t)) \right\}, \tag{5}$$

where U is the unspotted intensity of the star, and the coefficient κ_w is the flux ratio of the spot and the photosphere depending on the wavelength and on the relative temperature of the spot.

8. In the case of binary system, the loss of light depend on the L_1 intensity of the spotted star and on the U intensity of the system:

$$I_c(t) = U - L_1 (1 - \kappa_w) \sigma_c(u, \gamma, z_0(t)). \tag{6}$$

9. If USI denotes the unspotted intensity of the star in magnitude scale, then the intensity of the spotted star in magnitude scale is:

$$l_c(t) = \mathrm{USI} - 2.5 \log_{10} \left\{ \frac{U - L_1(1 - \kappa_w)\sigma_c(t)}{U} \right\}. \tag{7}$$

These formulae can be extended in a straightforward manner if the number of spots is greater than one.

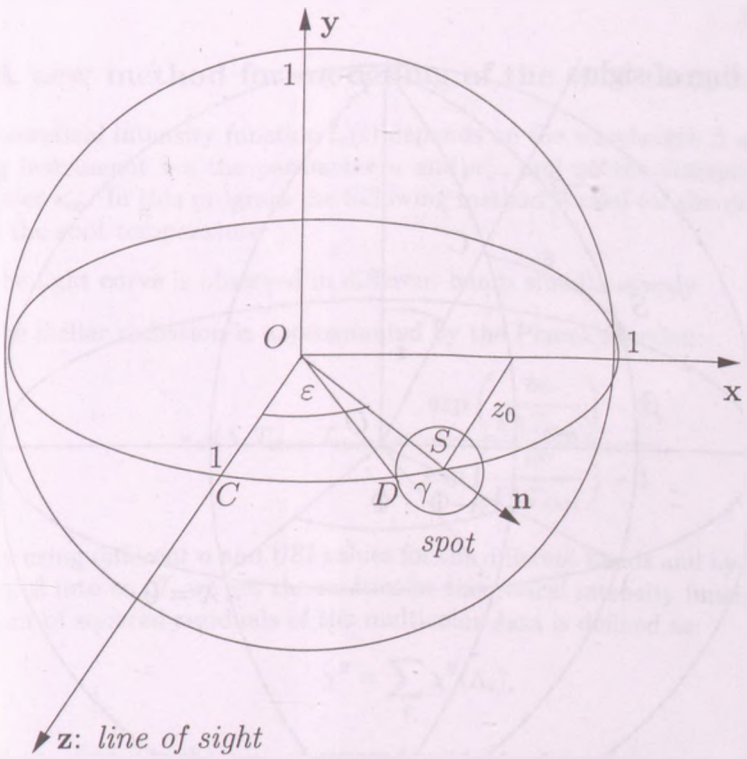

Figure 1: The calculation of the loss of light due to the presence of the spot. $\gamma = SOD\measuredangle$ is the radius of the spot, $\varepsilon = SOC\measuredangle$ is the angle between the surface vector **n** at spot center S and the direction **z** of the line of sight.

2. The standard spot model

This is the original model proposed by Budding (1977). This case the observed $l_o(t)$ intensities are fitted by the theoretical intensity function $l_c(t)$ in the whole time interval. For this purpose a nonlinear least squares algorythm, like the Marquardt-Levenberg algorythm (Levenberg, 1944; Marquardt , 1963), is needed. By minimizing the sum of squared residuals: $\chi^2 = \sum_{i=1}^{m} \frac{(l_{o_i} - l_{c_i})^2}{\Delta l_i^2}$, we get the optimal parameter values. In this model, the spot parameters are constant.

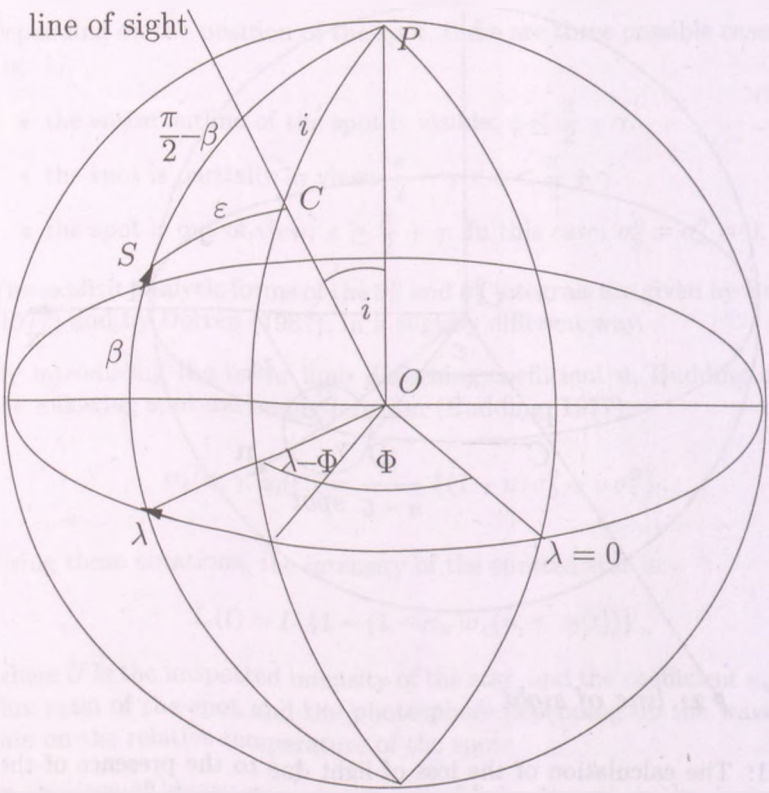

Figure 2: The calculation of the angle ε between the surface vector at spot center S and the direction of the line of sight.

3. The spot model using time series

In some cases the shape and amplitude of the light curve change in function of time. This is due to the movement, growth or diminution of the spots. In this model the time interval is divided into smaller subintervals and for each interval the standard model is applied. In this way we get a set of spot parameters in function of time. The theoretical intensity curve is obtained by averaging the theoretical intensity values of the standard models on the overlapping intervals. The model was developed by Bartus (1996).

4. A new method for modelling of the spot temperature

The theoretical intensity function $l_c(t)$ depends on the wavelength Λ of the observing instrument via the parameter u and κ_w, and on the starspot via the parameter κ_w. In this program the following method is used for the determination of the spot temperature:

1. the light curve is observed in different bands simultaneously.
2. the stellar radiation is approximated by the Planck function:

$$\kappa_w(\Lambda, T_{\text{star}}, T_{\text{spot}}) = \frac{\exp\left(\frac{hc}{k\Lambda T_{\text{star}}}\right) - 1}{\exp\left(\frac{hc}{k\Lambda T_{\text{spot}}}\right) - 1}. \tag{8}$$

3. by using different u and USI values for the different bands and by inserting eq. 8 into eq. 7, we get the multicolor theoretical intensity function. The sum of squared residuals of the multicolor data is defined as:

$$\chi^2 = \sum_i \chi^2(\Lambda_i), \tag{9}$$

where $\chi^2(\Lambda_i)$ is the sum of squared residuals of the data in the band Λ_i. The spot parameters and the spot temperature T_{spot} are refined using the multicolor observed data and the multicolor theoretical intensity functions.

In a paper on XX Tri (Strassmeier & Oláh, 1992) a similar method was used but the spot temperature was determined by the $\left(\sum_i \chi^2(\Lambda_i)\right)(T_{\text{spot}})$ plot. The

novelty of this method is the direct refinement of the parameter $T_{\rm spot}$ via the nonlinear eq. 8. The program can be easily modified by changing the function $\kappa_w(\Lambda, T_{\rm star}, T_{\rm spot})$.

Acknowledgements

The author acknowledges support from OTKA T032846, and from the Hungarian-German Int. S&T Grant D21/2001.

References

Budding, E. (1977). *Astroph. and Space Sci.* **48**, 207-223.
Dorren, J. D. (1987). *Astroph. J.* **320**, 756-767.
Bartus, J. (1996). *Occasional Technical Notes at Konkoly Observatory* No. 1/96
Ribárik, G., Oláh, K. and Strassmeier, K. G. (2002). *in preparation*
Strassmeier, K. G. and Oláh, K. (1992). *Astronomy and Astrophysics* **259**, 595.
Levenberg, K. (1944). *Quart. Appl. Math.* **2**, 164-168.
Marquardt, D. W. (1963). *SIAM J. Appl. Math.* **11**, 431-441.

Published by the Department of Astronomy of the Eötvös University
Budapest 2002

- Application of (Magneto)hydrodynamics
- Celestial Mechanics
- Extragalactic Astronomy
- Interstellar Matter
- Variable Stars

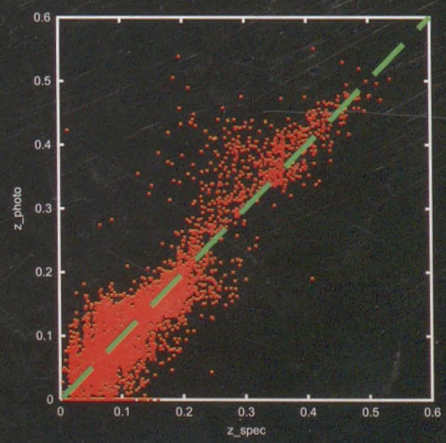

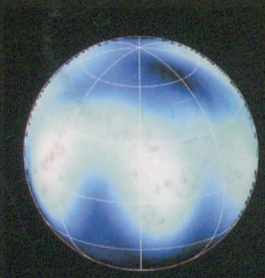

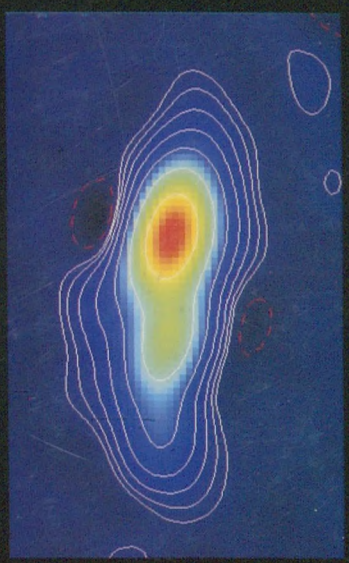

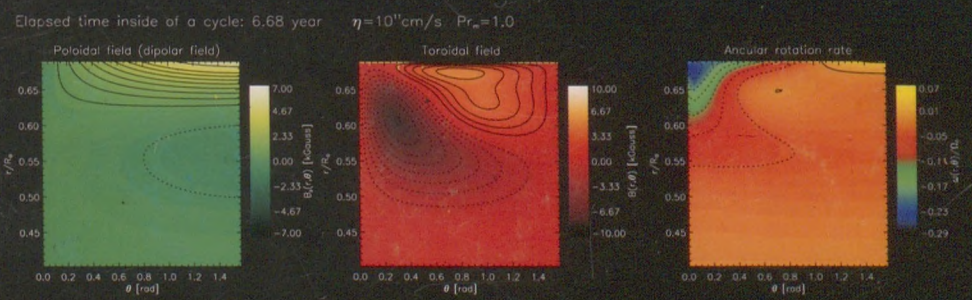

PADEU Vol.12